Development of a new
single-step process for the production
of SnO_2 based gas sensors

Entwicklung eines neuartigen
einstufigen Herstellungsprozesses
für Gassensoren auf SnO_2 Basis

DISSERTATION

der Fakultät für Chemie und Pharmazie
der Eberhard-Karls-Universität Tübingen

zur Erlangung des Grades eines Doktors
der Naturwissenschaften

2007

vorgelegt von

Thorsten Sahm

The first 90% of the work need 90% of the time.
The rest takes the other 90%.

Yogi Berra

Table of contents

1

Introduction

1.1 Motivation

Gas sensing in its very rudimentary meaning is simply about finding a qualitative or quantitative measure of a certain gaseous atmosphere. This is done subconsciously by every human being in their every day life. For example, the human nose advises against eating spoilt food. However, in the course of industrialisation and technological progress the need to control toxic or odourless gases increased tremendously as they are key measurands in many industrial and domestic environments. This need forced engineers and scientists at all times to develop solutions for the actual problems in the field of gas sensing. Accordingly, as early as in the 19th century a gas detecting device was invented by the chemist Humphry Davy [1]. In 1815, he presented a safety lamp for coal mines that indicated the presence of methane, which together with oxygen could form an explosive gas mixture leading to many disastrous mine accidents at that time. This is an early example that scientists and engineers are confronted with the needs of society while performing their research. As in course of time the applications became more and more sophisticated, also smart solutions for the corresponding gas sensing devices had to be found.

When in the late 1950ies and early 1960ies scientists discovered that the free charge carrier concentration of semiconducting metal oxides may be altered due to the interaction with reactive gases [2, 3, 4], a new direction of development for gas sensors was initiated. It was Taguchi who brought the first semiconducting gas sensors based on metal oxides to an industrial application [5]. Since then much effort has been made by both, academic scientists and industry to improve this new kind of user-friendly, robust and cheap gas sensing devices. Today, there are various companies in different countries that commercially produce and distribute metal oxide gas sensors, e.g. Figaro and FIS in Japan, Umweltsensortechnik UST and Applied Sensor in Germany, MICS in Switzerland or City Technologies in the UK [6, 7, 8, 9, 10, 11]. This development is a reflection of the socio-economic needs of the industrialised civilisation and always has to face the actual requirements of potential markets. This is one of the main reasons why research and development are still an ongoing dynamic process.

While the potential field of applications is an increasing one, at the same time a slight shift in the focus of research has appeared during the last 10 to 15 years. In the past a lot of effort has been made on typical e-nose applications where scientists tried to replace and even exceed the features of the human nose. In this context, setups for food monitoring were invented that tried to control for example the level of roasting of coffee beans, the origin or quality of different vine varieties, the quality of olive oil, or the freshness of fish. However, the number of publications on these topics has decreased during the last years. There are other fields that are still of great interest and where research is still going on simply because satisfying solutions are strongly desired by users, i.e. mainly automotive (air quality control, exhaust control) and domestic (smart ac control, fire alarm) applications and all solutions that deal with the control of industrial processes (e.g. leak control of industrial toxic chemicals).

Especially after the incidents of 09/11 the world has changed with regard to many aspects, which also did not keep the field of gas sensors unaffected. Nowadays there is a growing demand in the field of security. Security agencies seek for reliable systems for a rapid detection of harmful chemicals, e.g. a fast screening of passengers and luggage at the airport security check, static systems to monitor public places (train stations, crowded squares, big lobbies of public buildings) or mobile systems to monitor critical events (demonstrations, concerts, state visits) for detecting chemical warfare agents (cwa) and explosives. A relatively new sector and one with growing importance is the field of healthcare. Possible applications are homebased systems to support and monitor the medical conditions of elderly people or chronic illnesses ("assisted living"). This short overview of the industrial and the consumer aspect of gas sensing clearly reveals the increasing and changing demand for satisfying gas sensing solutions.

Consistently, a lot of academic research has been done in the past and is still going on to meet these requirements. Among the different kinds of gas sensors, the metal oxide based conductometric sensors are the most investigated ones. This is shown by an overview of the latest scientific conferences in the field of gas sensing (Table 1). Both conferences, the International Meeting on Chemical Sensors (IMCS) and the Eurosensors Conference deal not only with gas sensing, but with solid state sensors in general. However, a large part of

the contributions is dedicated to conductometric based metal oxide (MOX) gas sensors with electronic conduction. Among them, tin dioxide (SnO_2) plays the most important role. In most of the published research the authors report remarkable or even excellent sensing behaviour towards a specific single gas (analyte) under relatively unrealistic lab conditions, i.e. continuous and stable flow conditions for minutes or hours, constant level of humidity and absence of interferants. Meanwhile, there exists a large pool of knowledge about different sensing materials, a variety of production methods and deposition techniques among the scientists in the gas sensing community.

Table 1: Overview of the scientific contributions at the International Meeting on Chemical Sensors (IMCS) in 2004 and the Eurosensors XIX in 2005. (Data were collected from the proceedings of the conferences.)

Scientific contributions at	
IMCS 2004	**Eurosensors 2005**
total	
482	470
about conductometric MOX based gas sensors	
125	68
electronic conductance	
111	64
SnO_2	
73	40

However, there is still a large mismatch between industrial needs and academic research, displayed by the fact that only very few new developments in research overcome the barriers into industrial implementation. A main reason is the fact that in most cases the focus of scientists is on developing a new technology (e.g. sensing material, deposition method, data acquisition, etc.), and afterwards an application which fits to the achieved properties is searched. A good example is the latest focus on the development of metal oxide nanowires or nanorods [12]. After establishing ambitious techniques to produce such materials, many scientists evaluate their physical properties by a trial-and-error approach [13, 14, 15, 16]. However, promising future research has to be oriented vice versa in order to cope with the demands for commercial exploitation. The initial step is to

analyse which features a future sensing device needs for the desired application and to screen possible research concepts for it. Additionally, the strong restrictions of industry for mass production (i.e. cost efficiency, easy-to-use, harmless production and use) should be taken into account from the very beginning. Otherwise scientific research is just an academic exercise taking place in an ivory tower and is of no use for ordinary people and their daily life. Especially the field of gas sensing research is an academic discipline where the connection to the final device and to the demands of end users is most prominent.

Today, most of the commercially available sensors are fabricated by screen printing of pre-processed metal oxide powders. This technique leads to porous thick films with a large accessible surface for oxide-gas interaction. Screen printing is a standardised process which allows the use of unskilled workers for mass production when once the production parameters are adjusted; it leads to reproducible geometries of the sensing layers; and it is a cost-efficient production method. However, this technique has several drawbacks with regard to both manufacturing and sensor performance. Generally, the processing of the metal oxide powder consists of time and labour consuming steps; important parameters like grain size distribution and layer thickness are difficult to control and to vary. Screen printed layers tend to contain inhomogeneities in the sensing layer due to solvent evaporation, and they often show poor selectivity. Nevertheless, screen printing is still the frequently used technology when it comes to industrial appliance. Every new development in sensor production technology has to be benchmarked with the existing standard (i.e. screen printing) and to beat the latter where it has its limits.

1.2 Scope of the work

The research work in this thesis is based on and embedded in the knowledge of the gas sensor group at the ipc Tübingen that has been gained through the last years. Having a profound background in both, sensor fabrication technology [17, 18] and fundamental scientific research in the sensing mechanism of metal oxide semiconductors [19, 20], provided the basis for carrying out a systematic strategy to develop a new kind of sensor

fabrication method with enhanced sensing properties. This systematic development will be the main focus of the present work.

When it comes to the checkpoints of such a development, the desired new technique should in the best case allow the user to easily control important parameters such as grain size and size distribution to ensure optimum sensor performance and reproducibility. Additionally, the method should be technologically flexible, i.e. it should be applicable to many different metal oxides, and it should allow for different loadings of different noble metals. With regard to commercial exploitation, it should also be a fast and clean process to fulfil business and safety requirements. Against this background such a candidate could be the deposition of the metal oxide particles from the gas phase. It is reported that methods based on gas phase (aerosol) processes such as the flame spray pyrolysis (FSP) lead to nanoparticles with a very narrow size distribution [21, 22]. Additionally, FSP is a very fast (within minutes) and clean (i.e. without any organic additives) method already applied for the production of inorganic catalysts [23]. Therefore, a close collaboration between the author of this thesis and the research group of PD Dr. Lutz Mädler (formerly at the Particle Technology Laboratory at the Swiss Federal Institute of Technology (ETH) in Zürich, Switzerland, now at the Department of Chemical Engineering at the University of California (UCLA) in Los Angeles, USA), who has a profound background in the fabrication of nanoparticles via FSP synthesis, was built up. In the context of this thesis, the fabrication of all metal oxide nanoparticles via FSP and the experimental realisation of the commonly developed new deposition concept were carried out by the group of L. Mädler.

The starting point of the research within this thesis was to use the FSP method to fabricate sensing material (undoped SnO_2 in a first approach) and to use this metal oxide powder for standard sensor production, i.e. screen printing and drop coating. By doing so, the influence of the powder production method itself on the sensing properties was investigated. It revealed that thus fabricated sensors showed superior sensing behaviour for typical reducing gases like CO and ethanol. Doping of the sensing material with noble metal is a common method to improve sensor performance. For this reason, the

capability of FSP to add dopants to the SnO_2 has been tested, one batch with low loading of platinum (0.2 wt% Pt) and one with high loading (2.0 wt% Pt).

Nevertheless, the drawbacks of the screen printing method were still present. Thus, the next decisive step was to combine the formation of nanoparticles via FSP with the direct deposition of the latter from the aerosol phase by thermophoresis on sensor substrates. This can be regarded as a milestone in the research in gas sensor development as it merges the two processes of (i) production of sensing material and (ii) fabrication of the sensing element in one single-step. To establish and further develop these promising achievements, an intensive and systematic study on this method has been carried out. To check the possibility of controlling the grain size of the sensing metal oxide, sensors with different grain sizes of SnO_2 varying from 5.5 nm to 17 nm have been synthesised and compared. The thickness of the sensing layer depends on the deposition time of the sensing material on the substrate. Different deposition times between 30 s and 360 s were investigated. Changing the deposition time and thus the thickness of the sensing layer did not affect the other parameters like layer porosity or grain size. Thus, direct deposition of FSP made nanoparticles allows for specifically changing a certain parameter while the others still remain constant.

To fully make use of the potential of this new sensor fabrication method a way was developed to deposit several layers consisting of different metal oxides subsequently on top of each other. The gain of this approach is to use a catalytic active metal oxide as the top layer. This layer can either activate the analyte for the subsequent gas sensing reaction or decrease the concentration of the analyte by catalytic burning of the latter. Thus, such a top layer can be regarded as a filter layer of the sensing element. As the use of filters in gas sensing is widely known, the possibility to deposit multiple layers of different kinds of metal oxides on top of each other seems to be a promising feature and has been investigated. Finally, a complex gas sensor can be produced within one production step including the production of the sensing metal oxide containing noble metals as dopants, a second metal oxide as filter material (also with noble metals) and the deposition of these materials on sensor substrates. Figure 1 schematically displays the achieved new technology in contrast to the state-of-the-art technology.
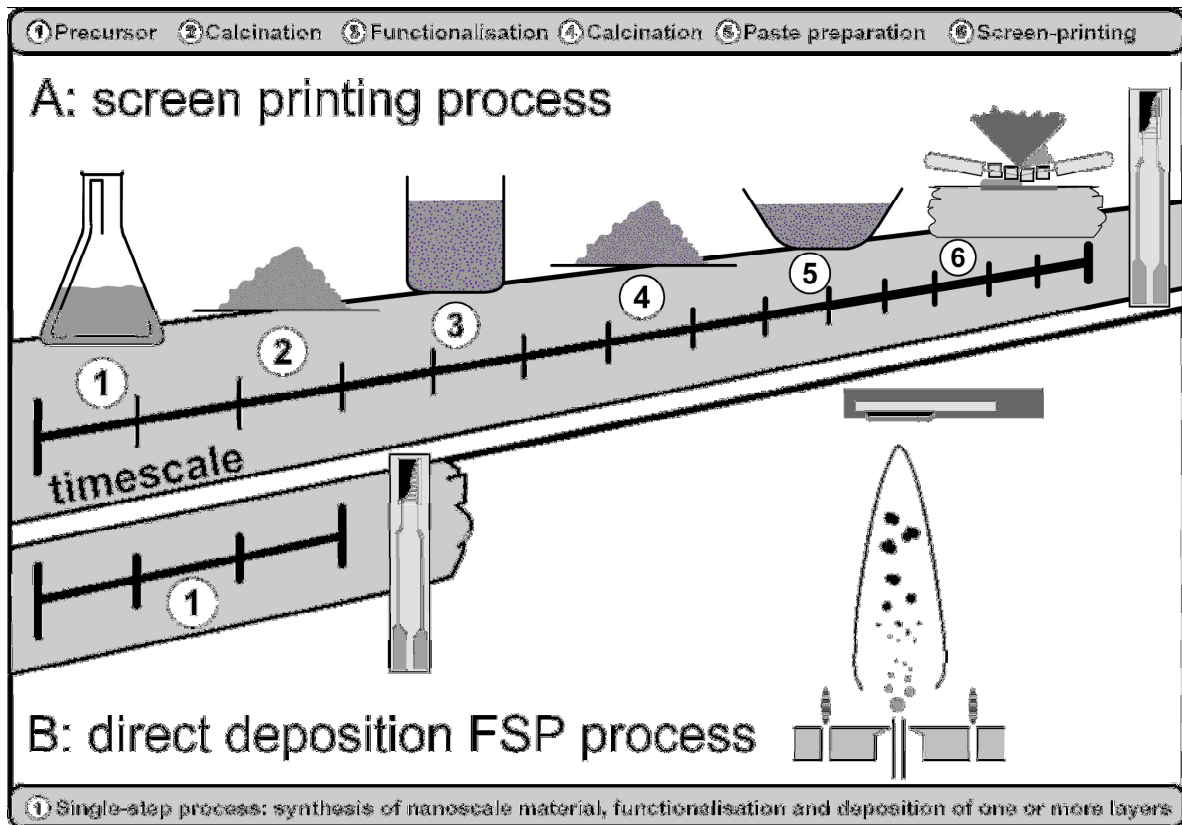
Figure 1: Scheme of deposition techniques. The screen printing process requires several time consuming steps (A), whereas the direct deposition of FSP made nanoparticles demonstrates a fast single-step process of a fully functional sensor fabrication method (B).

Complementary, the achieved sensors were subjected to a more fundamental investigation to get some insight into the sensing reactions and the underlying solid-gas interactions at the surface of the metal oxides. It is important to not only develop gas sensors by a trial-and-error approach but to understand what is going on on a molecular level. Unfortunately, the adsorption and desorption processes of a specific analyte on a certain metal oxide (e.g. the sensing mechanism of CO on SnO_2 sensors) is not an invariant and unique reaction path but depends on many factors, among them the applied technology for SnO_2 synthesis and for deposition of the latter [24]. This is also why despite the wealth of published data on metal oxide sensors, there are many contradicting results, because sensors that were fabricated under completely different conditions and thus with a different production history are used. As a consequence, when establishing a new kind of sensor fabrication method, attempts to understand and to model the correlated sensing reactions of thus prepared sensors are of fundamental interest.

Therefore, catalytic conversion measurements were performed that allowed for a detailed analysis of the educts and products of the metal oxide-gas reactions. Especially in the case of the multilayer sensors containing a filter layer, the correlation between the rate of gas conversion and sensor signal gives insight into how much the filter layer itself contributes to the conversion of gases.

It is well known and widely accepted that most of the sensing reactions of reducing gases go via pre-adsorbed species, i.e. oxygen ions and hydroxyl groups resulting from the adsorption of oxygen and water present in the ambient atmosphere [25, 26]. The nature and extent of such species was investigated by simultaneous resistance and work function change measurements. This technique that combines two different measurement principles on one sample provides additional information that could not be achieved by applying each technique individually, i.e. localized dipolar species at the surface of the metal oxide. The improvement and confirmation of this measurement setup was carefully carried out in the context of this thesis.

The main focus of the present work is on the systematic development of a new kind of sensor fabrication technology that withstands the benchmarking with the established technologies and even delivers crucial benefits compared to the latter. The thorough investigation of thus prepared sensors is the basis for an applied research that generates the convergence of industrial needs and academic research.

2

MOX sensors: an overview

Metal oxide based semiconductor gas sensors are mainly used because they are relatively inexpensive, robust and user-friendly compared to other gas sensitive devices. Although a lot of research has been done on metal oxide gas sensors, a full understanding of the whole gas sensing process is not yet available. This is because the quantitative and qualitative properties of a metal oxide gas sensor depend not only on the oxide-gas interaction and therefore on the sensing material, but on many other elements of the sensing device and their interplay among each other. In particular, the following parts of a metal oxide gas sensor have to be considered and understood:

- the sensing material itself – The physical properties of the metal oxide determine the way in which the adsorption and desorption processes take place. The effect of additional dopants on these processes is also of fundamental interest.
- the synthesis route – The way in which the metal oxide is produced influences important parameters like grain size and defects, etc.
- the deposition method – The technology of depositing the sensing material on a substrate mainly determines the resulting layer, i.e. thickness, porosity, etc.
- the sensing device – The material and structure of the electrodes, the origin of the substrate and the working temperature affect the sensing reaction. An additional filter crucially changes the sensing behaviour of the sensor.

Furthermore, the very basic chemistry of metal oxide – specific analyte interaction on a molecular level and the influence of a catalytic filter on the latter should be studied. Therefore, the following paragraphs provide a basis for the next chapters of experimental research by summarizing the state-of-the-art knowledge about the above mentioned elements of metal oxide based gas sensors.

2.1 Sensing materials

The gas-dependant conductivity of semiconducting metal oxides is not only restricted to a few cases but rather a common feature [27]. However, the most frequently used oxides in both research and industry are by far tin dioxide (SnO_2) and tungsten oxide (WO_3). Both

complement one another as SnO_2 shows high sensor signals towards reducing gases [28, 29, 30] whereas WO_3 has its main use for detecting oxidizing gases [31, 32, 33]. Other materials that are still in the status of research and up to now almost not commercially available are indium oxide (In_2O_3), zinc oxide (ZnO), iron oxide (Fe_2O_3), or mixed oxides like iron-tin oxide (Fe_2O_3-SnO_2) and indium-tin oxide (ITO, In_2O_3-SnO_2). Table 2 displays the vast importance of SnO_2 and WO_3 in the actual research.

Table 2: Overview of the scientific contributions dealing with various metal oxides at the International Meeting on Chemical Sensors (IMCS) in 2004 and the Eurosensors XIX in 2005. (Data were collected from the proceedings of the conferences.)

	Number of contributions dealing with					
	SnO_2	WO_3	In_2O_3	ZnO	Fe_2O_3	others
IMCS 2004	73	23	4	4	6	80
Eurosensors 2005	40	26	17	5	7	36

Due to its intensive use in research and application, SnO_2 can be regarded as a prototype material for gas sensing. Therefore, every new sensor fabrication technology should be able to implement SnO_2. The present work follows this idea and tests its achieved methods with SnO_2 in order to benchmark it with the state-of-the-art technologies in both academia and industry.

2.1.1 SnO₂

Tin dioxide is not only used in the field of gas sensing but is also applied in many other fields. Besides gas sensing, the major applications for SnO_2 are: (i) as a transparent conducting oxide (TCO) and (ii) as an oxidation catalyst.

The combination of low electrical resistance and high optical transparency qualify SnO_2 for its use as a TCO. These properties are utilized as electrode material in solar cells, light emitting diodes, flat panel displays or as transparent electronics in transparent field effect transistors [34, 35, 36]. Although SnO_2 is transparent in visible light, it is highly reflective for infrared light. Therefore, it is used for coating windows to keep the heat out or in a building, depending on the climate region. The use of SnO_2 as oxidation catalyst has been

reported many times in the past, e.g. for CO oxidation [37] or NO oxidation [38]. Not least due to these many applications, there are several review articles that describe the structural and electronic properties of SnO_2 in detail [39, 40].
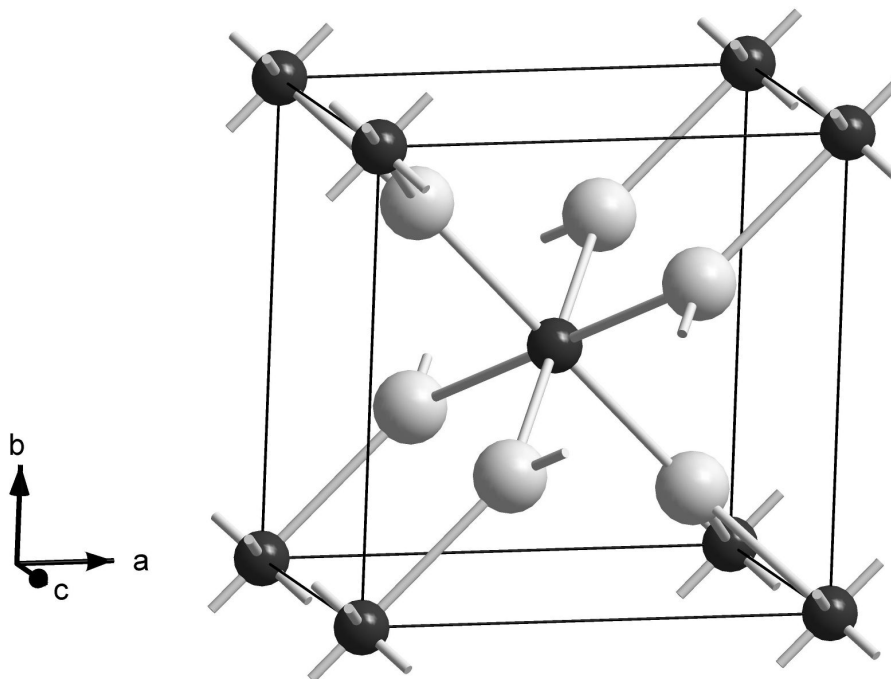
Figure 2: Unit cell of SnO_2. The tin atom (black) is octahedrally surrounded by six oxygen atoms (grey). The unit cell was created according to the crystal parameters reported in [41].

In nature, tin dioxide can be found as cassiterit crystallizing in a tetragonal rutile structure (Figure 2). Six oxygen atoms are grouped around every tin atom. SnO_2 in its stoichiometric form is a wide band-gap material with $E_g = 3.5$ eV and therefore a good insulator. However, nonstoichiometry (in particular oxygen vacancies) makes it a semiconductor under normal conditions, because the formation energy of oxygen vacancies and tin interstitials is very low [42]. For single ionized oxygen vacancies the donor level is $E_{D1} = 0.035$ eV and for double ionized oxygen vacancies $E_{D2} = 0.14$ eV below the conduction band edge [43]. The electrons of the donor levels can be easily donated to the conduction band making SnO_2 an n-type semiconductor. It is well known that the SnO_2 (110) is the thermodynamically most stable surface [44]. The rows of bridging oxygen ions can be removed easily to create a reduced surface with Sn^{2+} ions

(see Figure 3 and Figure 4). However, the removal of those bridging oxygen rows does not provide additional donor levels in the band gap [45].
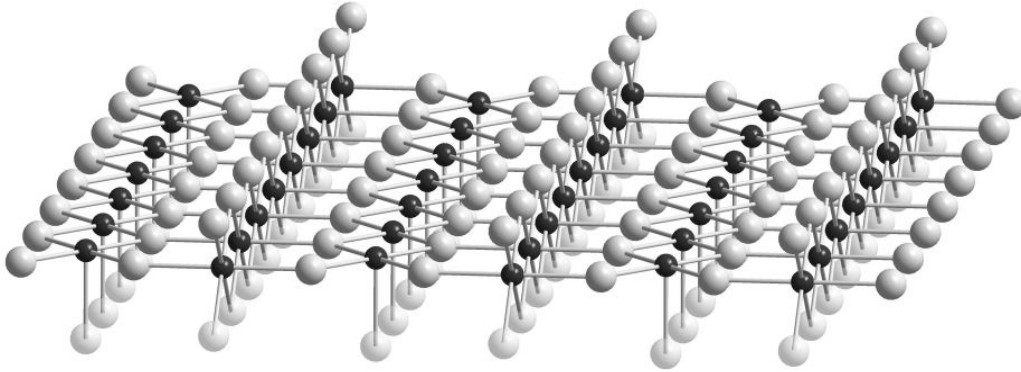
Figure 3: Ideal SnO_2 (110) surface. The surface was created according to the crystal parameters reported in [41].
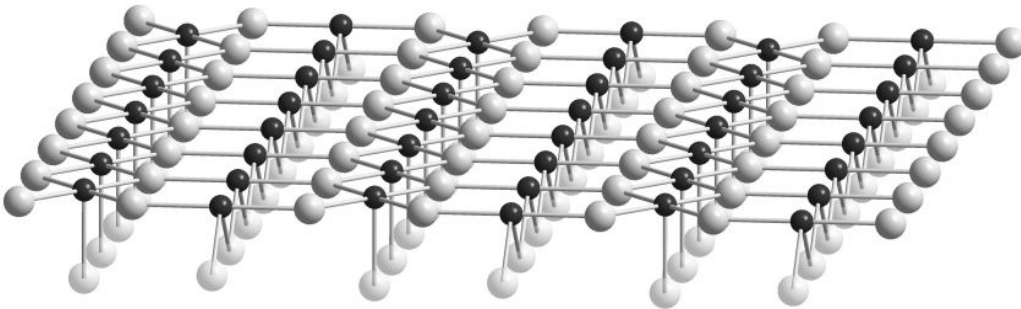
Figure 4: Reduced SnO_2 (110) surface. The surface was created according to the crystal parameters reported in [41].

As mentioned before, the presence of defects (oxygen vacancies) causes that pure SnO_2 exhibits gas sensing properties by itself. However, in practice additives or dopants are often introduced to increase the sensitivity and selectivity towards certain gases. A basic understanding of the underlying principles in gas sensing will be discussed in the next two paragraphs.

2.2 SnO_2 – gas interaction

The typical measurement technique for metal oxide sensors is the measurement of conductance or resistance. Thereby, changes in its overall resistance are attributed to the interaction with adsorbed molecules. It is well known that surface charge affects the band

structure of a semiconductor [46, 47]. The capture of electrons or holes at the surface has a strong effect on the surface barrier qV_s. In this context "surface" is the region of the solid in which the band structure is influenced by an adsorbate.

There are different ways in which a gas molecule can be adsorbed at the surface of a semiconducting metal oxide like SnO_2. However, there is no consistent definition of these adsorbed species in literature, and scientists talk about the latter in a different manner. Briefly, one distinguishes: (i) between physisorbed, chemisorbed and ionosorbed species [25], (ii) between "weak chemisorbed" and "strong chemisorbed" species [48, 49], or (iii) between "neutral" and "charged" adsorbed species [50]. The present work tries to keep to the first approach of physisorption, chemisorption and ionosorption. It is important to have a clear understanding of the physical meaning that these different phrases have for the characteristics of a semiconductor, i.e. work function, band bending and electron affinity. From this point of view, there are two different kinds of adsorbed species.

- The species having an influence on band bending and thus on electrical conductivity are regarded as ionosorbed species (this would correspond to "charged" or "strong chemisorbed" in the other denotations). Their total amount is limited to 10^{-5} to 10^{-3} monolayer (the so-called Weisz limitation [51]). Ionosorbed species undergo a delocalized charge transfer with the semiconductor, i.e. the counter charge of the ionized adsorbate at the surface is delocalized within a depletion layer or an accumulation layer in the metal oxide and thus changes the concentration of the free charge carriers in the conduction band near the surface.

- The species which do not influence the electrical conductivity of a semiconducting metal oxide are regarded as physisorbed or chemisorbed surface species, which means that they do not end up as adsorbed ions. The difference between physisorption and chemisorption is in the strength of the resulting bond between adsorbate and the solid. Physisorption displays weak Van-der-Waals forces, whereas chemisorbed molecules form covalent bonds with surface sites of the solid. However, in both cases they undergo a localized charge transfer. The latter influences the electron affinity of an oxide. To put it differently, it causes a

potential drop across an electric double layer created by the adsorbed molecule and the surface. This local charge transfer is equivalent to the creation of an effective dipole.

To summarize, changes in band bending are only induced by surface species which contribute to a delocalized charge transfer with the conduction band, whereas changes in the electron affinity are due to adsorbed species with a localized charge transfer and thus under building of dipoles with the surface. Therefore, the work function of a semiconductor will be influenced by both kinds of adsorbed species. The influence of localized and delocalized charge transfer on the band structure of an n-type semiconductor like SnO_2 is sketched in Figure 5.
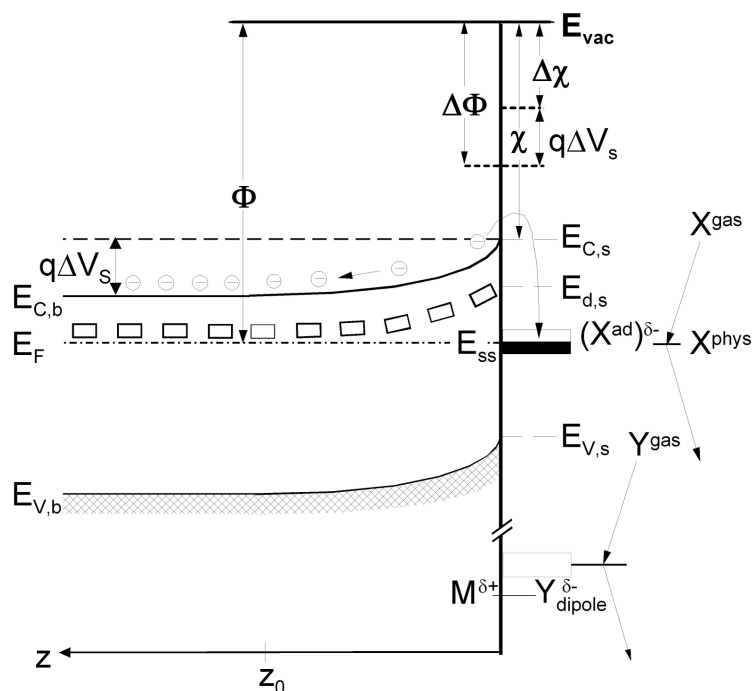
Figure 5: Band model of an n-type semiconductor. Ionosorption of molecules at the surface (X_{ad}) leads to a bending of the bands ($q\Delta V_s$), and the building of dipoles at the surface ($M^{\delta+}–Y^{\delta-}$) changes the electron affinity ($\Delta\chi$). Both changes determine the change in work function ($\Delta\Phi$).

Most gas sensors consist of porous thick films out of many polycrystalline SnO_2 grains that contact each other. According to the model of Bârsan et al [19], in such material the conduction process through the sensing layer can be described by the above mentioned theory of surface barriers due to interaction with adsorbed gases. Thus, the free charge

carriers (electrons in the case of SnO₂) have to overcome the intergranular barriers of height $q\Delta V_s$ formed by band bending at the surfaces of neighbouring grains. The height of the barriers, and hence the occupancy of surface states, can be altered by the adsorption of the molecules from the gas phase. The corresponding conductance G or resistance R may formally be described by Equation 1:

$$\frac{G_F}{G_I} = \frac{R_I}{R_F} = \exp\left(q\,\frac{\Delta V_S}{kT} \right) \tag{1}$$

where G_I and R_I denote the conductance and the resistance in the absence, and G_F and R_F the conductance and the resistance in the presence of the analyte. $q\Delta V_s$ represents the change in band bending due to the interaction with the analyte. Therefore, ionosorption of gas molecules at the surface of SnO₂ grains is directly connected with a change of the overall resistance of the sensing layer. The effect of the most prominent gases for real life applications – i.e. oxygen and water – and of the analytes that are object of this study – i.e. methane, carbon monoxide and ethanol – on the conduction process of polycrystalline SnO₂ layers will be discussed in the following.

2.2.1 Oxygen

As in most cases oxygen is present in the gas atmosphere, the effect of oxygen on the band structure of SnO₂ has to be taken into account. Often, the reaction of other analytes with the surface of metal oxides goes via a reaction with pre-adsorbed oxygen species and thus is rather an indirect interaction with the solid.

Despite many studies, the nature and origin of oxygen species and also the mechanism by which the interplay between O₂ and the SnO₂ surface occurs is still very poorly understood. The generally accepted model of O₂-SnO₂ interaction considers both molecular and atomic adsorbed surface oxygen species (for an overview of surface oxygen species on SnO₂ see [17, 25, 26]). However, there is no agreement on the physics and chemistry of the oxygen adsorption. There is consensus that the nature of the oxygen surface species depends on the temperature, i.e. oxygen adsorbs on SnO₂ non-

dissociatively in a molecular form (either neutral $O_{2(ads)}$ or charged $O_{2(ads)}^-$) at lower temperatures (< 150-200°C), and at higher temperatures it dissociates into atomic oxygen (either neutral $O_{(ads)}$ or charged $O_{(ads)}^-$). This model for oxygen interaction with SnO_2 is based mainly on phenomenological measurements, e.g. conductance and TPD (Temperature Programmed Desorption) [26, 52, 53]. There are only few direct spectroscopic observations of surface oxygen species ($O_{2(ads)}$, $O_{2(ads)}^-$, $O_{(ads)}^-$). Charged molecular oxygen species ($O_{2(ads)}^-$) have been detected in many works [52, 54, 55, 56] by Electron Paramagnetic Resonance Spectroscopy (EPR or ESR). However, the identification of charged atomic oxygen species ($O_{(ads)}^-$) by EPR [57] is inconsistent with the rest of EPR studies and appears to be due to a misinterpretation of EPR results [54].

A localised interaction associated with a formation of surface dipoles between surface tin atoms and oxygen molecules was identified by IR spectroscopy [58, 59]. However, this interpretation is not commonly accepted [54, 60]. In the case of XPS, deconvolution and interpretation of the O 1s peak in the spectra is very controversial, i.e. many interpretations are possible (e.g. adsorbed OH, C-impurities, CO_2, H_2O). Moreover, the SnO_2 surface changes considerably due to the UHV conditions (< 10^{-9} mbar).

Complementary information about adsorption sites as well as geometries of adsorbed oxygen species can be gained by theoretical (quantum chemical) calculations [61, 62, 63, 64, 65, 66]. However, they have been done for the oxygen-SnO_2 interaction at 0 K and should be regarded very carefully. This means that the stability of different forms of adsorbed oxygen at operating temperatures – 150 to 450°C – can significantly differ from the ones predicted by calculations. Moreover, the theoretical calculations are restricted to neutral species, i.e. the presence of charged species is not clear from DFT calculations. To be very brief, on the SnO_2 (110) surface the following adsorbed oxygen species are described:

- molecular adsorption – End-on O_2 coordination to 5-fold Sn site (Sn_{5f}^{4+}).
- molecular adsorption – Side-on O_2 coordination to a pair of 4-fold reduced Sn-sites (Sn_{4f}^{2+}). The oxygen molecule will pick up the electronic charge associated with reduced Sn^{2+} ions, becoming a peroxide molecule ($O_{2(ads)}^{2-}$).

- dissociative adsorption – Filling the bridging oxygen vacancies with atomic oxygen.

- dissociative adsorption – O coordination to 5-fold Sn site (Sn_{5f}^{4+}).

As one can see, the general picture of O_2 interaction with SnO_2 is still far from understanding and there are still large pieces of the puzzle missing to get a full understanding of oxygen interaction with SnO_2 surfaces.

2.2.2 Water

For many applications, water is present as background humidity. Therefore, water molecules might act as interferants with regard to other analytes. A lot of research on water adsorption on solid surfaces has been done and can be found in detail in several review papers [67, 68]. Different authors developed models for the interaction of water and metal oxide surface. For example, one model proposes that homolytically dissociated water forms a rooted OH-group and a terminal OH-group [69]. This can be formally described by Equation 2:

$$H_2O^g + Sn_{Sn} + O_O \rightarrow Sn_{Sn} - OH + \left(O_OH\right)^+ + e^- \tag{2}$$
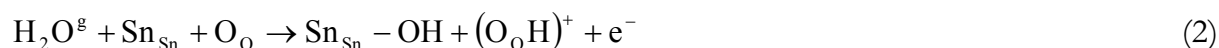
In this context, "terminal" denotes an OH-group that is bond to a tin atom and "rooted" denotes an OH-group where a hydrogen atom is bond to a lattice oxygen atom. The rooted OH-group can act as a donor under release of an electron ($q\Delta V_s < 0$), whereas the terminal OH-group builds up a local dipole $Sn^{\delta+}-(OH)^{\delta-}$ ($\Delta\chi > 0$).

On the basis of conduction measurements a model was proposed where an interaction of homolytically dissociated water and adsorbed oxygen species leads to two terminal OH-groups [70, 71]. Recently, Koziej et al [72] supported the latter model by spectroscopic methods, i.e. DRIFT spectroscopy. An increase of hydroxyl groups on a SnO_2 surface was observed with increasing oxygen concentration. This was interpreted as an interaction of water and adsorbed oxygen species and the following mechanism was proposed:

homolytically dissociated water forms via an ionosorbed oxygen two terminal OH-groups (see Equation 3).

$$H_2O^g + 2\,Sn_{Sn} + O_{ad}^- \rightarrow 2\,Sn_{Sn} - OH + e^- \tag{3}$$

The same reaction might occur not via adsorbed oxygen but via lattice oxygen leading to two terminal OH-groups and an oxygen vacancy (see Equation 4) [69].

$$H_2O^g + 2\,Sn_{Sn} + O_O \rightarrow 2\,Sn_{Sn} - OH + V_O^{\bullet\bullet} + 2e^- \tag{4}$$
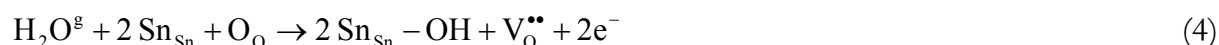
Others suggest a competitive adsorption of water molecules and oxygen where the presence of water blocks the adsorption sites for oxygen adsorption [27, 73]. However, despite many studies and proposed models, the interaction of water with SnO_2 is not yet clarified. Rather, it is not a unique reaction path but depends on the origin and the history of the metal oxide [68, 74].

2.2.3 Methane

The adsorption and subsequent oxidation of methane on metal oxide based catalysts and sensors has been studied intensively. It is reported that the initial step in the oxidation of CH_4 is the abstraction of an H radical followed by further reactions of the CH_3 radical [75, 76]. The latter is a very reactive species so that the reaction rate of breaking the first C-H bond regulates the sensing reaction. There are two different pathways proposed for the further reaction steps [77]: (i) oxidation by further abstraction of hydrogen and formation of CO_2 and water and (ii) recombination of two methyl radicals and abstraction of hydrogen under formation of ethene (C_2H_4).

2.2.4 Carbon monoxide

The detection of CO with SnO_2 based gas sensors is the topic of many studies [20, 30, 78]. The reason is twofold: (i) CO is an "easy" molecule where the reaction path of the oxidation to CO_2 is expected to be relatively manageable and (ii) the detection of

CO is of great interest for many applications. In dry conditions it is generally accepted that CO reacts with pre-adsorbed oxygen to form CO_2 (Equation 5).

$$\beta \cdot CO^g + O_{\beta\,ad}^{-\alpha} \rightarrow \beta \cdot CO_2^g + \alpha \cdot e^- + S \qquad\qquad (5)$$

where β is equal 1 for atomic and 2 for molecular oxygen and α is equal 1 for single and 2 for double ionized oxygen species, respectively. However, as intermediates different forms of carbonates and carboxylates have been identified [60, 79, 80]. The presence of humidity affects the sensing of CO drastically and is contradicting in literature. Some authors report a strong enhancement of the sensor signal [71], whereas others show a decrease for CO sensing in the presence of humidity [81]. The enhancement is explained either by a direct reaction of CO with hydroxyl groups or by water increasing the reaction between oxygen and CO [71, 82]. The suppression of CO sensing in the presence of humidity is explained by a competitive reaction between water and oxygen for the same adsorption sites [81].

2.2.5 Ethanol

The adsorption of ethanol (C_2H_5OH) on the SnO_2 surface has not very often been investigated in detail. Most authors are content with reporting the sensing behaviour towards ethanol without discussing the underlying reaction mechanisms. However, several TDS (thermal desorption spectroscopy) investigations give some insight into the reaction products and intermediates of the ethanol – SnO_2 interaction [75, 83].

Intermediate products of the total oxidation of ethanol on SnO_2 are acetaldehyde, ethylene and CO, the final desorbing products are CO_2 and water. The ethanol molecule is expected to be bound in a first reaction step with the oxygen to a tin atom of the lattice under abstraction of a hydrogen atom.

All the above described models try to explain the interaction of certain gas molecules with the SnO_2 surface. As mentioned, in most of the cases even this is a difficult task and object of many controversial discussions. However, the sensors used for applications

mostly consist of SnO_2 layers doped with different noble metals. These dopants have a crucial influence on the sensor performance and thus also on the underlying metal oxide – gas reaction path. Therefore, their contribution to the sensing process has to be taken into consideration.

2.3 Effect of doping

In order to improve the behaviour of a sensor, it is common to test whether additives, so-called dopants, can give further benefit. Therefore, doping tin dioxide became more and more important as research activities were heading for the enhancement of application properties [84, 85, 86]. Additives often used are noble metals such as platinum (Pt) or palladium (Pd) due to their catalytic activity towards specific gases. Varying dopants and their concentrations allows tuning the sensing behaviour significantly, e.g. leading to a higher sensitivity or selectivity, shorter response or recovery times or improved stability. Generally, it is assumed that the added noble metals form isolated clusters on top of the metal oxide grains. Therefore, this kind of sensitization is rather a loading of the SnO_2 surface than a bulk doping by incorporation into the metal oxide lattice.

With regard to understanding the reaction mechanisms at the surface, doping metal oxides means taking into account additional models which are able to reflect the influence of those dopants. The most important of these models described in literature [86, 87, 88] are summarised in Figure 6. For the (i) "spill-over effect" the dopant supports the activation and dissociation of molecules into those reactive species that are taking part in the sensing reaction at the SnO_2 surface and thus enhances the latter. In the case of a (ii) "Fermi level control" gases partially oxidize the metal clusters by trapping electrons. As the dopant and the SnO_2 are in electrical equilibrium, also the Fermi level of the SnO_2 will be influenced leading to a depletion region at the interface of metal and oxide. Furthermore, (iii) catalysis can take place directly at the metal clusters which does not influence the conductance of the sensing layer.
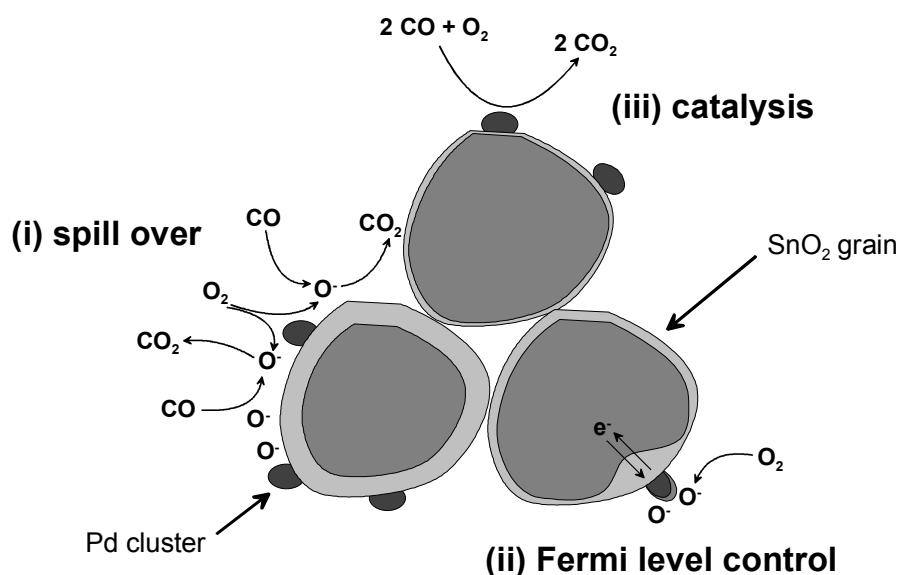
Figure 6: Effect of doping. (i) The metallic dopant promotes the dissociation of gas molecules which diffuse to the metal oxide surface and thus enhances the sensing reaction. (ii) The amount of oxidization of the metallic clusters influences the Fermi level of the semiconductor and thus the depletion layer at its surface. (iii) If catalysis takes place on clusters of the dopant, the conductance of the metal oxide stays unaffected.

It is not always clear but rather a matter of debate which of these models describes a certain analyte / noble metal / metal oxide system best. In this study, platinum and palladium were used for doping the SnO_2. Yamazoe et al concluded that the spill-over mechanism dominates for Pt, whereas the Fermi level control determines the interaction with Pd [86, 89]. In the case of Pd this assumption is supported by the finding that under atmospheric conditions palladium is present as PdO [90, 91, 92]. Thus, the larger work function of PdO compared to SnO_2 causes an electron depletion zone in the SnO_2 at the interface.

2.4 Synthesis of metal oxides

The core of each sensor fabrication process is the synthesis of the gas sensitive material itself. Often, selecting a certain method already predefines many parameters and thus many of the properties of the final device, e.g. thin or thick film layers, lateral dimensions of the sensing layer area or morphology. In principle, there are synthesis routes that (i) are not necessarily linked to a certain deposition method and those that (ii) include metal

oxide synthesis and deposition method in one technological process, e.g. vapour deposition methods. The latter will be discussed in the next chapter, which deals with deposition methods. Here, classical ways of metal oxide powder synthesis will be presented.

Polycrystalline SnO_2 for gas sensors is usually prepared starting with metallic tin, tin oxide, salt solutions (mostly $SnCl_4$) or organo-tin compounds. However, the first two require total oxidation of the tin under rough conditions and are therefore not commonly used. Easier to deal with and with a diversified spectrum of synthesis routes are the wet chemistry methods. Here, aqueous solutions of tin salts form a sol with SnO_2 clusters. This stabilised solution can either be precipitated and filtered to get the polycrystalline SnO_2 powder, or it can be transferred into a gel with growing of the clusters in the stable solution and finally reach a precipitation of the powder. In both cases, the final calcination step of the powder will determine the grain size of the material. This so-called sol-gel process has been well investigated and reported in detail [93, 94, 95]. There is also a sol-gel process reported that starts from Sn(II) [96]. One big advantage of the sol-gel route is the capability to introduce additives (dopants) to the sensing material during the synthesis process. These additives are noble metals in form of clusters on the surface of the SnO_2 grains. There are different ways to introduce the dopants:

- impregnation – The SnO_2 is mixed with a noble metal salt (e.g. $PtCl_4$ or $PdCl_2$) and then subjected to a further heat treatment.
- colloidal method – A dispersion of metal particles is mixed with the SnO_2 which is expected to adsorb the metal particles on its surface.

Thus prepared pre-processed metal oxide powder is the base material for commercial sensor production as it is relatively simple, cheap, compatible with mass production, and can be used as a source for the standard deposition method of commercial sensors, i.e. screen printing. There is another method that leads to functionalized metal oxide powders. This method is based on aerosol technology and is called flame spray pyrolysis (FSP). It will be described in detail in another section (chapter 2.7) as the FSP process is the main technological focus of this work.

Recently, there have been some new trends in fabricating materials for gas sensing and a lot of research activity has been devoted to developing nano- and meso-crystalline materials. Most effort has been done to synthesize nanowires, nanobelts or nanotubes of metal oxides [97, 98, 99, 100]. The vision of the scientists is to have a conducting nanowire without grain boundaries in the longitudinal direction between the electrodes of a sensing device. Another trend is the creation of a nanocrystalline metal oxide material with a mesoporous structure or a controlled microstructure [101, 102, 103, 104]. Although these research activities are very promising, they are far from being ready to be commercially exploited for gas sensing.

2.5 Deposition methods

To build up a gas sensor, it is obvious to not only have the sensing material itself but to also implement a method of depositing the sensing material on a sensor substrate. The methods that are currently used for the deposition of metal oxides on sensor substrates can be classified into the following groups:

- vapour deposition (physical vapour deposition or chemical vapour deposition);
- sol-gel based methods;
- classical methods for thick films.

These different technologies all have their own advantages and disadvantages and will be discussed briefly in the following sections. A short overview is sketched in Figure 7 and details are described in different textbooks [105, 106].
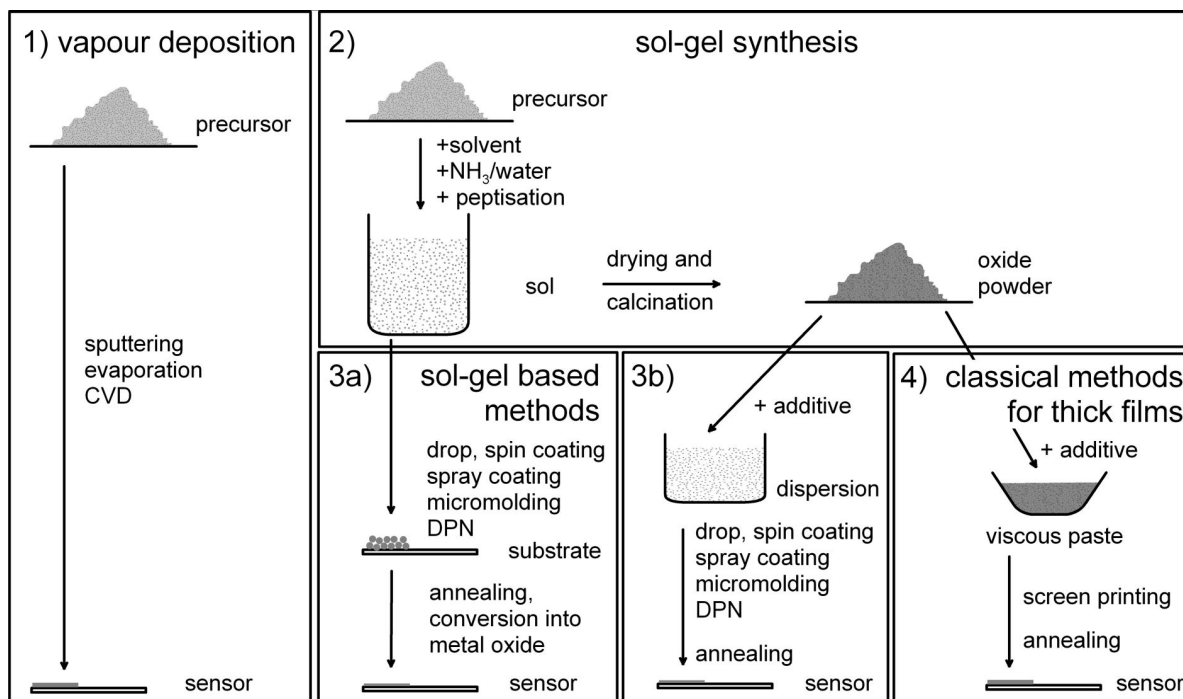
Figure 7: Different deposition methods. Physical or chemical vapour deposition combines the synthesis and the deposition of the metal oxide in one step (1). Other methods require an initial synthesis step, e.g. sol-gel (2). Usually, techniques like spray coating, drop coating or spin coating start with a sol (3a), but can in principle also be used with stable metal oxide generated solutions (3b). Screen printing is the classical method for thick film sensor preparation (4).

2.5.1 Vapour deposition

Vapour deposition is a well known method in semiconductor processing as it is a clean and well controllable method. Two important parameters are always the partial pressure (of the evaporated gas and of a reactive gas) and the temperature of the substrate. Usually, physical vapour deposition (PVD) needs low partial pressure (for a long mean free path) and chemical vapour deposition (CVD) needs a higher substrate temperature (to deliver the activation energy for the reaction of the precursor material).

PVD techniques are based on sputtering or evaporation and their combination with photolithographic technologies belongs to the classical methods in microtechnology. There are many different ways of deposition, e.g. thermal or electron beam evaporation, dc sputtering, rf sputtering; however, the main limitations are the temperature of deposition, the maximum for the thickness of the sensing layer and the stoichiometry of

the sensing material. Additionally, introducing dopants is rather difficult or even impossible. In CVD the sensing film is formed by thermal decomposition of gaseous molecules on hot substrates. Limitations of CVD are related to the choice of suitable precursors, the reagent gas composition and the precursor partial pressure to control the composition and the microstructure of the deposited films [107]. None of the vapour deposition methods allows the use of pre-processed and functionalized oxide powders for deposition.

2.5.2 Sol-gel based methods

Sol-gel techniques require a stable dispersion or suspension of metal oxide precursors as described in chapter 2.4 that can be used for the deposition on substrates. After the solution has been successfully brought onto the substrate, the evaporation of the solvent and the transition into the final metal oxide layer takes place by heating. The deposition itself can be performed by several methods. For spray coating, a sol is sprayed on the substrate by using a spray gun that is moved over the substrate. Spray coated layers show disadvantages with regard to layer homogeneity and roughness. When spraying droplets on the substrate, droplets with very different sizes and therefore chemically different compositions reach the sensor substrate leading to an inhomogeneous layer. In the case of drop coating, a drop of a stable suspension is put locally on the surface of the substrate. This is done with a micropipette or a microinjector. Here, it is important to control the adhesion properties of the substrate so that the droplet wets the substrate well. Obviously, it is rather difficult to achieve a uniform layer thickness all over the covered sensing area. Spin coating tries to solve this problem by spinning the substrate after a drop of the sol was deposited on it. The spin rate and the viscosity of the sol offer a possibility of varying the layer thickness of the final sensing layer.

Recently, there have been some new approaches in depositing sol-gel based solutions. At the moment they are not applicable for commercial exploitation. The first one is micromolding in capillaries. This technique belongs to the soft lithographic methods. A patterned mold is placed on a substrate with the capillaries opened at one side. Applying a droplet of a colloidal dispersion leads to a spontaneous filling of the capillaries [108]. The

second one is dip-pen nanolithography (DPN). This method is based on the controlled transfer of ink from an ink coated tip of an atomic force microscope (AFM) to a substrate [109]. In principle, all the methods described here can also be performed starting with a pre-processed and functionalized metal oxide powder instead of the sol. In that case, one has to prepare a stable aqueous solution of the oxide powder first [110].

2.5.3 Classical methods for thick films

Screen printing is a very versatile technique that is therefore used in many different industries. The basic principle is always that a screening ink is put on top of a screen with a mask that covers all the areas of the substrate that should not be covered by the ink. Then, a squeegee (rubber blade) is used to push the ink evenly into the screen openings and onto the substrate. The ink passes through the open spaces in the screen onto the substrate below; then the screen is lifted. In the case of colour ink, one can print on a variety of materials, such as textiles, ceramics, metal, wood, paper, glass, and plastic. Another important application of screen printing is the fabrication of printed circuit boards in electronics. The enormous advantages of screen printing are its cheapness and the compatibility to mass production.

Today, most of the commercially available metal oxide gas sensors are fabricated in screen printing technology. Here, the screening ink has to be made by mixing the pre-processed and functionalized metal oxide powder with an appropriate organic carrier. The aim is to achieve a homogeneous and viscous paste with a high metal oxide loading that passes smoothly through the screen. In a final annealing step the organic carrier can be removed. Recent developments in this field also allow the deposition onto fragile micromachined substrates [111, 112].

In summary, most of the above mentioned deposition techniques need an appropriate mask for the deposition of a sensing material only onto a certain area of the substrate, i.e. a shadow mask for CVD, sputtering and evaporation methods, a screen for screen printing, a patterned mold for micromolding. Only the methods based on drop coating, i.e. drop coating itself, spin coating, dip-pen nanolithography, do not require the

additional step of patterning or masking. Actual and future research in the field of deposition techniques has to face the increasing demands for miniaturisation in gas sensing. Therefore, these techniques should be compatible with micromachining technologies (MEMS) and with the integration onto CMOS transducers.

2.6 The role of filters

As already described in chapter 2.2, a variety of organic and inorganic gaseous compounds interact with metal oxides – or more precisely with pre-adsorbed oxygen species – and thus influence the conductance of the metal oxide. However, in many applications just one single gas or only few gas compounds should be detected by the gas sensor. The lack of selectivity is the largest limitation of metal oxide gas sensors. Interfering gases – even if only in trace amounts – and changes in the background level of humidity can significantly affect the sensor signal, causing an uncertainty in interpreting sensor data [20].

Increased selectivity can be gained to certain extent by different approaches:

- fine-tuning of the sensing material – Varying the morphology of the metal oxide, dopants, geometry of the contacts, operating temperature, or mode of operation can increase the selectivity to certain gases.
- use of filters – By forcing gas molecules to pass a filter, the composition of a gas mixture can be altered and thus cross-selectivity can be diminished.
- use of sensor arrays – The interpretation of several nonselective or partially selective sensors using multi component analysis or pattern recognition can improve gas selectivity for certain applications.

The first approach – optimizing sensing material, dopants, temperature – is part of the present work although not directly addressed as main focus but rather a subliminal topic when improving the new sensor fabrication method developed here. The last approach – using sensor arrays – is no topic here as this work concentrates on easy-to-build and easy-

to-use sensing devices. The possibilities of using filters and the impact they have on the sensing behaviour are a major topic of this research as the deposition of filter layers was successfully implemented in the sensor fabrication process.

Enhanced selectivity gained by the use of filters can be related to different fundamental working principles of the latter. Generally, filters are classified into two categories [113]. One is physical / passive filtering and the other is chemical / active filtering. For physical filters different materials are used, such as dense [114, 115] or mesoporous [116] SiO_2, zeolites [117] or charcoal [118]. They prevent certain gas molecules from reaching the sensing layer and thus increase the selectivity to gases that are unaffected by the filter. These filters are generally added as additional parts of the sensor, e.g. in the housing above the sensor chip. Chemical filters, on the other hand, eliminate interfering gases via a chemical reaction [119] or transform the analyte into a more active species [120]. Such a catalytic filter can be a porous thick film of ceramic (Al_2O_3, SiO_2,...) [121, 122] or of doped SnO_2 on both thick films [123] and thin films [124]. Additionally, metals can be used as filter layers, either incorporated in an oxide [125] or as a metallic film [126]. These filter layers are often deposited directly on top of the sensing layers or are realized by mixing it with the sensing material.

The present work implements the use of filters in an easy and feasible sensor fabrication technology and studies the fundamental impact that those filters have on the sensing mechanism.

2.7 The FSP approach

The different metal oxide synthesis routes and deposition techniques described so far summarize the achievements of scientific research regardless of potential applications and their capability for industrial exploitation. Against the background of these considerations, the importance of size control, the required large accessible surface, the desired uniformity of the material, the ability of noble metal doping and the feasibility of high

production rates put high demands on a possible production method for metal oxides in gas sensing.

Dry aerosol synthesis routes are able to fulfill these requirements [22] as tin oxide can be made readily in vapor flames from its chloride [127, 128] and from tetramethyl tin gaseous precursor with sizes down to 6 nm [129]. Porous metal oxides in the nanometer range deliver a high specific surface. Flame aerosol synthesis is used on a large scale today in the production of carbon black, fumed silica and titania pigments. However, vapor flame methods have limitations when tin oxide has to be doped with materials where only low vapor pressure precursors are available such as platinum or ceria. The present work utilizes the potential of a more versatile flame spray method. Flame spray pyrolysis (FSP) overcomes this drawback by spraying liquid precursors thus forming a spray flame where the precursor evaporates or decomposes and reacts in the gas phase, resulting in the formation of clusters which grow to nanometer-sized particles by coagulation and sintering [130]. In this way FSP is a very promising technique for sensor material fabrication since it enables primary particle and crystal size control (e.g. [131]), which is important for tailoring sensitivity [132], as well as the controlled in-situ deposition of noble metal clusters [23, 133]. It has been shown that due to the morphology of the FSP made particles the mass transfer rates in catalysis are higher compared to microporous materials because of the large specific surface area of flame made materials [23]. Furthermore, FSP bears the advantage of completely manufacturing the nanopowder in a single high temperature step without affecting the microstructure and noble metal particle size in a subsequent annealing process as it is necessary in conventional spray pyrolysis [134] or wet methods in general. The principle of this fabrication method is shown in Figure 8.

Directly after the metal oxide powder has been generated in the flame, it can be collected with the aid of a vacuum pump on a glass fiber filter. After that one has to choose an appropriate deposition method for metal oxide powder, e.g. screen printing. However, when it comes to nanosized material it is experimentally challenging to achieve a good paste for the deposition. "Good" means a homogeneous mixture with an organic carrier, a high metal oxide loading, high viscosity, and without coagulation or agglomeration.

Additionally, one has to face the principal disadvantages of screen printing deposition as already mentioned in chapter 1.1, i.e. an additional step of combining the sensing material with organic carriers and thus an increase in processing time, deposition equipment and handling.
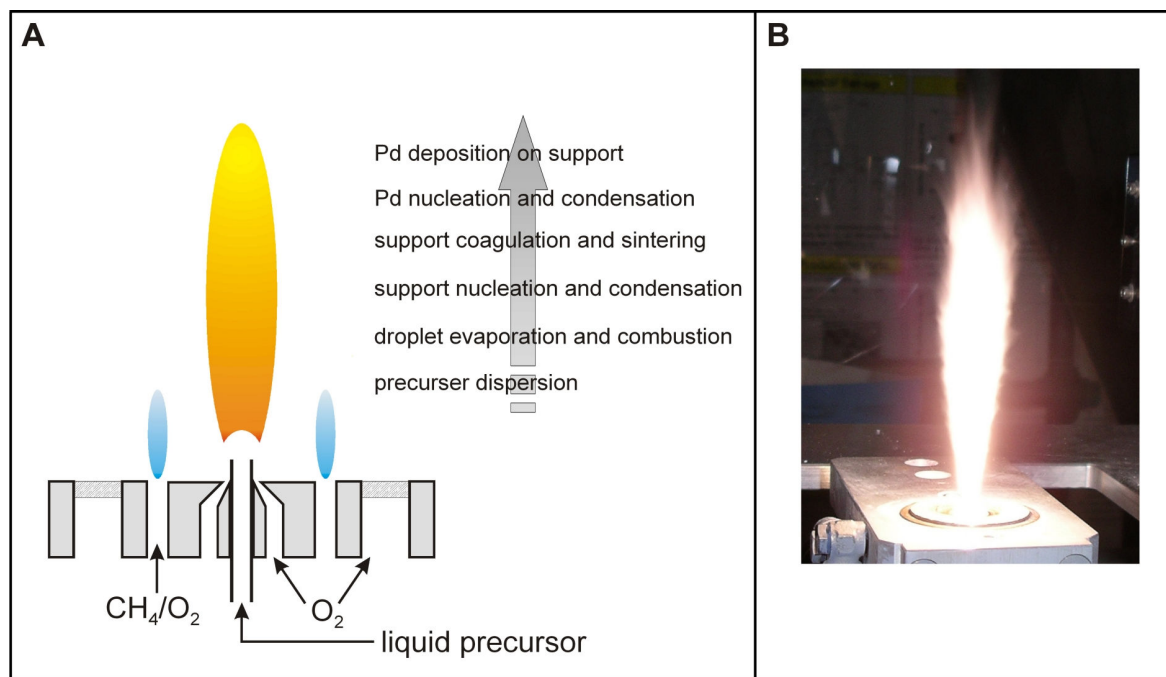

Figure 8: The flame spray pyrolysis (FSP) unit. The liquid precursor mixture is rapidly dispersed by a gas stream and ignited by a premixed methane/oxygen flame. After evaporation and burning of the precursor, particles are formed by nucleation, condensation, coagulation, and sintering (A). Image of a typical spray flame producing Pd/Al_2O_3 nanoparticles, taken from [135] (B).

To overcome these drawbacks, one can combine the FSP fabrication technology with the direct deposition of metal oxide particles from the gas phase onto sensor substrates. Direct particle deposition from vapor-fed flames has been used extensively for the production of light guide preforms and is known as vapor axial deposition (VAD) or outside vapor deposition (OVD) [136, 137]. A similar FSP deposition technology called flame spray deposition (FSD) has recently been reported for porous catalyst preparation (Au/TiO_2) and testing in micro-reactor systems [138]. In the latter, film growth rates at different deposition thickness as well as the final performance of the deposited film as a screening catalyst was reported. Also for the direct deposition of SnO_2 the use of vapor-flames has been reported [139]. However, quantitative measurements or a target

application were not reported or evaluated. Deposition by FSP at high substrate temperatures (up to 1100 °C) leads to dense films and is also called combustion chemical vapor deposition (CCVD). It has been used for the deposition of dense barium-strontium-titanate films for electronic applications such as tunable radio frequency devices [140, 141]. Single particle deposition on substrates from the aerosol phase is also reported [142, 143]. However, the direct deposition of functionalized metal oxides on smart sensor substrates and their use as gas sensors has not been reported so far. Therefore, implementing the direct deposition into the FSP process offers a novel single-step gas sensor fabrication technology. Finally, to further explore the full potential of this approach it is also possible to deposit more than one metal oxide layer subsequently on top of each other leading to a gas sensor with a sensing layer and a filter layer on top of it [144].

3

────── **Experimental** ──────

3.1 Sensor fabrication

As sensing material SnO_2 – doped or undoped – synthesized in a flame spray pyrolysis reactor was used throughout the whole studies. This base material was deposited in three different ways onto classical thick film sensor substrates: (i) direct deposition via FSP, (ii) screen printing of a viscous paste, and (iii) spin coating of an aqueous solution.

For all sensors used within this study the same substrates were used, i.e. alumina substrates with interdigited platinum electrodes on the front side and a platinum heating meander on the back side. After deposition, the sensors were annealed for 10 min in a belt oven at 500°C in air (Centrotherm Centronic DO 1600-60-D5). For screen printed and spin coated sensors this step is indispensable to get rid of additives, i.e. organic carriers for screen printing and solvents for spin coating. For the directly deposited sensors this step was also performed for reasons of comparability. However, this step is not necessarily needed from a technological point of view.
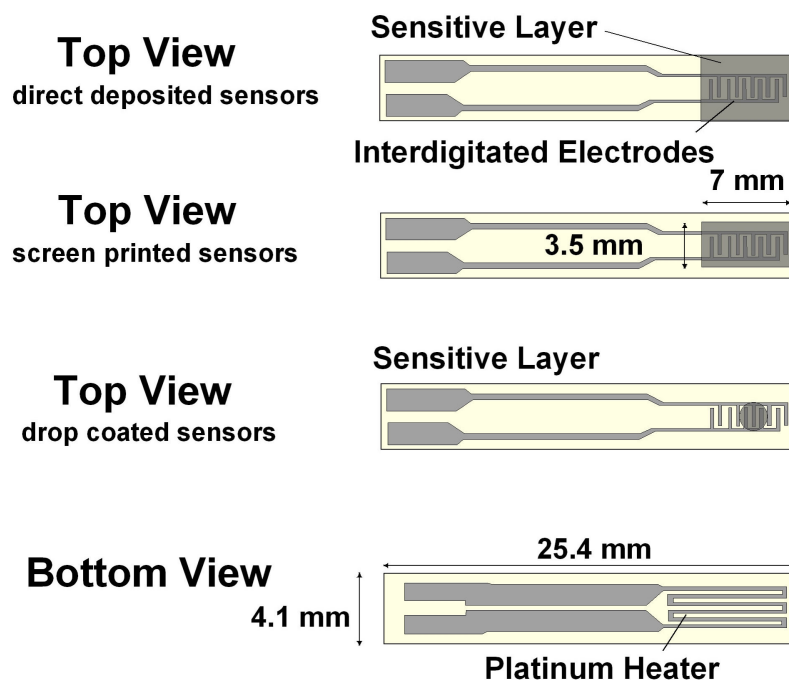

Figure 9: Sensor substrates from front side and back side. The interdigited electrode structures are covered by the sensing layer, whereas the area of the latter depends on the deposition method, i.e. direct deposition via FSP, screen printing, or spin coating. The platinum heater on the back side is used to keep the sensors at operating temperatures between 200°C and 450°C.

3.1.1 Flame spray pyrolysis (FSP)

The flame spray pyrolysis reactor [145] was used for powder synthesis and for direct deposition of the metal oxide from the gas phase. In the following, the general features of the setup are described and afterwards the specific parameters for the different synthesised powders are listed.

FSP for powder synthesis

An appropriate precursor for the desired metal oxide was diluted in an organic solvent. The precursor solution was fed into the FSP reactor by a syringe pump and dispersed by the use of oxygen into fine droplets by a gas-assist nozzle (with a controlled pressure drop at the nozzle tip). A water-cooled system avoided any evaporation of the precursor within the liquid feed lines or overheating of the nozzle. The spray flame was maintained by a concentric supporting of premixed methane/oxygen gas. In order to assure enough oxidant for complete conversion of the reactants, an additional outer oxygen flow was supplied. In the case of powder synthesis without direct deposition, the powder was collected with the aid of a vacuum pump on a glass fibre filter (GF/D Whatman, 257 mm in diameter). During the experiment, the filter was placed in a water-cooled holder, 400 mm above the nozzle, keeping the off-gas temperature below 200°C [146]. Figure 10 A shows a sketch of the FSP reactor.

Direct deposition via FSP

The direct deposition of the sensing layers on substrates was achieved by placing a home-made sample holder between the nozzle and the glass fibre filter so that the substrate was centred 200 mm above the nozzle facing it [147]. That way, simultaneously to the filter collection product, particles were directly deposited on the alumina substrates. During one production batch, eight connected and pre-cutted alumina substrates could be covered at once. Therefore, the substrates were mounted on a water-cooled copper block equipped with a K-type thermocouple to control the substrate temperature during the deposition process. The substrate temperature was maintained at $T_{sub} = 120°C$ in order to

avoid water condensation on the substrate. A mechanical mask was put on top of the substrates to allow the deposition of the particles just within the desired areas. The temperature of the flame in front of the substrate was $T_{gas} = 500°C$. Both temperatures were kept constant throughout the deposition process. This temperature difference is the driving force for the deposition of particles on the substrate leading to a thermophoretically controlled particle film growth (see Figure 10 B).
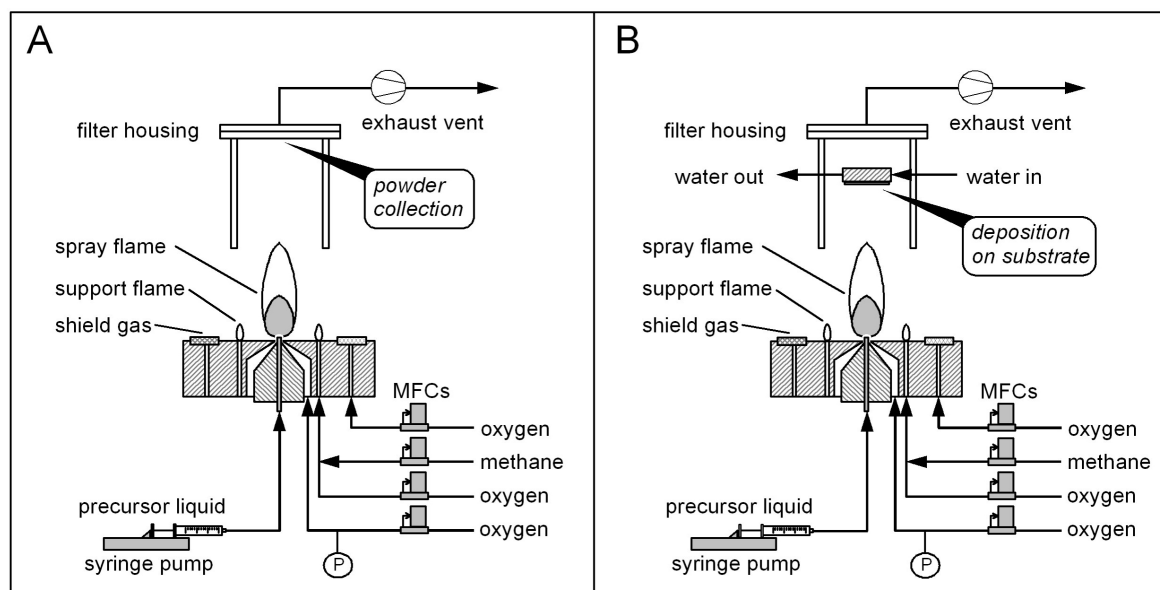
Figure 10: Metal oxide synthesis in the FSP reactor. In the standard process, the fabricated particles are collected with a glass fibre filter (A). For the direct deposition of particles from the vapour phase the substrates are mounted above the flame covered with a deposition mask (B).

As mentioned before, a precursor solution that contains all chemicals needed to achieve the desired functionalised particles has to be realized in a first step. Table 3 gives an overview over the different chemicals that have been used within this work to achieve the appropriate precursor solutions. Afterwards, this precursor solution is fed in the FSP system. Features like grain size or layer thickness in the case of direct deposition can be tuned by varying different parameters of the FSP reactor. Therefore, Table 4 shows the chosen parameters for the metal oxide synthesis and its deposition of the present study.

Table 3: Parameters and chemicals for preparation of the precursor solutions for the FSP process [146, 147, 148, 144].

product	grain size	precursor and its concentration		dopant and its concentration		solvent
A) for powder synthesis						
SnO_2	17 nm	tin(II) 2-ethylhexanoic acid (Aldrich, purity > 98%)	0.5 M			ethanol (J.T. Baker, purity > 99.9%)
SnO_2	10 nm / 19 nm	tin(II) 2-ethylhexanoic acid (Aldrich, purity > 98%)	0.5 M			toluene (Fluka, purity > 99.5%)
Pt/SnO_2	10 nm	tin(II) 2-ethylhexanoic acid (Aldrich, purity > 98%)	0.5 M	platinum acetylacetonate (Strem, purity >98%)	0.2 wt% / 2.0 wt%	toluene (Fluka, purity > 99.5%)
B) for direct deposition						
SnO_2	10 nm	tin(II) 2-ethylhexanoic acid (Aldrich, purity > 98%)	0.5 M			toluene (Fluka, purity > 99.5%)
Pt/SnO_2	10 nm	tin(II) 2-ethylhexanoic acid (Aldrich, purity > 98%)	0.5 M	platinum acetylacetonate (Strem, purity >98%)	0.2 wt%	toluene (Fluka, purity > 99.5%)
SnO_2	10 nm	tin(II) 2-ethylhexanoic acid (Alfa Aeser, purity 100%)	0.4 M			toluene (Fisher purity > 99.5%)
Pd/SnO_2	10 nm	tin(II) 2-ethylhexanoic acid (Alfa Aeser, purity 100%)	0.4 M	palladium acetylacetonate (Aldri, purity >99%)	0.02 M / 0.001 M	toluene (Fluka, purity > 99.5%)
Pd/Al_2O_3	15 nm	Aluminium-sec-butoxide (Aldrich, purity > 97%)	0.675 M	palladium acetylacetonate (Aldri, purity >99%)	0.02 M	toluene (Fluka, purity > 99.5%)

Table 4: Parameters of the FSP reactor for the synthesis of the different metal oxides [146, 147, 148, 144].

product	grain size	feed rate of syringe pump	flow of oxygen	pressure drop at nozzle tip	flow of support flame methane / oxygen		deposition time
A) for powder synthesis							
SnO_2	17 nm	8 ml/min	3 l/min	1.5 bar	1.5 ml/min	3.2 ml/min	
SnO_2	10 nm 19 nm	5 ml/min 8 ml/min	5 l/min 3 l/min	1.5 bar	1.5 ml/min	3.2 ml/min	
Pt/SnO_2	10 nm	8 ml/min	3 l/min	1.5 bar	1.5 ml/min	3.2 ml/min	
B) for direct deposition							
SnO_2	10 nm	5 ml/min	5 l/min	1.5 bar	1.5 ml/min	3.2 ml/min	30 s / 180 s / 360 s
Pt/SnO_2	10 nm	5 ml/min	5 l/min	1.5 bar	1.5 ml/min	3.2 ml/min	180 s
SnO_2	10 nm	4 ml/min	5 l/min	1.5 bar	1.58 ml/min	1.38 ml/min	300 s
Pd/SnO_2	10 nm	4 ml/min	5 l/min	1.5 bar	1.58 ml/min	1.38 ml/min	300 s
Pd/Al_2O_3	15 nm	4 ml/min	5 l/min	1.5 bar	1.58 ml/min	1.38 ml/min	300 s

Theory of film growth

Establishing the new method of direct deposition via FSP on sensor substrates, it was evident that the resulting thickness of the sensing layer depends on the deposition time, i.e. the longer the formation of particles in the FSP reactor is running the more particles settle on the substrate and thus the thicker is the final sensing layer. However, this qualitative approach is not satisfying as only a fabrication technology with tuneable and predictable features of the final sensor will achieve acceptance. Therefore, knowing the growth rate of the sensing film is necessary to enable a smart design of the process.
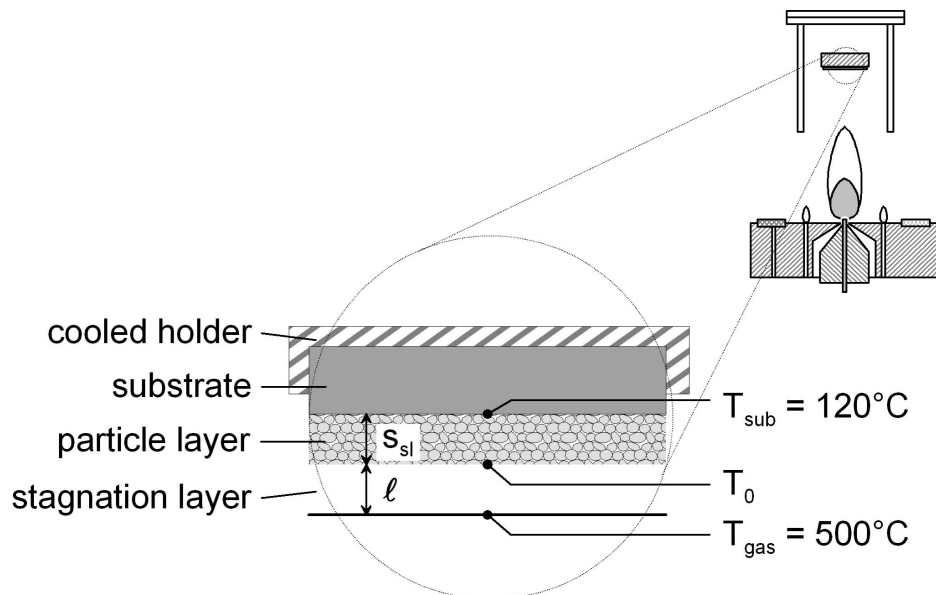

Figure 11:   Deposition process of particles from the gas phase on a substrate. The temperature of the substrate (T_{sub}) is kept constant by water cooling. The temperature of the gas (T_{gas}), which is the temperature of the hot spray flame, is also constant. The surface temperature of the particle layer (T_0) is equal to T_{sub} at the beginning of the deposition and approaches T_{gas} for large layer thickness (s_{sl}) because the growing porous particle layer has a low thermal conductivity.

A model that describes the growth rate and the thickness of the deposited film was developed specifically for the FSP direct deposition setup used in this work [147]. This simplified model only takes into account thermophoresis and diffusion as driving forces for the deposition of particles. Other possible deposition mechanisms are excluded, i.e. interception, impaction, gravitational, and electrical field forces. Figure 11 shows the simplified situation in front of the substrate. The model assumes a constant stagnation gas

layer (ℓ) in front of the substrate in which particle transport by axial convection is smaller than transport by thermophoresis and diffusion. A linear particle concentration and temperature profile is assumed within the stagnation gas layer (ℓ). The temperature on the substrate layer / gas interface (T_0) increases with increasing porous layer thickness (s_{sl}) because of heat transfer limitation in the porous layer. Therefore, the temperature gradient within the stagnation gas layer (ℓ) changes as the particle layer grows. Consequently, the driving force for the deposition (thermophoresis) will decrease (and thus also the growth rate (ξ_{dep})) with increasing porous layer thickness. The substrate holder was kept at a constant temperature (T_{sub}) while the heat flux q through the gas and particle layer were equal (Equation 6):

$$q_{gas} = \frac{\lambda_{gas}}{\ell}\left(T_{gas} - T_0\right) = \frac{\lambda_{sl}}{s_{sl}}\left(T_0 - T_{sub}\right) = q_{sl} \tag{6}$$

From this equation the temperature on the surface of the deposit can be derived (Equation 7):

$$T_0 = \frac{\dfrac{\lambda_{gas}}{\ell}T_{gas} + \dfrac{\lambda_{sl}}{s_{sl}}T_{sub}}{\dfrac{\lambda_{gas}}{\ell} + \dfrac{\lambda_{sl}}{s_{sl}}} \tag{7}$$

The actual layer growth rate (ξ_{dep}) can be expressed with the total particle number flux (j) towards the substrate and the packing of the layer assuming spherical monodisperse particles and constant particle size (d_p) and layer porosity φ (Equation 8):

$$\xi_{dep} = \frac{ds_{sl}}{dt} = \frac{dV_{sl}}{dt}\cdot\frac{1}{A_{sl}} = \frac{dN_p}{dt}\cdot\frac{\frac{\pi}{6}d_p^3}{A_{sl}\left(1-\varphi\right)} = j\cdot\frac{\frac{\pi}{6}d_p^3}{\left(1-\varphi\right)} \tag{8}$$

In the case of the presented model, the total particle number flux (j) due to thermophoresis and diffusion can be calculated as (Equation 9; see [147] and references therein):

$$j = \frac{c_{N,0}}{\ell}\left(D_p + \frac{0.55\eta\left(T_{gas} - T_0\right)}{\rho_{gas} \cdot \dfrac{T_{gas} + T_0}{2}} \right)$$

(9)

Combining Equations 7, 8 and 9 and estimating the containing parameters properly gives a direct relationship between the layer thickness s_{sl} and the actual growth rate of the deposited layer (ξ_{dep}). Figure 12 A shows the layer growth rate due to thermophoresis and the temperature at the surface of the layer with increasing thickness. At the beginning of the deposition, the temperature of the layer surface is equal to the substrate, but it increases strongly with ongoing deposition. Therefore, the layer growth rate also decreases. Integration of the actual layer growth rate over the time delivers the dependence of the total layer thickness on the deposition time (Figure 12 B).
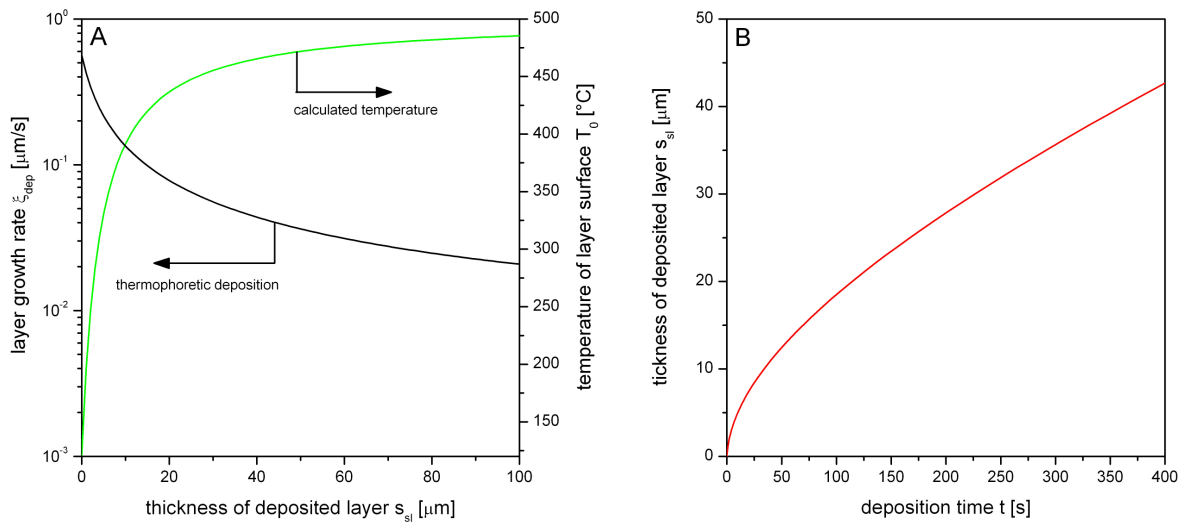
Figure 12:   Calculated layer growth. The layer growth rate (ξ_{dep}) by thermophoresis (black) and the temperature (T_0) of the layer surface (grey) are shown as a function of the layer thickness (s_{sl}) (A). The thickness (s_{sl}) of the deposited layer (grey) increases at the beginning of the deposition the most (B).

3.1.2 Screen printing

In order to achieve a homogeneous paste that is suitable for the screen printing process, the tin dioxide powders synthesised via the FSP method were mixed with polyethylene glycol (PEG 600, Fluka) in a mortar. The pastes contained 80 wt% of the desired SnO_2

material. The thus prepared pastes were subjected to a standard screen printing treatment using a screen printer Ekra Microtronic II (see Figure 13).
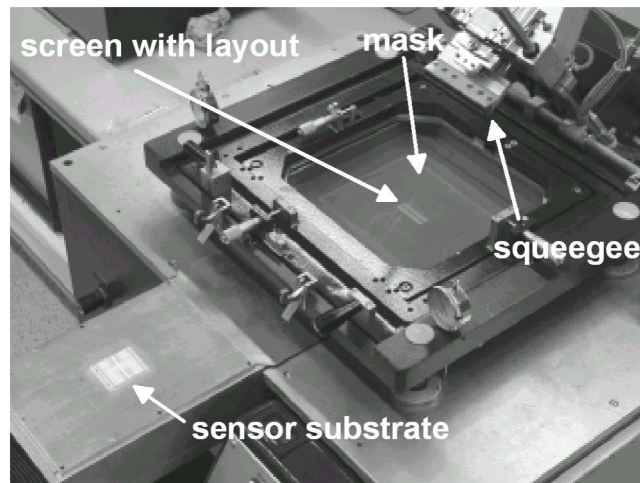

Figure 13: Picture of the screen printing setup. For the deposition of the SnO_2 pastes a standard screen printer (Ekra Microtronic II) with appropriate screen layouts was used.

The SnO_2 containing paste was put on the screen printing mask with an appropriate screen layout, i.e. it had openings just where the underlying electrode structures of the substrates should be covered with the sensing material. A rubber squeegee pressed the paste through the openings of the mask and after the removal of the screen the coated substrates were taken out for drying and calcination (see Figure 14).
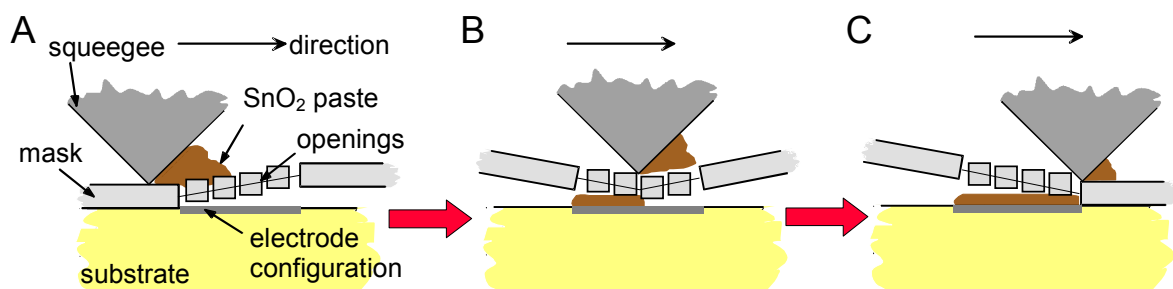

Figure 14: Principle of the screen printing process. A substrate is fixed below a mask with openings exactly where finally the sensing area shall be located (A). A rubber squeegee presses the paste through the openings of the mask (B). After the removal of the mask a deposited layer stays on the substrate (C).

3.1.3 Spin coating

Spin coating requires an aqueous solution of the metal oxide. However, just metal oxide in water leads to a fast segregation of the solid at the bottom of the solvent. Therefore, additives that are able to stabilize the oxide particles in the solution have to be introduced. In the present study, β-alanine (Fluka) was used as a stabiliser. A 1M β-alanine solution was prepared containing 45 wt% SnO_2. By means of a micropipette (eppendorf multipette plus) 1μl of the stabilised solution was dropped onto an alumina substrate that was fixed on a spin coater Convac 1001. The spinning was performed with 4000 rounds per minute (rpm) for 60 s (see Figure 15).
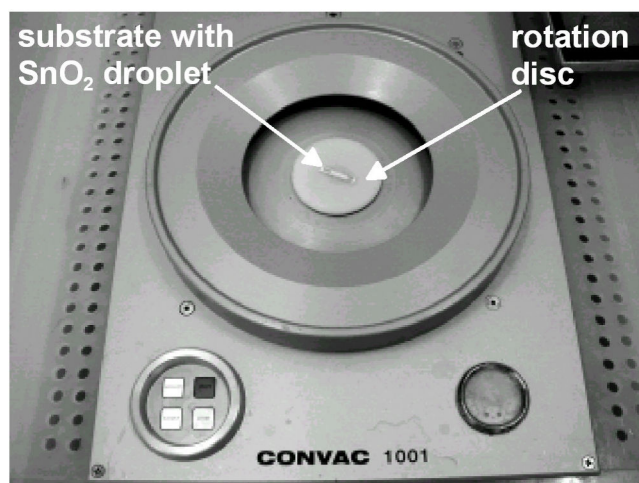
Figure 15:   Picture of the spin coating setup. For the deposition of the SnO_2 solution on the sensor substrate a standard spin coater (Convac 1001) was used.

After drop coating a droplet of the SnO_2 containing suspension onto the alumina substrate, the droplet wets the substrate depending on the adhesion properties of the latter. Therefore, by spinning the substrate on a rotation disc the solution spreads homogeneously over the substrate. The resulting deposited film is thinner and of equal height throughout the deposited area (see Figure 16).

Figure 16: Principle of the spin coating process. A droplet of a stable aqueous suspension of the metal oxide is deposited onto a substrate (A). The droplet wets the surface of the substrate to a certain extend (B). By spinning the rotation disc the droplet starts to spread over the surface of the substrate (C).

3.2 Sensor characterisation

The sensing material used in this work has been extensively studied using different techniques. The particle sizes were in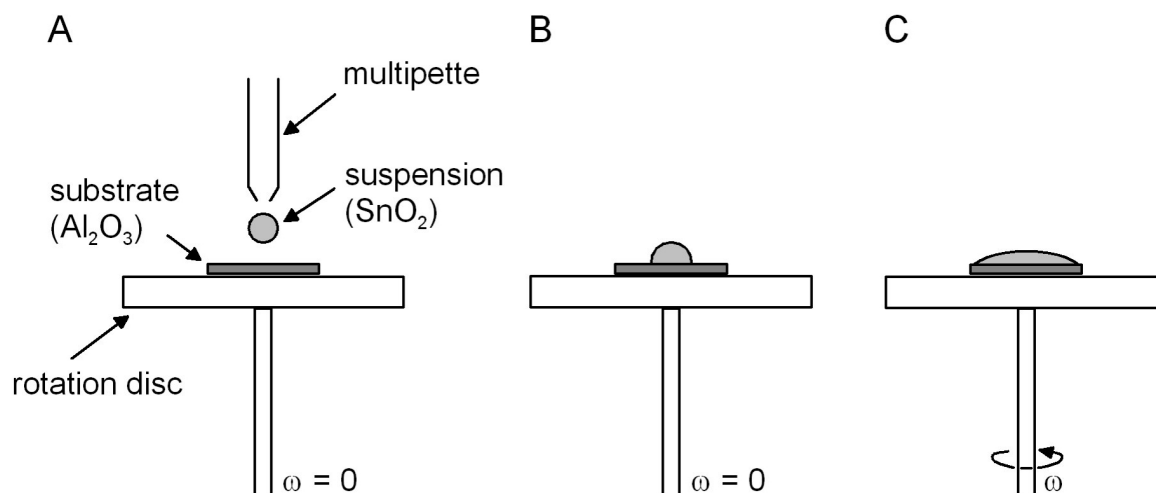vestigated by Brunauer, Emmett and Teller (BET) surface area determination and compared with the results of the X-ray diffraction patterns (XRD). The latter and high resolution transmission electron microscopy (HRTEM) delivered information about the crystallinity of the synthesised metal oxides. Scanning electron microscopy (SEM) and scanning transition electron microscopy (STEM) images allowed for the analysis of the morphology of the material. Furthermore, X-ray photoelectron spectroscopy (XPS) and extended X-ray absorption fine structure (EXAFS) were applied to get insight into the state and composition of the undoped and doped SnO_2.

Most of the above mentioned techniques were applied within the framework of different collaborations with international laboratories being experts in the respective fields and published in common papers. Therefore, details of the used setup can be found in the references that will be given in the respective sections of this work. Those measurements

that were performed completely at the Institute of Physical and Theoretical Chemistry at the University of Tübingen will be described in the following sections.

3.2.1 Scanning electron microscopy (SEM)

SEM was used to characterise the morphology and the thickness of the deposited layers. The samples could be measured unsputtered, charging of the samples was only minor. For the measurements, a Zeiss SEM (DSM 962) with a tungsten electrode was used. The surface of the layers was investigated using accelerating voltages of 3 kV and 10 kV and magnifications between 100 and 30,000. For the cross section analysis to determine the layer thickness the samples were mounted vertically and an accelerating voltage of 5 kV and a magnification of 500 was used.

3.3 Sensor performance

To determine the performance of a gas sensor, i.e. how it behaves towards the presence of gases, different parameters are usually investigated. In the following the most common definitions of the different detection properties are given and the experimental setup to determine them is described.

3.3.1 Dc electrical measurements

The standard parameter of a metal oxide gas sensor that is read out as its signal is the overall conductance G or resistance R. As already described in chapter 2.2 and Equation (1) those adsorption processes causing a band banding of the metal oxide influence the resistance of the latter. Therefore, the sensor signal S is usually given as the resistance ratio R_{air}/R_{gas} for reducing gases and R_{gas}/R_{air} for oxidising gases, where R_{gas} is the resistance of the sensor in the presence and R_{air} the resistance in the absence of the analyte, respectively (see Equation 10).

$$S_{red} = \frac{R_{air}}{R_{gas}} \quad \text{and} \quad S_{ox} = \frac{R_{gas}}{R_{air}} \tag{10}$$

Other parameters of interest to describe a sensor's properties are the sensitivity m, the analytical sensitivity α, the lower detection limit LDL, the reproducibility Q, and the response time T_{res}.

The response time T_{res} gives a measure of how fast a sensor will react to a certain analyte and is defined as the time $t_{90\%}$, i.e. the time it takes for the sensor to reach the 90% of the maximum signal change after a certain analyte was started to be delivered. The reproducibility Q shows the similarity of individual sensors of one type [7, 24]. To compare the reproducibility for individual sensors from one batch, the mean value relative to the maximum value of a sensor property (e.g. sensor resistance R or the sensor signal S) is evaluated (Equation 11). Theoretically, the reproducibility ranges from 0 (completely irreproducible sensor) to 100 (perfectly reproducible sensor).

$$Q = \left(\frac{\frac{1}{n}\sum_{k=1}^{n} S_k}{S_{max}} \right) \cdot 100 \tag{11}$$

The lower detection limit LDL gives a measure for the minimum gas concentration that can be detected by the sensor. It's related to that analyte concentration that is just outside a resistance interval of three times the standard deviation of the resistance in air R_{air}. The sensitivity m of a sensor is the change of the resistance R due to a change of the gas concentration and thus the derivative of the resistance function (Equation 12):

$$m = \frac{\partial R}{\partial c} \tag{12}$$

As all measurements are not with absolute precision but rather with a certain inaccuracy, the analytical sensitivity α is introduced which weights the sensitivity m with the standard deviation of the measured value, i.e. the resistance R (Equation 13):

$$\alpha = \frac{m}{\sigma_R} \qquad\qquad (13)$$

The resistance of the total sensing device was measured using a digital multimeter (Keithley DMM 199 or DMM 2000). In the case of high resistance, an electrometer was used (Keithley EM 617). The sensors were heated to their operating temperatures (200°C – 450°C) by applying a constant voltage to the platinum heater at the back side of the sensors. Therefore, a calibration curve of measured temperature versus applied voltage was taken by using an infrared pyrometer (Maurer KTR 2300).

A computer driven gas mixing system provided the analyte gas. A typical gas mixing bench consisted of computer controlled mass flow controllers and computer controlled valves. The desired analyte concentrations were delivered by mixing certified analyte gas with the appropriate amount of dry or humidified synthetic air. The humidity was adjusted by bubbling synthetic air through a column of water and subsequently mixing it with dry synthetic air. The final gas mixture was delivered through a home-made Teflon chamber containing up to four sensors.

3.3.2 Catalytic conversion measurements

Catalytic conversion of the analyte gases was measured using more than one identical sensor placed in a chamber (Figure 17). In the case of screen printed sensors eight identical sensors were used, one in a single sensor chamber followed by a chamber with the other seven sensors. In the case of directly deposited sensors four identical sensors were placed in one chamber. Downstream of the measurement chamber, an IR gas analyzer (Innova 1301) was employed to analyze the composition of the outgoing gas. On the basis of the measured CO_2 concentrations and the CH_4, CO and ethanol concentrations in the downstream gas, the percentage of the conversion was calculated. In order to get information about the influence of the entire setup (measurement chamber, blank substrates, gas connections etc.) measurements under identical conditions were performed using substrates without a sensing layer.
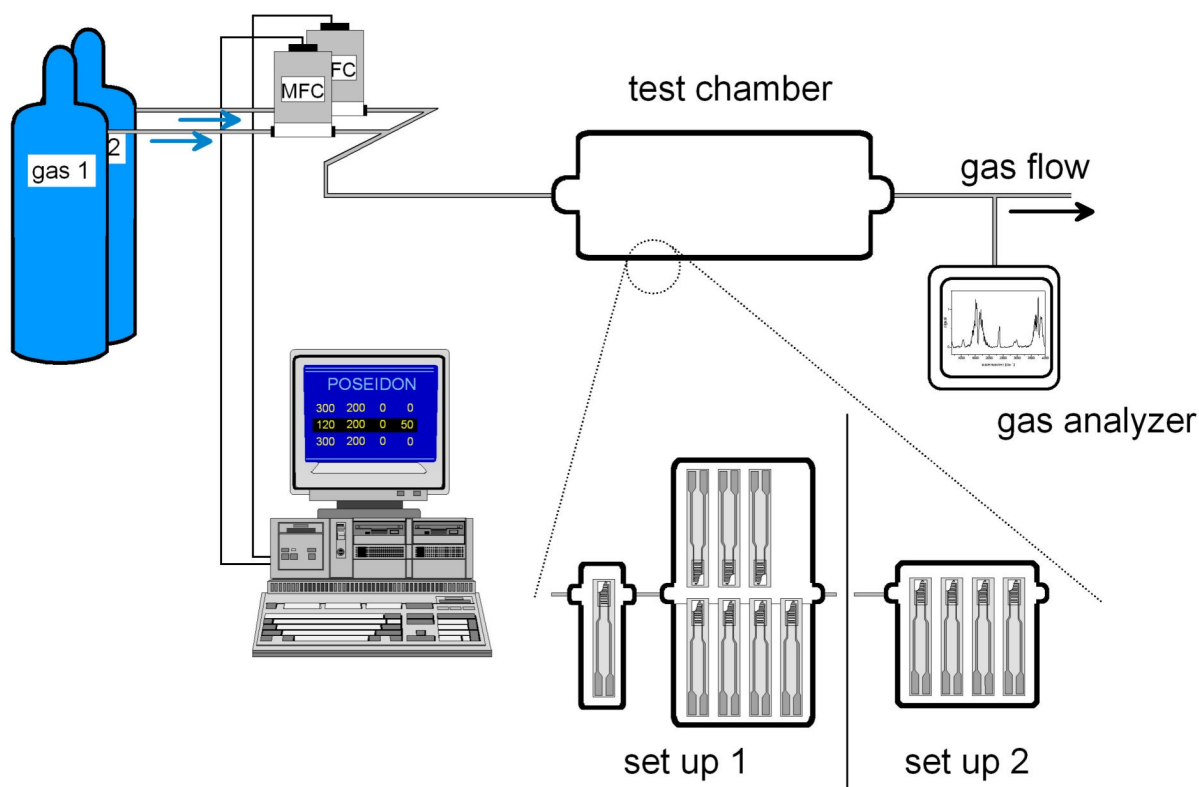
Figure 17: Catalytic conversion measurements. The computer controlled gas mixture is delivered through the test chamber which contains either eight screen printed sensors (setup 1) or four directly deposited sensors (setup 2). A downstream IR gas analyzer detects the composition of the outgoing gas stream.

3.3.3 Stability tests

For stability tests, screen printed SnO_2 and 0.2 wt% Pt doped SnO_2 sensors were investigated. A set of four sensors (two sensors with undoped SnO_2 and two sensors with 0.2 wt% Pt doped SnO_2) has been exposed to a test cycle of different CO concentrations repeated every second day for a period of 20 days. The sensing properties over this period were assessed through the sensor signal.

3.3.4 Simultaneous work function and resistance measurements

As mentioned above in chapter 2.2, dc electrical measurements can only investigate those surface species which contribute to an overall charge transfer with the conduction band, whereas work function changes can additionally be due to adsorbed species without charge transfer, but under building of dipoles with the surface. Therefore, the

combination of work function change and resistance measurement technique provides insight into those surface species that build up local dipoles. For a better comparability, these measurements should be performed simultaneously to ensure the same measurement conditions.
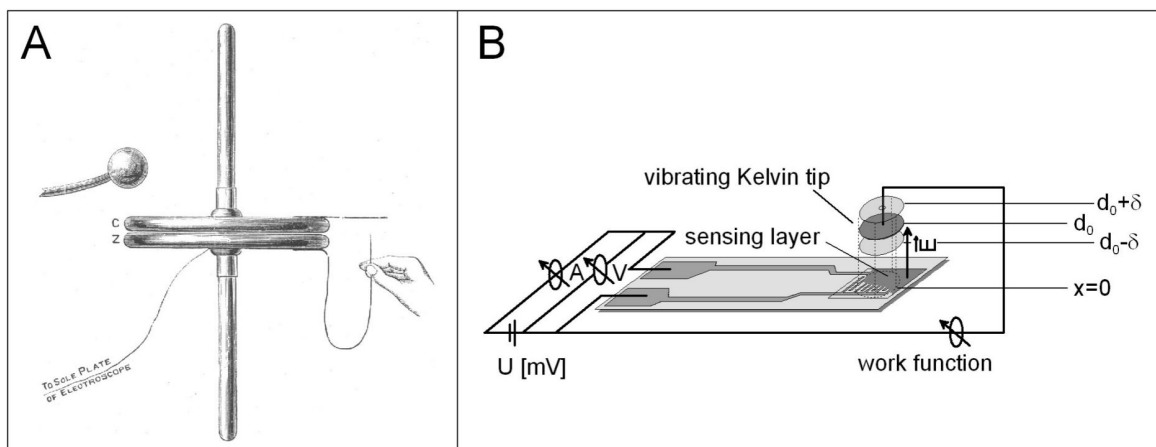

Figure 18: Principle of the Kelvin oscillator method. The original experiment was performed using a copper and a zinc plate varnished with shellac as a capacitor and a gold leaf electroscope (A). The actual setup consists of a vibrating metal reference tip ("Kelvin tip") and a real sensor with a semiconducting sensing layer as sample. The oscillating tip induces a current that can be measured (B).

Simultaneous work function and resistance (under constant voltage polarisation) measurements were performed in a Kelvin probe (Mc Allister KP6500) setup. The technique used here for measuring differences in work functions is the well established Kelvin oscillator method (see Figure 18) [149, 150]. The basic principle of this method was first described by Lord Kelvin when he gave a lecture at the Royal Institution in London on the 21st of May 1897. He showed that by bringing two parallel plates of different metals in electrical contact they get charged and concluded "that in the separation of the two discs of copper and zinc the copper carries away resinous electricity and the zinc vitreous electricity" [151]. In the chosen setup, the Kelvin oscillator consists of a metallic reference electrode in electrical contact with the sensor. The reference electrode oscillates at a mean distance d_0 over the sample. In electrical equilibrium conditions, a contact potential difference V_{CPD}, which is equal to the difference in work function of the two materials $\Delta\Phi$, appears. This results in an electrical field between the two plates of the capacitor, the sample and the grid. Changes in distance due to the

oscillation result in changes of the capacity C and therefore in a current i(t), as described by Equation 14 and 15.

$$C(t) = \varepsilon\varepsilon_0 A/(d_0 + \delta\sin\omega t) = Q(t)/V_{CPD} \tag{14}$$

$$i(t) = \dot{Q} = -V_{CPD}\varepsilon\varepsilon_0 A\delta\omega\cos\omega t/(d_0^{\ 2}(1+\delta/d_0)\sin\omega t)^2 \tag{15}$$
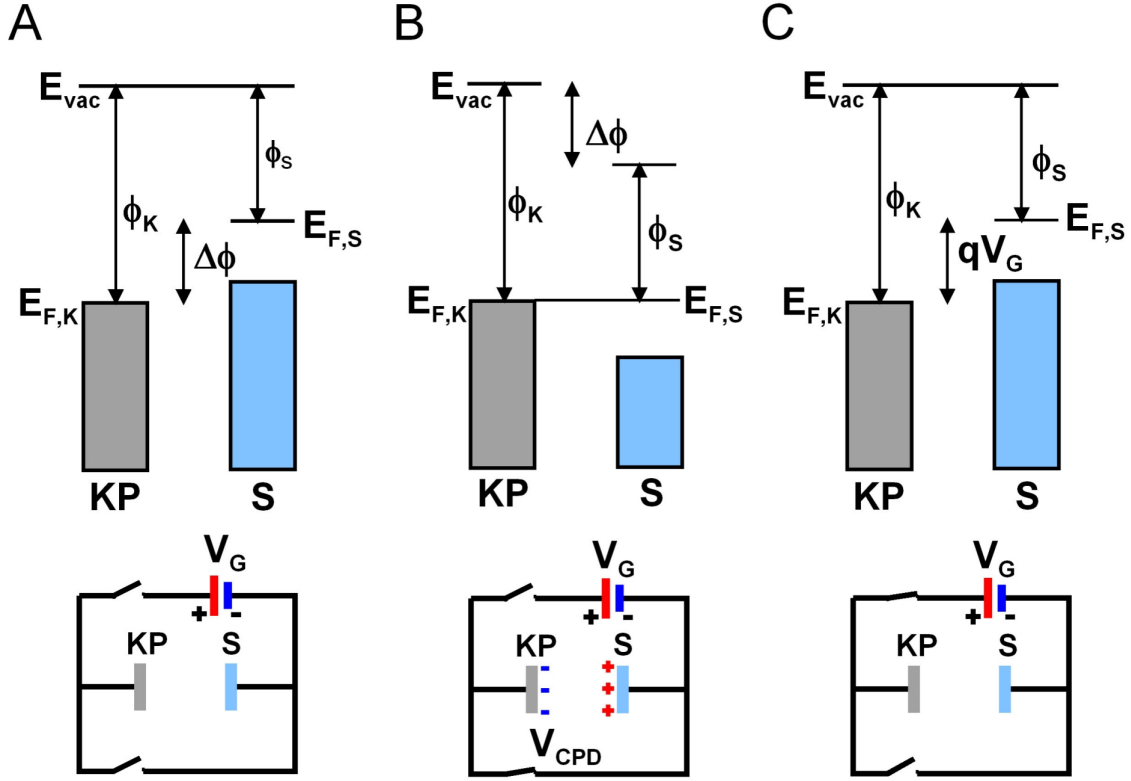
Figure 19: Circuit of the Kelvin probe setup. The metal tip of the Kelvin probe and the semiconductor sample have different work functions (A). Bringing them into electrical contact leads to a charging of the two opposing materials and the appearance of a contact potential difference V_{CPD} (B). The vibration of the Kelvin tip causes a current flow i(t). Applying a counter voltage V_G diminishes the current and amortises the contact potential difference (C).

Experimentally, a counter voltage V_G is applied and adjusted until i(t) disappears. In this case the counter voltage is equal to the contact potential difference and thus the difference in work function $V_{CPD} = -V_G = \Delta\Phi/q$ is measured (see Figure 19). Consequently, if the work function of the metallic reference electrode is unaffected by changes in the ambient atmosphere (i.e. $\Phi_{Metal,i} = \Phi_{Metal,j}$) it is possible to determine work

function changes of a semiconductor as a result of changes in the contact potential difference in dependence on gas adsorption (Equation 16).

$$\Delta V_{CPD} = V_{CPD,f} - V_{CPD,i} = \frac{\Phi_{Mtetal,f} - \Phi_{SC,f}}{q} - \frac{\Phi_{Mtetal,i} - \Phi_{SC,i}}{q} = \frac{\Phi_{SC,i} - \Phi_{SC,f}}{q} = -\frac{\Delta\Phi}{q} \qquad (16)$$

where q is the elementary charge and *i* and *f* indicate the situation before and after gas adsorption, respectively. At the same time, a constant voltage is applied to the interdigited electrodes of the sensor and the current is measured. Therefore, changes in the current lead to changes in the resistance by Ohm's law (Equation 17).

$$\Delta R = \frac{U}{\Delta I} \qquad (17)$$

All investigated sensing layers consisted of polycrystalline grains. Thus, changes in the overall resistance of the sensor can be attributed to changes in the band bending of the semiconductor (see Equation 1 in chapter 2.2). Basically, the work function Φ of a semiconductor contains three contributions: (i) the energy difference between the Fermi level and conduction band in the bulk (E_C-E_F)$_b$, (ii) the band bending qV_S , and (iii) the electron affinity χ (Equation 18; see also Figure 5 in chapter 2.2).

$$\Phi = \left(E_C - E_F\right)_b + qV_S + \chi \qquad (18)$$

All three contributions may, in principle, change upon gas exposure. If one assumes that the difference between Fermi level and conduction band in the bulk is unaffected by adsorption processes at the surface, changes in work function are due to changes in band bending or changes in electron affinity. Therefore, experimental determination of changes in band bending by resistance measurements and of the changes in work function by the Kelvin oscillator method allows a calculation of changes in electron affinity (Equation 19).

$$\Delta\chi = \Delta\Phi - kT\ln\frac{G_I}{G_F} = \Delta\Phi - kT\ln\frac{R_F}{R_I} \qquad (19)$$

Experimentally, the simultaneous work function and resistance measurements ("Kelvin measurements") were performed with CO, humidity, and oxygen as analytes on undoped SnO_2 sensors. In the case of CO and humidity a standard gas mixing system could be used to deliver the desired concentrations through the home-made Kelvin probe chamber. This modified Kelvin probe setup allowed measurements under real sensor working conditions, i.e. the sensor was heated between 200°C and 400°C and provided with a continuous gas flow of 200 ml/min. Additionally, the influence of low oxygen concentration on the SnO_2 surface was investigated. For these measurements the system to deliver the appropriate gas mixture had to be changed. Certified nitrogen was additionally purified by flowing through a filter (AirLiquide Oxisorb) that adsorbed residual oxygen and water. Thus purified, the nitrogen was led through a solid electrolyte (Zirox Electrolysis Cell) permeable for oxygen, i.e. an oxygen ion conductor. This solid electrolyte is made of zirconia in the shape of a hollow pipe with the nitrogen flowing through and surrounding air.
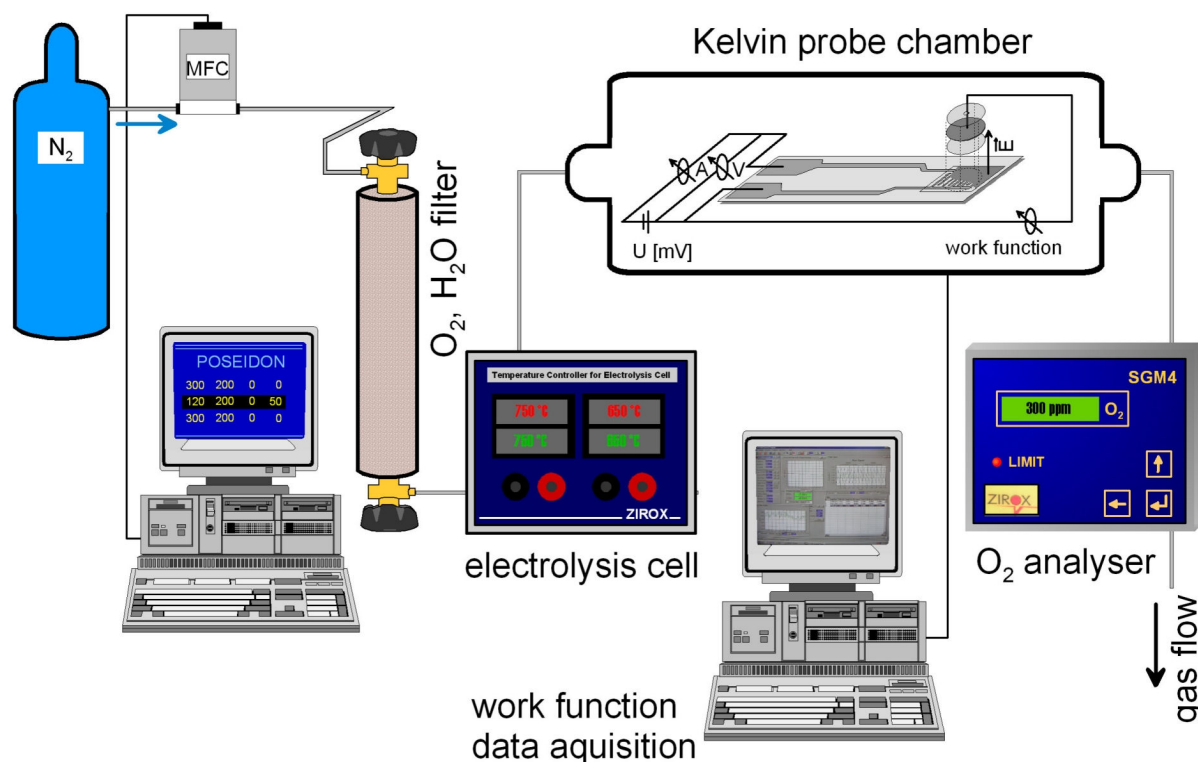
Figure 20: Setup for the Kelvin measurements at low oxygen concentration. N_2 is purified by an O_2 and H_2O adsorbing filter. Afterwards, O_2 is dosed to the systems by means of an electrolysis cell. The modified Kelvin probe measures changes in work function and resistance simultaneously.

Due to different oxygen partial pressures in the inner and the outer gas atmosphere a potential appears according to the Nernst equation. By regulating the current of this electrolysis cell, one can enforce the direction and amount of the oxygen ion conduction through the ceramic. Thus, different oxygen concentrations were added to the gas flow. This gas mixture was led through the measurement chamber. Subsequently after the chamber, the oxygen concentration was controlled by an oxygen analyzer (Zirox SGM4) at the end of the line. The oxygen analyzer is again a zirconia tube and based exactly on the same principle as before. This time, the appearing potential is used to measure the oxygen partial pressure and thus the oxygen concentration of the gas stream. Figure 20 shows a sketch of the setup.

4

—— **Material characterisation** ——

Besides testing the gas sensing properties of the realised gas sensors it is of major interest to study the physical and chemical properties of the synthesised base material and of the fabricated layers. This is necessary to understand and model the sensing reactions that are taking place at the metal oxide / gas interface and to be technologically able to tune the sensor performance by adjusting the fabrication parameters.

Therefore, Chapter 4.1 lists all the important results about the SnO_2 powder that was prepared for the classical deposition methods. These results give detailed information about the sensing material itself and were gained by BET, XRD, HRTEM, XPS, EXAFS, STEM, and EDX measurements. Once it was known how the parameters of the FSP reactor influence the base material, also the directly deposited layers were investigated. The results are reported in Chapter 4.2.

4.1 Powder characterisation

The FSP process is a very useful method to control the grain size of the synthesised metal oxides. The grain size of the final material depends mainly on the ratio between the feed rate of the syringe pump and the flow of oxygen. Three different combinations have been used to synthesise undoped and Pt-doped SnO_2 powder, i.e. a feed rate of 3 ml/min and an oxygen flow of 7 l/min (called "3/7"), a feed rate of 5 ml/min and an oxygen flow of 5 l/min (called "5/5") or a feed rate of 8 ml/min and an oxygen flow of 3 l/min (called "8/3").

4.1.1 Undoped SnO_2

The grain size of the collected powders was determined using the Brunauer, Emmet and Teller (BET) surface area determination. The powder specific surface area (SSA) was measured by nitrogen adsorption at 77 K after degassing the sample. Assuming spherical particles, the average primary particle diameter d_{BET} can be calculated according to $d_{BET} = 6/(SSA \cdot \rho_P)$, where ρ_P is the density of SnO_2 (6.85 g/cm^3). The observed grain

sizes varied between 5.5 nm (7/3), 9.9 nm (5/5), 17.1 nm (8/3; ethanol as solvent) and 19.4 nm (8/3; toluene as solvent) (see Table 5) [146, 148].

Table 5: Properties of differently prepared SnO_2 powders. The primary particle size was determined from BET measurements and the primary crystallite size from XRD patterns.

product	flame conditions	precursor solvent	SSA size d_{BET} [nm]	crystallite size d_{XRD} [nm]
SnO_2	8/3	ethanol	17.1	17.8
SnO_2	3/7	toluene	5.5	5.6
SnO_2	5/5	toluene	9.9	10.7
SnO_2	8/3	toluene	19.4	19.8

X-ray diffraction patterns (XRD) were recorded in order to obtain the average crystallite size of the SnO_2 [146, 148]. This was done by using the fundamental parameter approach and the Rietveld method [152] with the structural parameters of cassiterite (ICSD Coll. Code: 084576 [153]). In all cases the measured crystallite sizes listed in Table 5 showed a very high congruence with the BET primary particle size. This is a strong indication that the primary particles are single crystals with a low degree of aggregation and has been reported also for other metal oxides synthesised by FSP [21]. Figure 21 shows the corresponding XRD pattern. Generally, increasing the ratio of precursor liquid to oxygen flow rate increased the grain size of the SnO_2 particles and therefore narrowed the peak width. No other crystalline species than SnO_2 could be detected.
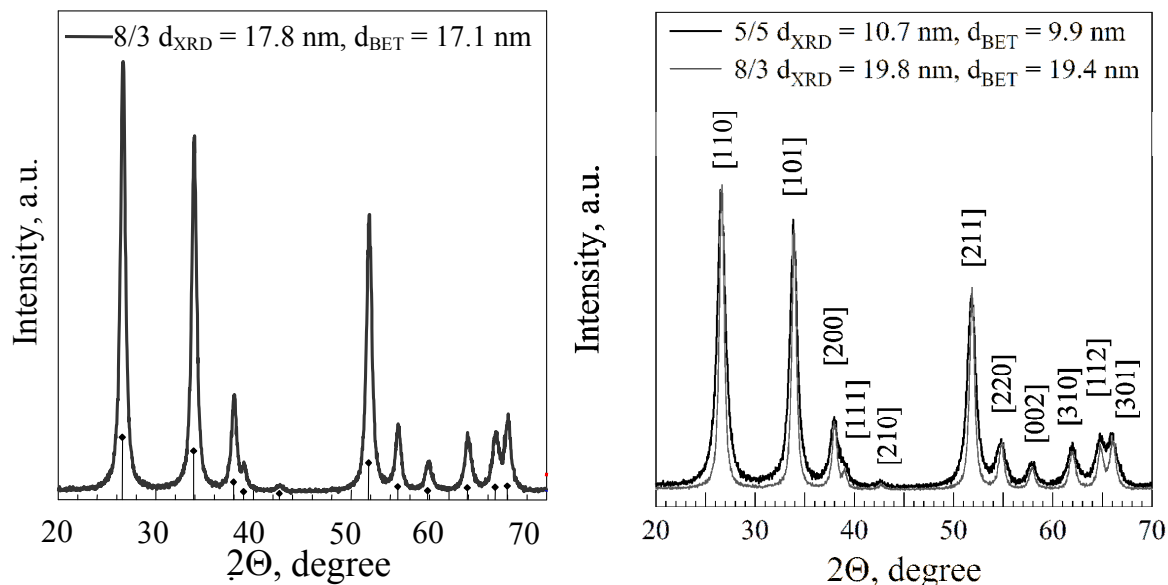
Figure 21: X-ray diffraction pattern of as-prepared SnO₂ powders made at different flame conditions. Using ethanol as precursor solvent led to a primary particle size of 17.8 nm for the 8/3 flame (left), whereas in the case of toluene the primary particle size was 19.8 nm (right). Other flame conditions (5/5) realised smaller particles (9.9 nm) [146, 148].

To confirm the high crystallinity and the presence of crystalline primary particles high resolution transmission electron microscopy (HRTEM) and corresponding electron diffraction was carried out with the SnO₂ 5/5 powder [148]. The qualitative approximation of the particle size in Figure 22 is in good agreement with the reported data for d_{BET} and d_{XRD}.

Figure 22: High resolution TEM (left) and the corresponding electron diffraction pattern (right) of undoped SnO₂ (5/5). The powder shows high crystallinity and the particle size corresponds to the results of BET and XRD [148].

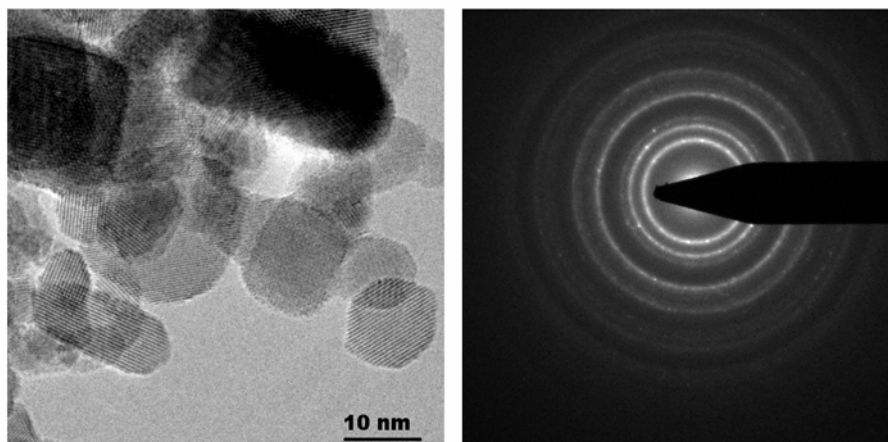The morphology of the nanoparticles was further qualitatively characterised by transmission electron microscopy (TEM) [146]. Figure 23 shows the TEM images of the SnO_2 8/3 powder at two different magnifications. The observed morphology is typical for particles formed in the gas phase [130]. The powder consists of polyhedral primary particles with an estimated particle size of about 20 nm.
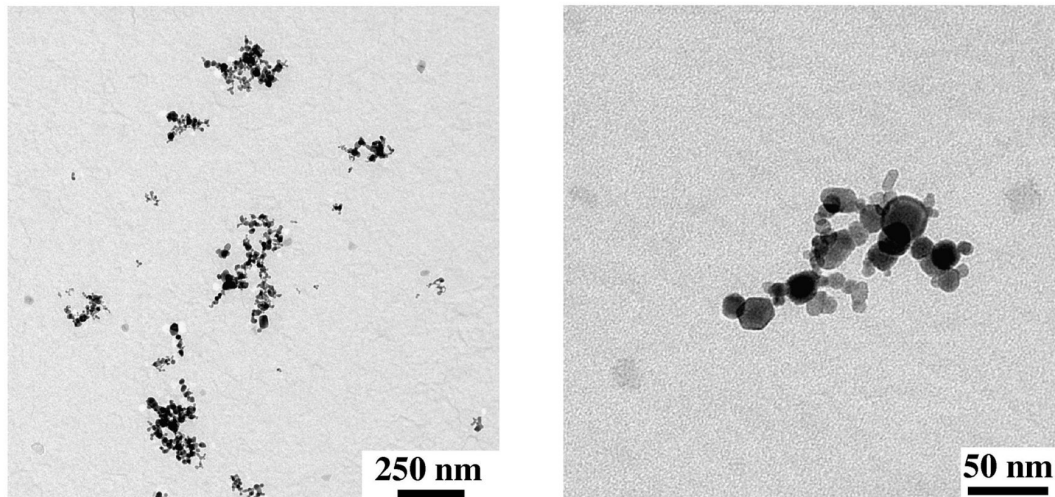
Figure 23:   TEM images of the SnO_2 8/3 powder. The particles show low degree of aggregation [146].

The thus prepared powders were used to fabricate sensors by screen printing. However, preparing a highly viscous and homogeneous paste for the screen printing is a difficult task when coming to very small particles in the nanometre range. The particles tend to coagulate and aggregate. The deposited layers were investigated by scanning electron microscopy (SEM). This tendency of agglomeration can be clearly seen in Figure 24. Whereas the structure of the primary particles remains unaffected by the screen printing procedure, larger agglomerates appear. In the case of smaller particles the amount and size of those agglomerates is larger than for the larger particles. At the same time the stress within the deposited layer is larger for smaller grain size so that during the calcination step the layer tears apart and deep cracks appear.
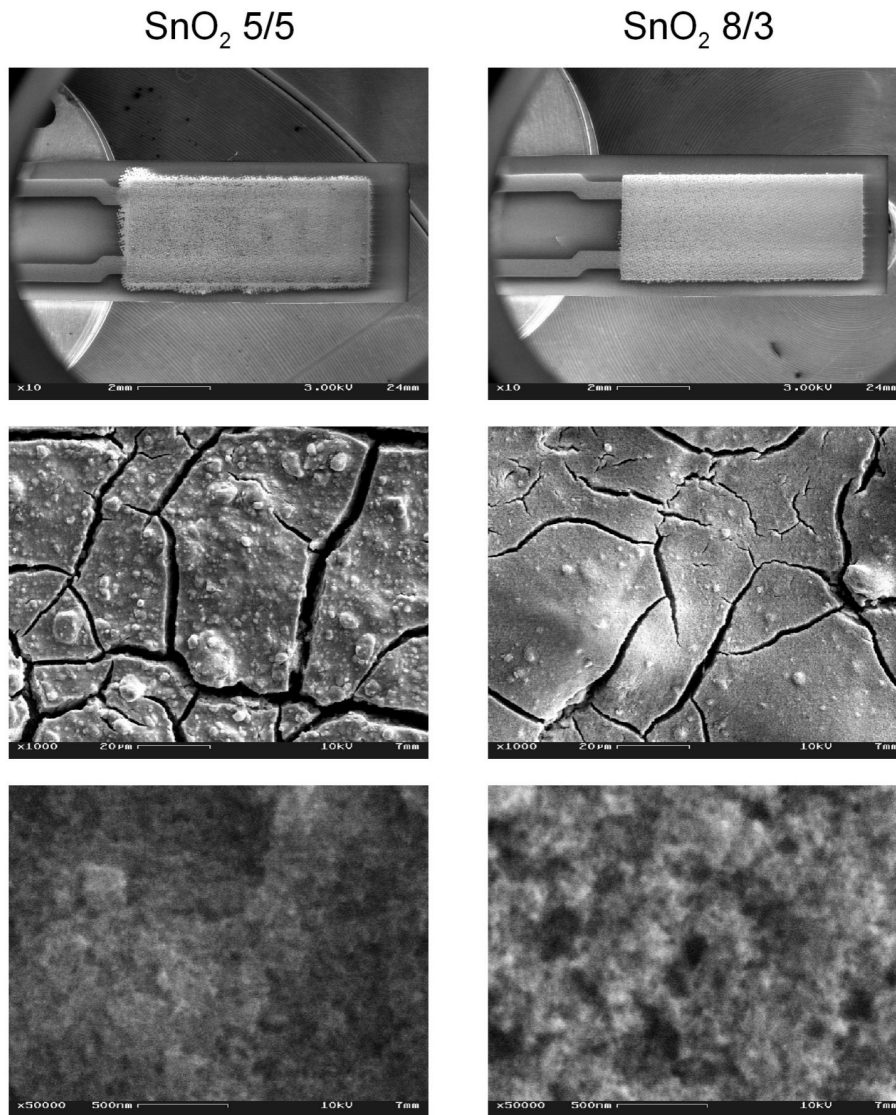
SnO$_2$ 5/5   SnO$_2$ 8/3

Figure 24: SEM images of the screen printed sensors with SnO$_2$ 5/5 (left) and SnO$_2$ 8/3 (right) taken at an acceleration voltage of 10 kV. The smaller particles tend to build larger agglomerates and more cracks in the layer than the larger particles (middle row). However, both layers are very porous (lower row).

4.1.2 Pt-doped SnO$_2$

In situ functionalisation of the SnO$_2$ particles during the FSP synthesis route was also applied to explore the potential of this method for sensor fabrication and to optimise sensor performance. The method of *in situ* functionalisation of metal oxides with platinum within a flame process is rather new and was first described for the doping of TiO$_2$ [154]. Fabricating a Pt-doped Al$_2$O$_3$ catalyst via FSP, it has been shown that the platinum is present as highly dispersed clusters and that the mass loading in the final

product was the same as in the precursor solution [23]. For the present work, 0.0 wt%, 0.2 wt%, and 2.0 wt% Pt-doped SnO_2 with a 5/5 flame were synthesised. All three powders showed a grain size of about 10 nm revealed by BET and XRD [148]. Figure 25 shows the XRD patterns of the different powders. It can be clearly seen that the platinum functionalisation did not influence the highly crystalline cassiterite structure and the SnO_2 crystallite size.
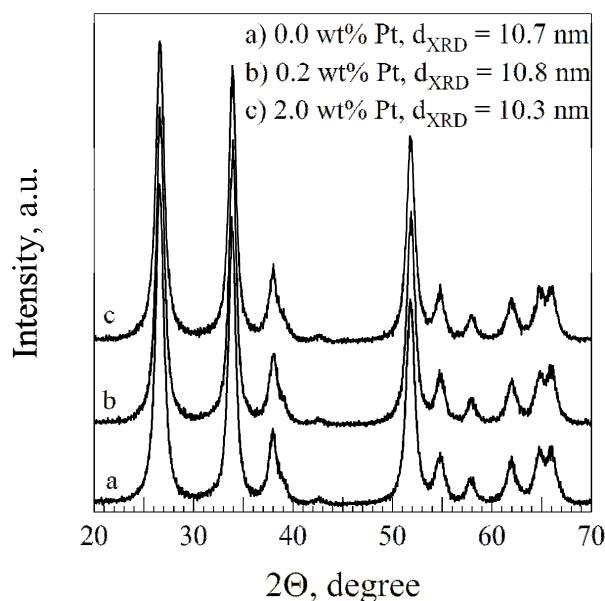
Figure 25: X-ray diffraction patterns of the SnO_2 powder with different platinum loadings. Adding platinum did not influence the highly crystalline cassiterite structure and the SnO_2 crystallite size. The Pt-loadings were too low (0.2 wt% and 2.0 wt%) to be detected by XRD [148].

To check the presence of the platinum in the SnO_2 powders scanning transmission electron microscopy (STEM) investigation and corresponding energy dispersive X-ray (EDX) analysis were carried out for the 2.0 wt% Pt doping [148]. The STEM image in Z-contrast of SnO_2 (Figure 26) shows that the inherent Z-contrast difference between tin and platinum is not very high. The result is a rather blurred image. However, one can state that no particle inhomogeneities are present. Furthermore, an EDX analysis of that section of the sample shows the presence of Pt.
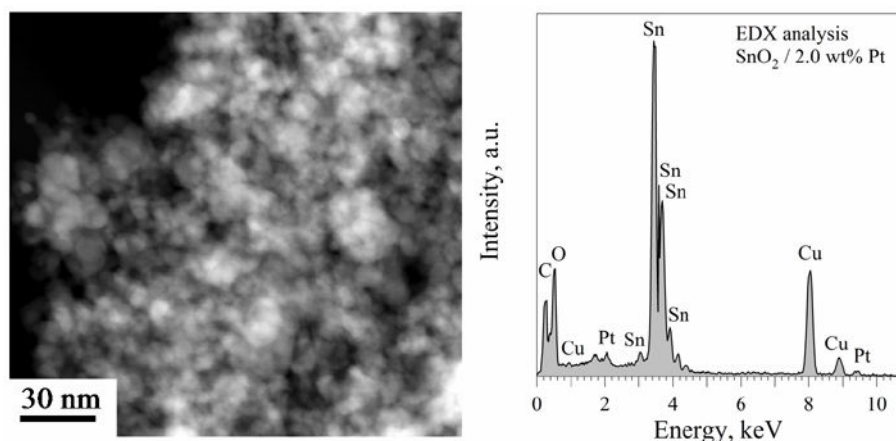
Figure 26:   STEM image in Z-contrast of 2.0 wt% Pt doped SnO_2 (left). The corresponding EDX analysis shows the presence of platinum, the signals for copper and carbon are due to the carbon coated copper TEM grid (right) [148].

As mentioned above (Figure 25), the platinum was invisible in the XRD spectra indicating that no crystalline platinum particles larger than 10 nm were present. Therefore, surface sensitive or element specific analysis methods are needed to get more information about the platinum. X-ray photoelectron spectroscopy (XPS) and extended X-ray absorption fine structure (EXAFS) analysis were performed [148]. XPS revealed that tin is in the 4+ oxidation state (Sn^{4+}) and that the platinum is better dispersed in the case of low platinum loading (0.2 wt% Pt). Just one dominant species was found for platinum which is higher in binding energy than Pt^0, they are rather closely related to Pt^{2+}. The fact that the observed binding energies are slightly lower than the reported ones can be attributed to the rough UHV conditions of the XPS experiments leading to a partial reduction of the Pt^{2+}. Interestingly, no hints for Pt^{4+} could be found as reported by others [155]. Measurements under normal conditions in air, i.e. X-ray absorption near edge structure (XANES) and extended X-ray absorption fine structure (EXAFS), confirmed that the platinum is in the oxidized Pt^{2+} state and highly dispersed in the SnO_2. Furthermore, no Pt aggregates were found.

4.2 Directly deposited layer characterisation

After establishing FSP generated nanoparticles for gas sensor fabrication by classical deposition methods, the possibilities of depositing the particles directly from the gas phase on sensor substrates have been explored. Realising this would be a huge step of progress as the limitations of screen printing were clearly seen in the SEM investigations in Chapter 4.1.1. Firstly, the possibility of tuning the layer thickness was tested by varying the deposition time. In a next step the deposition of more than one layer was established.

4.2.1 Different layer thicknesses

All the layers were fabricated using the 5/5 flame conditions. SnO_2 was deposited on standard alumina substrates with three different deposition times, i.e. 30 s, 180 s and 360 s, respectively. Additionally, powder was collected from the filter mounted above the substrate holder. Thus, the properties of the deposited material could be compared with the same material from the gas phase to see whether the deposition itself influences the SnO_2.

Table 6: Properties of directly deposited SnO_2 with different deposition times and of the corresponding powder collected from the filter. The layer thickness was evaluated from SEM images, the primary particle size from BET measurements and the primary crystallite size from XRD patterns. The layer porosity can be calculated from the layer thickness [147].

SnO_2 taken from	deposition time [s]	thickness s_{sl} [nm]	SSA size d_{BET} [nm]	crystallite size d_{XRD} [nm]	layer porosity φ
sensor	30	9 ± 1	—	—	—
sensor	180	30 ± 3	—	8.4 ± 2.0	0.981 ± 0.004
sensor	360	40 ± 4	—	11.2 ± 1.0	0.983 ± 0.004
filter	(360)	—	10.3 ± 0.5	10.5 ± 1.0	—

To determine the particle size BET surface area determination and XRD pattern analysis of the SnO_2 powder collected from the filter have been carried out. Additionally, XRD pattern analysis was performed on the deposited SnO_2 layers of the sensors [147]. The primary particle size determined by BET and the primary crystallite size from XRD were

in good agreement (Table 6). This is a clear sign of the presence of monocrystalline particles. Furthermore, the crystallite size did not change due to the deposition of the particles as revealed by the XRD pattern of the SnO_2 layers with a deposition time of 180 s and 360 s. The signals for the shortest deposition time (30 s) were too weak for a crystallite size evaluation. Figure 27 shows that SnO_2 powder and layer have overlapping XRD pattern except from the diffraction signals of the alumina substrate and the platinum electrodes.
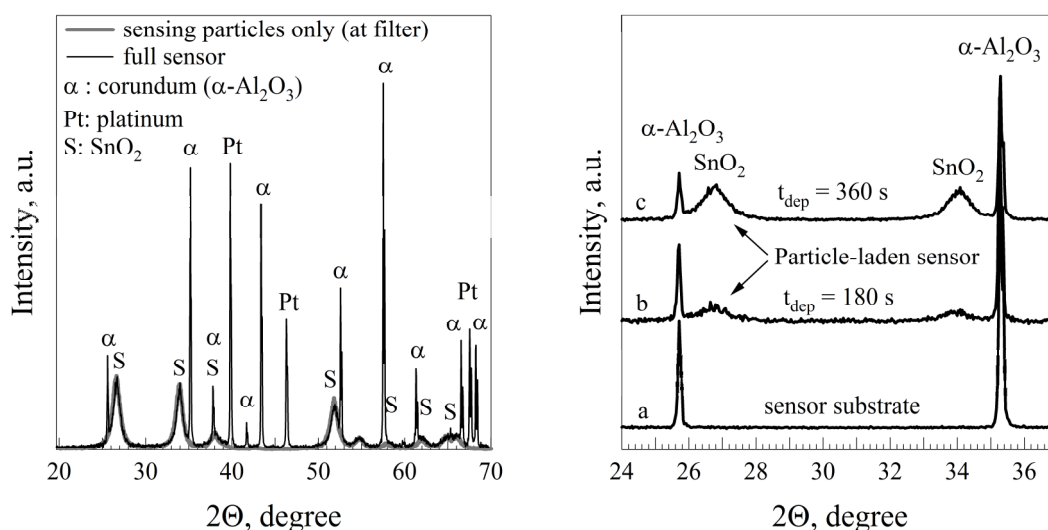
Figure 27: X-ray diffraction pattern of SnO_2 powder and sensors. No difference between the collected powder and the deposited layers could be observed (left). The pattern of the substrate shows diffraction signals of the α-Al$_2$O$_3$ (right, a). When a SnO_2 layer is deposited the signal of the latter increases whereas the signal of the substrate decreases with longer deposition times (right, b and c) [147].

SEM images of the cross sections of the sensors were used to estimate the sensing layer thickness on the alumina substrates (see Table 6). Figure 28 shows that the thus estimated layer thicknesses are in very good agreement with the model for the layer growth that was proposed in Chapter 3.1.1. It can be clearly seen that the layer grows fastest at the beginning of the deposition, whereas doubling of the deposition time (from 180 s to 360 s) increases the layer thickness only by a factor of 1.33. The porosity of the SnO_2 layers was estimated from the measured thickness of the porous layer (s_{sl}) and the corresponding layer thickness of a hypothetical dense SnO_2 solid layer (s_s) according to Equation 20.

$$\varphi = 1 - \frac{s_s}{s_{sl}} \qquad\qquad (20)$$

The solid layer thickness (s_s) can be gained from the attenuation of the XRD signal of the alumina substrate due to the covering with SnO_2 (for details, see [147]). It revealed that the directly deposited SnO_2 layers are highly porous having a porosity of about 98% (Table 6). This value fits very well to a simulation of the morphology of nanoparticle deposits that predicted a porosity of 97.7% for a layer of particles with 30 nm grain size [156]. Such a high porosity is strongly favoured for gas sensing applications as it results in a very large accessible surface for the analyte molecules to interact with the sensing material. Additionally, the porosity seems to be independent of the deposition time, i.e. the highly porous character of the layers is kept preserved also for the thickest layer.
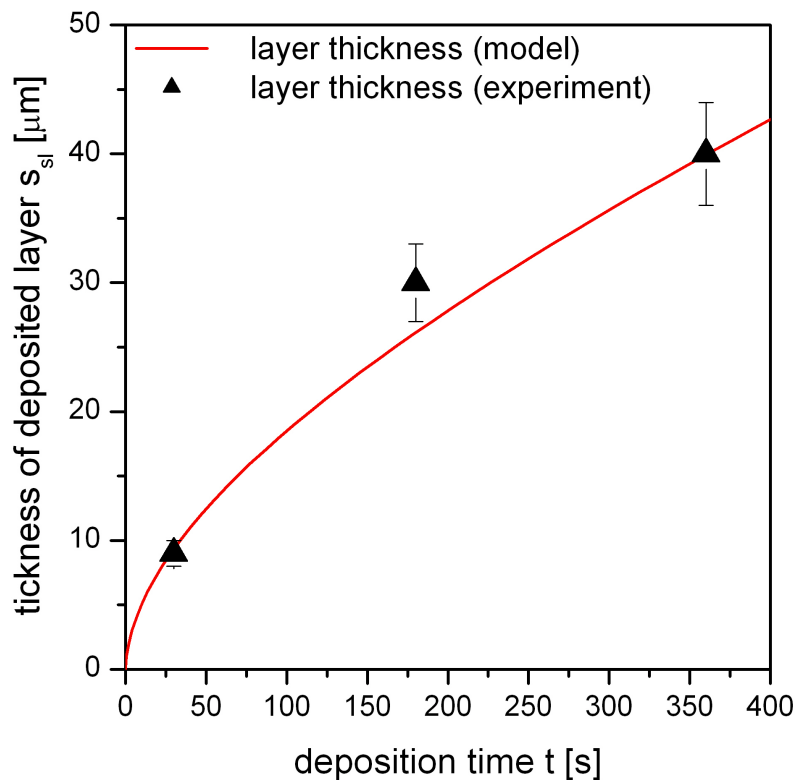

Figure 28: Dependency of layer thickness on the deposition time. The measured thicknesses (black triangles) that were extracted from SEM cross section images of the layers are in good agreement with the calculated layer thickness (grey line) [147].

4.2.2 Multi layer deposition

Once a sensor substrate is mounted above the flame of an FSP reactor, it is relatively easy to handle the deposition of different metal oxides subsequently after each other. After the desired thickness of the first layer is achieved, one simply has to exchange the precursor solution and thus the second layer will start to grow on top of the first one. In principle, each combination of material that can be synthesised by FSP can be applied for this multilayer fabrication. With regard to aspects that are relevant to applications, the combination of a gas sensitive functionalized metal oxide as bottom layer and a catalytic active metal oxide as top layer seems to be very promising. In this case, the top layer can act as a filter element of the sensor which is widely used to improve the performance of a gas sensor (see Chapter 2.6).

Table 7:   Overview of the fabricated single layer (A) and double layer (B) sensors. As sensing material undoped and Pd-doped SnO_2 was used and as filter material Pd-doped Al_2O_3.

A: single layer sensor	bottom layer
	SnO_2
	$0.1 \ wt\% \ Pd/SnO_2$
	$2.0 \ wt\% \ Pd/SnO_2$

B: double layer sensor	bottom layer	top layer
	SnO_2	$2.0 \ wt\% \ Pd/Al_2O_3$
	$2.0 \ wt\% \ Pd/SnO_2$	$2.0 \ wt\% \ Pd/Al_2O_3$

In order to investigate and extend this approach systematically, different kind of single layer and double layer sensors were fabricated (Table 7). The sensing layer was made out of undoped SnO_2 or palladium doped SnO_2 with different Pd loadings (0.1 wt% and 2.0 wt%). Additionally to these sensors, a second layer (i.e. a filter layer) was deposited on sensors with undoped SnO_2 and 2.0 wt% Pd-doped SnO_2 layers. This top layer was always 2.0 wt% Pd-doped Al_2O_3. For all material synthesis a 4/5 flame of the FSP reactor was used. From the experience gained so far this should result in an average particle size

of about 10 nm. The morphology and grain size of the nanoparticles was investigated by evaluating TEM images [144]. The size of the SnO_2 primary particles ranged from 4 to 10 nm and that of the Al_2O_3 ranged from 10 to 15 nm (Figure 29).
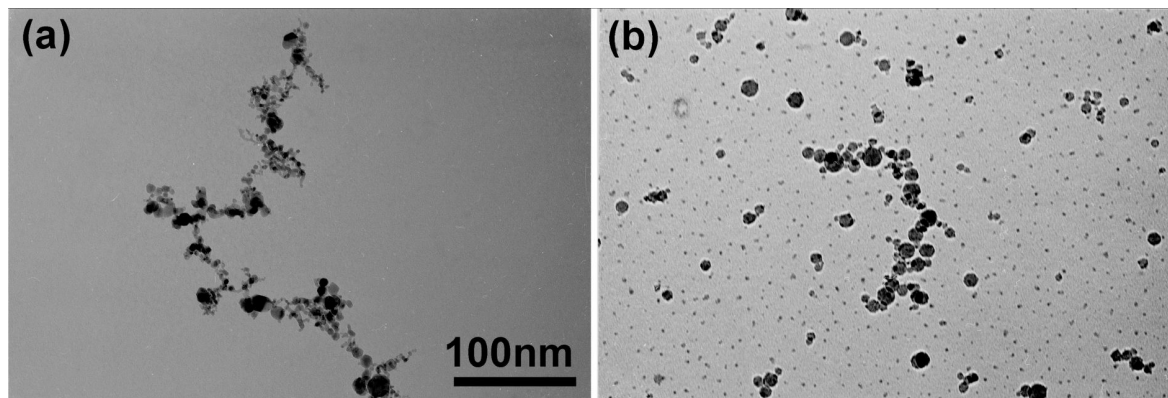
Figure 29: TEM images of SnO_2 (a) and Al_2O_3 (b) nanoparticles from FSP synthesis. The scale bar applies to both images [144].

One of the striking facts of the directly deposited layers is their high porosity while showing at the same time a high homogeneity and uniformity. This can be shown impressively by Figure 30. The layers are so porous that they are invisible for the human eye, i.e. they are transparent for the visible light. However, a SEM image of the same area clearly shows that the whole electrode structure is covered by the sensing layer. A zoom on the surface of the layer (magnification of 100 at an accelerating voltage of 5 kV) demonstrates the smoothness and uniformity of the macroscopic surface.
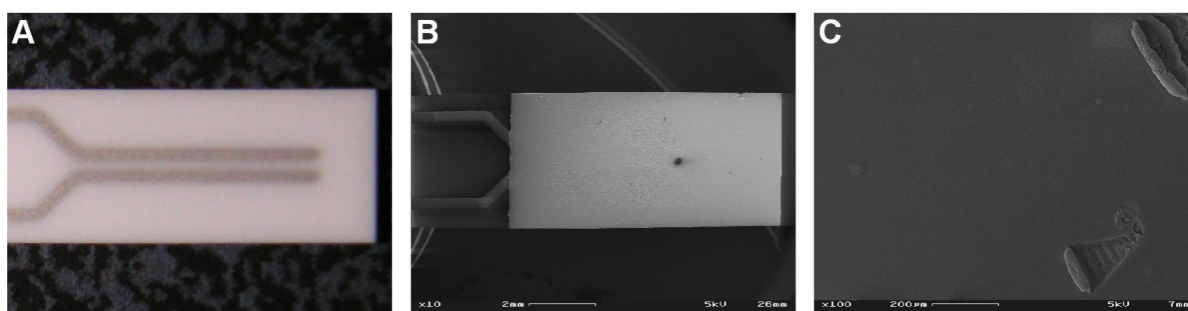
Figure 30: Top view of the directly deposited layers. The image taken with a digital camera shows that the SnO_2 layer is transparent in VIS (A). SEM image of the same area shows that the SnO_2 layer completely covers the front part of the substrate (B). The image with a magnification of 100 (accelerating voltage of 5 kV) confirms the smoothness of the layer. The scratches appeared due to mechanical damage while mounting the sample into the SEM setup (C).

Especially when comparing the quality of the directly deposited layers (Figure 30 C) with the screen printed layers of the same material (Figure 24, middle row), the superiority of using FSP direct deposition for sensor fabrication becomes obvious. Furthermore, Figure 31 shows that this layer uniformity is not only preserved on the macroscopic scale, but also the microstructure remains homogeneous and extremely porous throughout the whole layer. All three different kind of deposited materials, i.e. SnO_2, Pd-doped SnO_2 and Pd-doped Al_2O_3, form an open and fluffy layer without any formation of larger agglomerates.
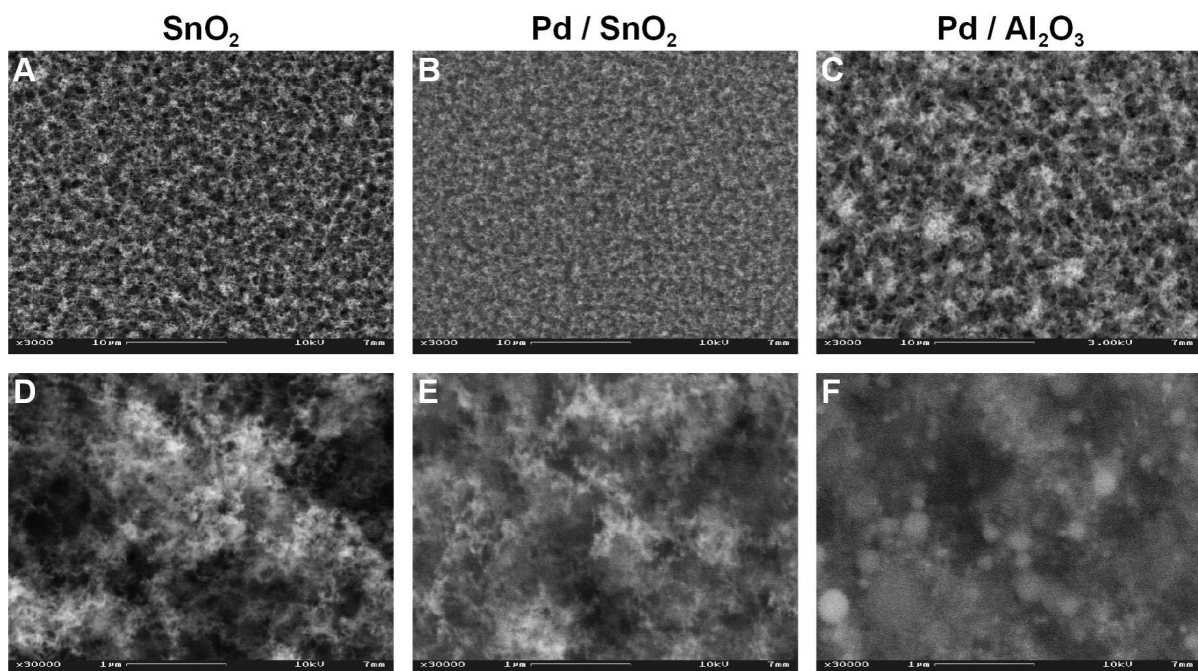
Figure 31: SEM images of the top of the directly deposited layers. The surfaces – especially of the SnO_2 materials (A and B) – are even layers. All layers exhibit a porous structure with a sponge-like distribution of the metal oxide without any agglomerates (D, E and F). The images were taken with a magnification of 3,000 (A, B, C) and 30,000 (D, E, F) at an acceleration voltage of 10 kV (only image C was taken at 3 kV).

With regard to the realised multilayer sensors, it is of major interest to get information about the structure and morphology of the piled layers in the vertical direction. Therefore, the cross sections of the sensors were investigated by SEM analysis (Figure 32). The stacked porous layers showed good uniformity and the thickness of each layer was constant throughout the whole deposited area. This results in highly even layers without any rises and hollows. In the case of the SnO_2 + Pd/Al_2O_3 double layer sensor the

thickness of the Al_2O_3 layer was much smaller than of the SnO_2 layer although the same deposition time was applied. This is the consequence of the thermophoretic deposition where the layer growth rate decreases with increasing layer thickness. The reason is a decreasing temperature gradient as the surface temperature of the deposited layer increases with the growth of the layer (explained in detail in Chapter 3.1.1). Therefore, the next double layer sensor (i.e. Pd/SnO_2 + Pd/Al_2O_3) was fabricated with a longer deposition time for the Al_2O_3 layer.
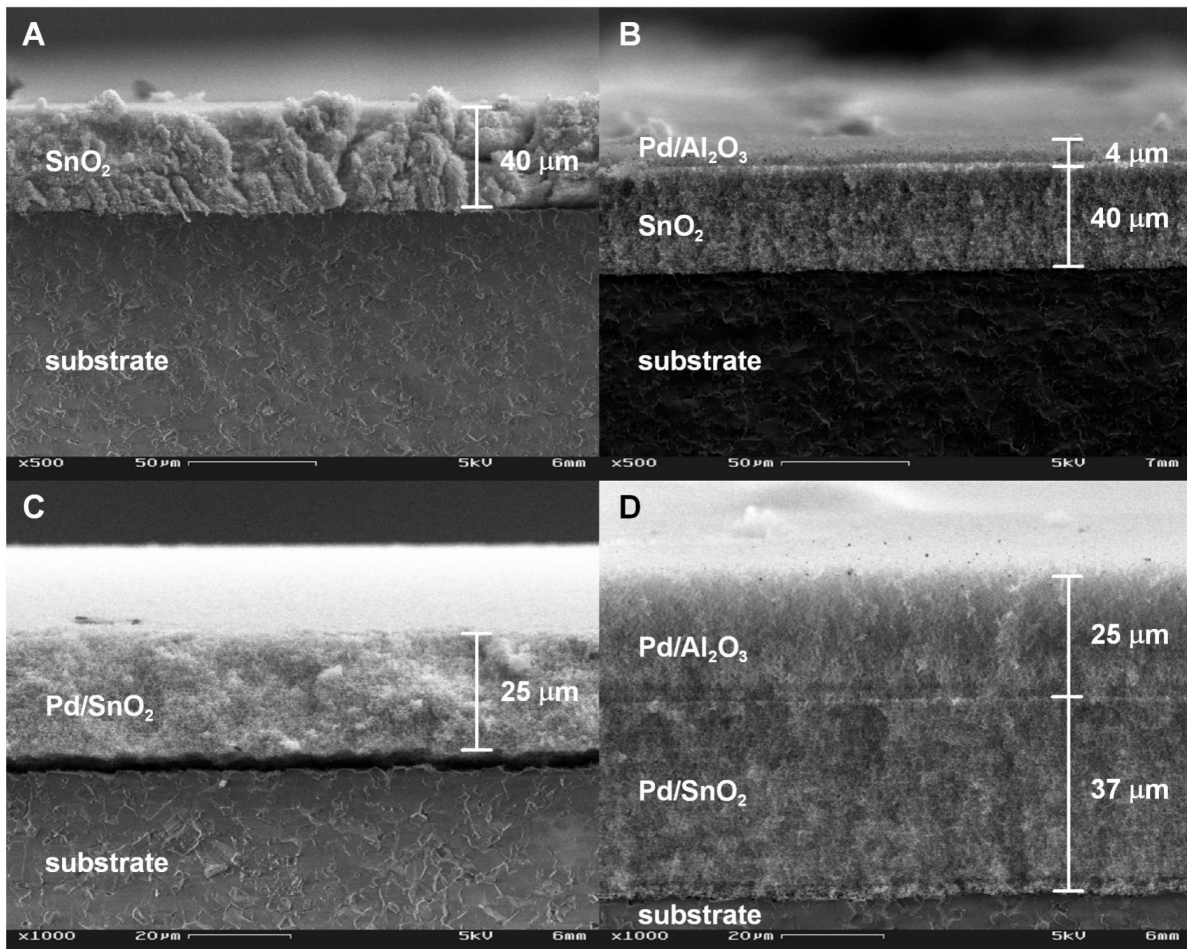
Figure 32: SEM images of the cross sections of the directly deposited sensors. Different sensors are realised: a single SnO_2 layer (A), a Pd/Al_2O_3 layer on top of a SnO_2 layer (B), a single Pd/SnO_2 layer (C), and a Pd/Al_2O_3 layer on top of a Pd/SnO_2 layer (D) deposited on ceramic substrates.

The high uniformity of the directly deposited layers is a key factor that makes the direct deposition via FSP a favourite for sensor fabrication as it also guarantees a high reproducibility for the sensors. The batch-to-batch variations are only small as the conformity of the layer body structure can be controlled.

4.3 Summary

The characterisation of the fabricated material reveals that FSP is a promising technique for the synthesis of metal oxide nanoparticles for gas sensing. The grain size of the material can be adequately controlled. The resulting product consists of monocrystalline particles with a low degree of agglomeration. This nanocrystalline SnO_2 can be subjected to standard deposition methods for sensor fabrication, e.g. screen printing. However, the screen printed layers show cracks and agglomeration due to difficulties in the paste preparation with such small particles.

The *in situ* platinum functionalisation of the SnO_2 particles is possible. The Pt doping does not influence the SnO_2 grain size, the primary crystallite size or the high crystallinity. Additionally, no larger crystalline Pt particles can be found. The platinum is rather highly dispersed on the SnO_2 and shows the oxidation state of Pt^{2+}.

The direct deposition of SnO_2 particles from the flame on sensor substrates is successfully implemented into the fabrication step of the FSP reactor. Thus, it is possible to control the thickness of the deposited layers. All the layers are highly porous and the grain size is independent of the deposition time. Using this setup, even more than one layer can be deposited subsequently after each other. The resulting multilayers are even and uniform, highly porous and without any agglomerates.

To summarize, the established sensor fabrication via the FSP route shows many advantages from a technological point of view compared to state of the art techniques, e.g. *in situ* functionalisation of nanoparticles, highly porous layers, a short and straightforward single-step process. Thus, it is an eligible candidate for future industrial implementation.

5

——— Results & discussion ———

5.1 Feasibility study of FSP material

First of all one has to check whether FSP synthesised metal oxide nanoparticles can be used for gas sensing and what their sensing properties are like if compared with standard materials. Therefore, sensors were fabricated using SnO_2 that was synthesised in an FSP reactor with an 8/3 flame ("SnO_2 8/3"). The powder had a mean grain size of 17 nm and was deposited via spin coating on alumina substrates. By comparison, commercially available SnO_2 powder (Aldrich, 325 mesh) with a mean grain size of 330 nm was subjected to the same process for sensor fabrication. Dc electrical tests have been performed to monitor the response of the sensors to propanal (propionaldehyde, C_3H_6O), CO and NO_2 in dry synthetic air and in synthetic air with 50% relative humidity (r.h.).

5.1.1 Propanal

Figure 33 shows a typical measurement run for dc electrical tests. While delivering different concentration steps of propanal the resistance of the sensor with the FSP material (SnO_2 8/3, black line) and of the sensor with the commercial SnO_2 (SnO_2 com, grey line) are recorded. As expected the resistance of the n-type material decreases due to the interaction with the reducing gas propanal. The measurement was carried out in dry synthetic air at 220°C. Both sensors qualitatively show a similar behaviour with regard to response and recovery time.

The sensors were exposed to propanal at various temperatures between 220°C and 345°C in dry synthetic air and in synthetic air with 50% r.h. The sensor signal S of the sensors towards 150 ppm propanal under these conditions is given in Figure 34. In dry air the SnO_2 8/3 sensor always shows higher signals than the SnO_2 com decreasing with temperature (Figure 31 A). In 50% r.h. the same behaviour is found except for 220°C where the SnO2 8/3 shows very low signal (Figure 34 B). The signals of both sensors are higher in dry air than in humid air, respectively.
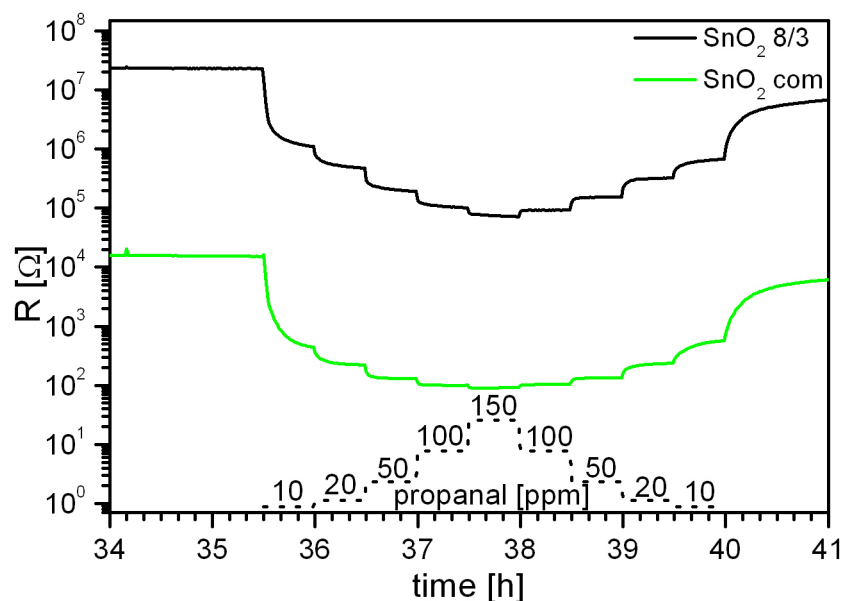
Figure 33: Typical measurement run. The change of the resistance of a SnO₂ 8/3 sensor (black) and of a SnO₂ com (grey) are recorded in dry synthetic air at 220°C for different propanal concentrations (dashed line).
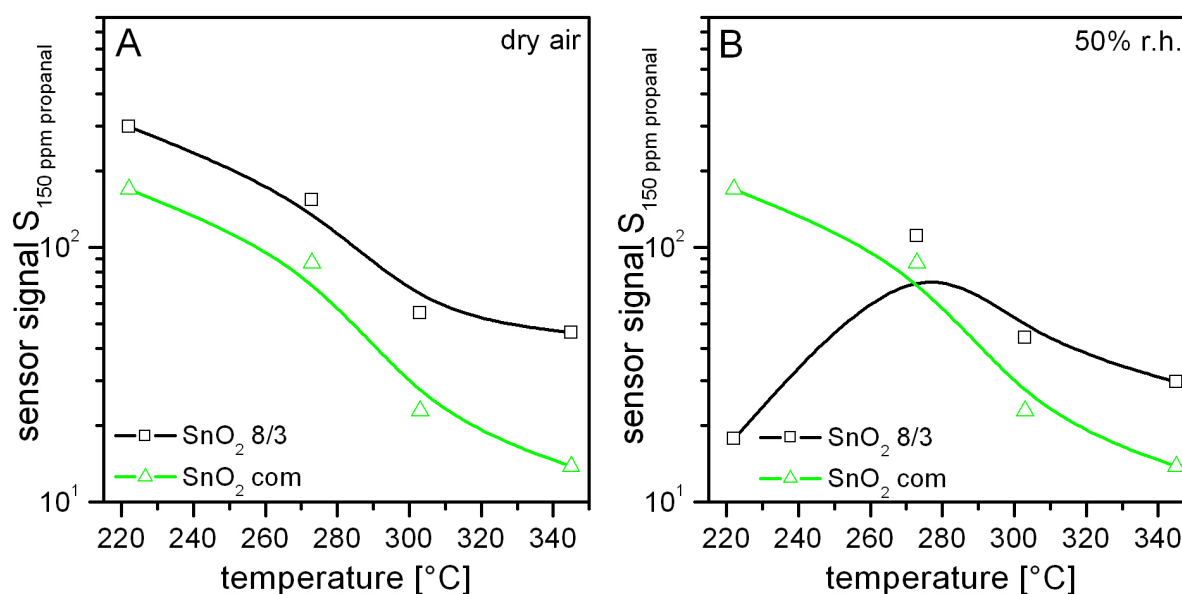
Figure 34: Sensor signal S to 150 ppm propanal at various temperatures. The SnO₂ 8/3 (black) and the SnO₂ com (grey) are measured in dry synthetic air (A) and in 50% r.h. (B).

To gain further information about the correlation between sensor signal S and the concentration of the analyte (propanal in this case), the signal of the sensors for different propanal concentrations are plotted at one temperature, i.e. 300°C in dry synthetic air (Figure 35). The SnO₂ 8/3 shows slightly higher signals than the SnO₂ com; the trend is becoming more obvious at higher propanal concentrations. This means that the SnO₂

com gets saturated already at lower concentrations. Both sensors show a power law dependency. The SnO$_2$ 8/3 can be fitted with the calibration function $S = 1 + 1.517 \times c^{0.630}$ and the SnO$_2$ com with the calibration function $S = 1 + 2.501 \times c^{0.438}$. The larger exponent of the SnO$_2$ 8/3 represents a steeper increase of the signal with an increase of the propanal concentration.
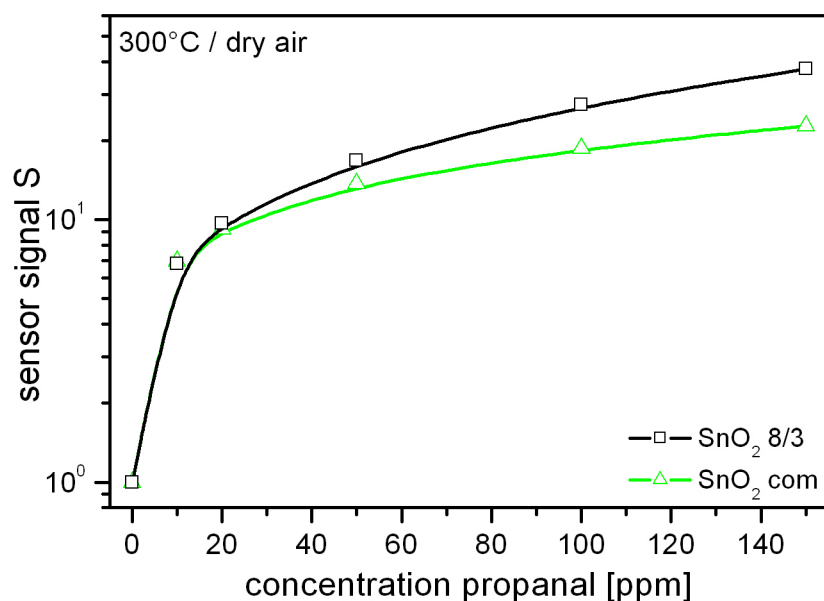
Figure 35:   Sensor signal S dependence on propanal concentration for SnO$_2$ 8/3 (black) and SnO$_2$ com (grey). The measurement is performed at 300°C in dry synthetic air.

5.1.2 CO

Under the same measurement condition as for the propanal investigation the sensors were exposed to CO concentrations between 500 ppm and 10,000 ppm. The sensor signal S to 5,000 ppm CO in dry synthetic air and in synthetic air with 50% r.h. is shown for different temperatures in Figure 36. In dry air as well as in humid air, the SnO$_2$ 8/3 sensor shows always higher signals than the SnO$_2$ com sensor. However, the sensor signal is quite low compared to propanal – even for very high CO concentrations. This is a typical behaviour of undoped material [157]. Humidity decreases the signal for both sensors, which is also known [81].
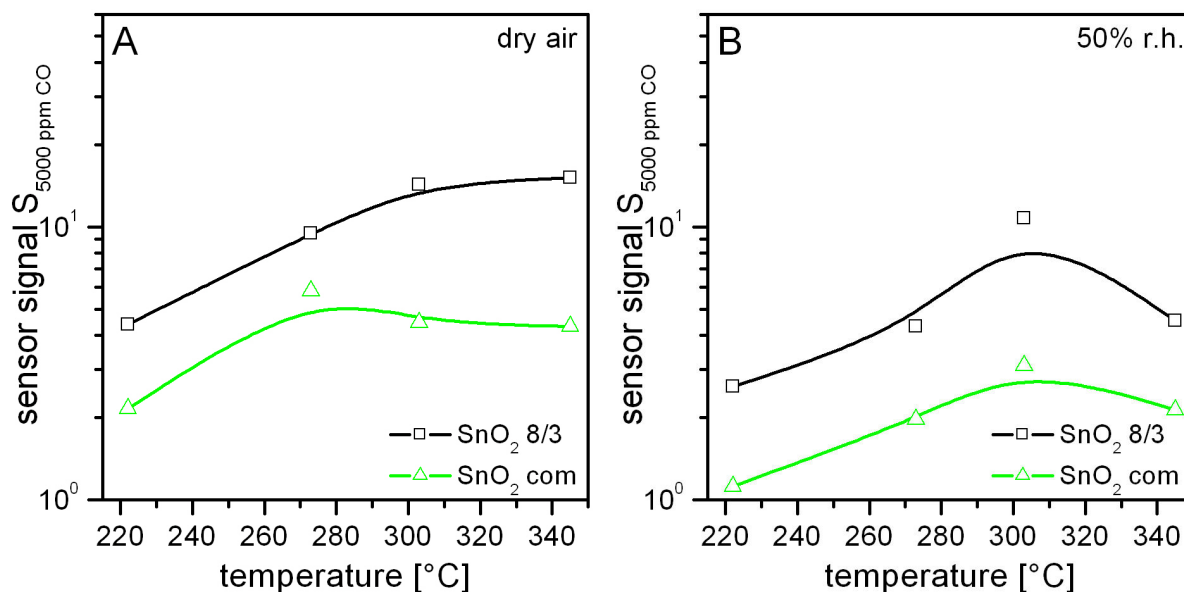
Figure 36: Sensor signal S to 5,000 ppm CO at various temperatures. The SnO_2 8/3 (black) and the SnO_2 com (grey) are measured in dry synthetic air (A) and in 50% r.h. (B).

The sensing behaviour of the two sensors at 300°C in dry synthetic air for different CO concentrations between 500 ppm and 10,000 ppm is shown in Figure 37. The signal of the SnO_2 8/3 is much higher than of the SnO_2 com (of about a factor of 3). This is also displayed by the fitted calibration functions: $S = 1 + 0.179 \times c^{0.515}$ for SnO_2 8/3 and $S = 1 + 0.211 \times c^{0.359}$ for SnO_2 com.
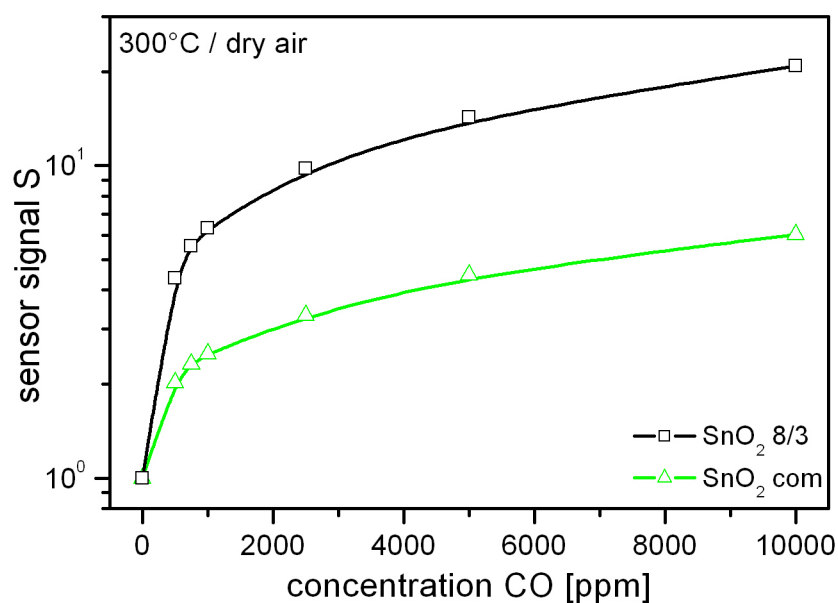
Figure 37: Sensor signal S dependence on CO concentration for SnO_2 8/3 (black) and SnO_2 com (grey). The measurement is performed at 300°C in dry synthetic air.

5.1.3 NO₂

As a probe molecule for oxidising gases NO₂ has been chosen to test the fabricated sensors. Different NO₂ concentrations between 10 ppb and 4800 ppb were delivered to the sensors in a pulse mode, i.e. after each pulse of NO₂ the sensors were exposed to synthetic air before the next NO₂ concentration was delivered. Figure 38 shows the results of these measurements at 220°C in dry synthetic air. The actual NO₂ concentration was measured online with a NOₓ analyzer (Figure 38 A). As expected the resistances of both sensors increased due to the interaction with NO₂ (Figure 38 B). The sensor signal for SnO₂ com is higher than for SnO₂ 8/3 at lower NO₂ concentrations. However, at higher concentrations the difference between the sensors diminishes (Figure 38 C). The corresponding calibration functions are $S = 1 + 0.220 \times c^{0.523}$ for SnO₂ 8/3 and $S = 1 + 0.406 \times c^{0.493}$ for SnO₂ com.
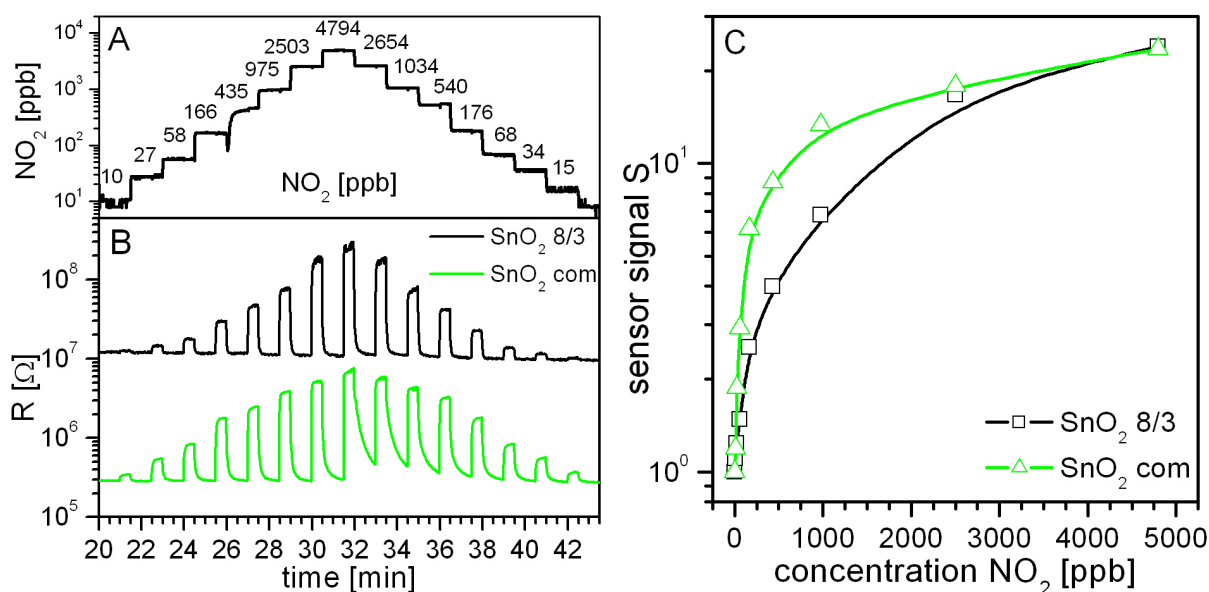
Figure 38:   Dc electrical tests with NO₂. The actual NO₂ concentration is monitored by a NOx analyzer (A) while the resistances of the SnO₂ 8/3 (black) and SnO₂ com (grey) are recorded (B). The sensor signal S is given for various NO₂ concentrations at 220°C in dry synthetic air (C).

5.1.4 Summary

The performed feasibility study has clearly shown that SnO₂ nanoparticles synthesised by an FSP reactor can be successfully used as gas sensing material. Sensors prepared with

FSP generated SnO_2 showed under identical conditions comparable sensor signals to the sensors with commercial SnO_2 for all investigated gases. In several cases (for propanal and CO) the FSP made sensor showed even a better sensing performance than the sensor with commercial SnO_2 material. This legitimates a further study on the possibilities of FSP nanoparticle synthesis for gas sensing applications.

5.2 Simultaneous work function and resistance measurements

After confirming the potential of FPS synthesis for gas sensing applications, some more fundamental investigation had to be carried out to get insight into the sensing reactions and the underlying solid-gas interactions at the surface of the synthesised SnO_2. It is important to not only improve the presented FSP technique for gas sensing by a trial-and-error approach but to understand what is going on a molecular level. This is because the adsorption and desorption processes of the analytes on a certain metal oxide (e.g. CO on SnO_2 sensors) depend on many factors, amongst them the applied technology for SnO_2 synthesis and for deposition of the latter [24].

As seen in Chapter 5.1, the typical measurement technique for metal oxide gas sensors is the measurement of resistance. However, recent investigations have shown the need of combining results obtained by different techniques to achieve additional information and thus to get deeper insight into the reactions at the sensor's surface [20]. For example, the combination of work function change and resistance change measurements provides knowledge about those surface species that build up local dipoles. To increase the knowledge about the SnO_2 synthesised by FSP, simultaneous work function and resistance measurements have been performed on standard screen printed sensors investigating CO, humidity and oxygen.

5.2.1 CO and humidity

CO is one of the most investigated probe molecules for SnO_2 gas sensors. However, the reaction mechanism is not fully understood yet, especially when humidity is present as an interferant. For the present study, three different cases have been investigated: (i) interaction of CO with SnO_2 in the background of dry synthetic air, (ii) influence of water on the SnO_2 surface and (iii) competing interaction of CO and water with SnO_2. The sensor was exposed to different CO concentrations between 5 ppm and 240 ppm in dry synthetic air and in synthetic air with 50% r.h. During all measurements the sensor was kept at a constant temperature of 380°C. The main results can be summarised as follows:

- the reaction of the SnO_2 surface with CO in dry air only leads to changes in band bending and no changes in electron affinity ($q\Delta V_S < 0$ and $\Delta\chi = 0$, see Figure 39 A);

- increasing humidity leads to a decrease in band bending, but to an increase in electron affinity ($q\Delta V_S < 0$ and $\Delta\chi > 0$, see Figure 41);

- the presence of humidity decreases the effect of CO on band bending ($q\Delta V_{S\,(CO\,in\,humid\,air)} < q\Delta V_{S\,(CO\,in\,dry\,air)}$, see Figure 39 B);

- the latter effects are additive, i.e. the sum of the changes in band bending due to water and due to CO in the background of water is nearly equal to the change in band bending due to CO in dry conditions ($q\Delta V_{S\,(humid\,air)} + q\Delta V_{S\,(CO\,in\,humid\,air)} = q\Delta V_{S\,(CO\,in\,dry\,air)}$, compare Figure 39 and Figure 41);

- additionally, in the presence of humidity, the interaction with CO increases the overall electron affinity ($\Delta\chi > 0$, see Figure 39 B);

- nevertheless, more than one dipole species is involved in the latter reaction (Figure 43).
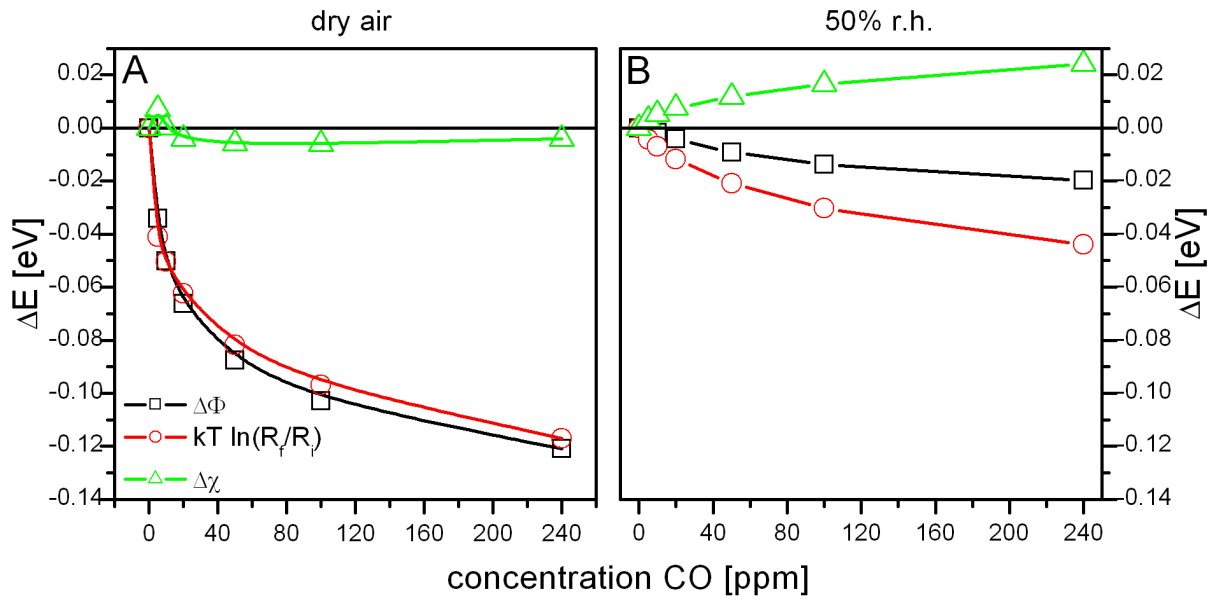
Figure 39: Changes in work function ($\Delta\Phi$), band bending ($kT \ln(R_f/R_i)$) and electron affinity ($\Delta\chi$) with increasing CO concentration in dry synthetic air (A) and in synthetic air with 50% r.h. (B).

The results of the measurements with CO in dry air (Figure 39 A) are in agreement with the models that have been proposed so far [19, 27]. The observation that band bending ($q\Delta V_s = kT \ln(R_f/R_i)$) decreases due to the interaction of the sensing layer with CO can be explained by a reaction of CO with pre-adsorbed oxygen species on the surface which is under the given circumstances most probably O^-.
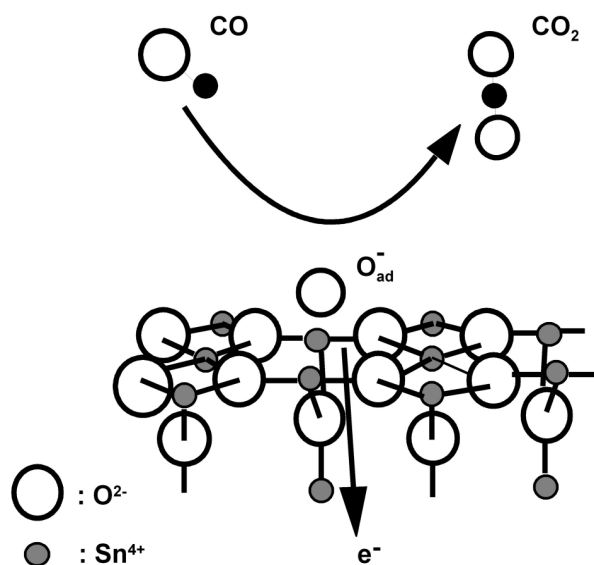
Figure 40: Model for the interaction of CO with a reduced SnO_2 (110) surface. CO reacts via ionosorbed oxygen under release of an electron to the conduction band to form CO_2.

The oxidation of CO to CO_2 releases an electron of the ionosorbed oxygen to the conduction band and thus decreases the band bending. Figure 40 sketches these considerations.

As can be seen from Figure 41, increasing humidity leads to different kinds of surface species, one contributing to an overall charge transfer with the conduction band and one forming local dipoles. The first one is represented by a decrease in band bending and the second one by an increase in electron affinity (Figure 41).
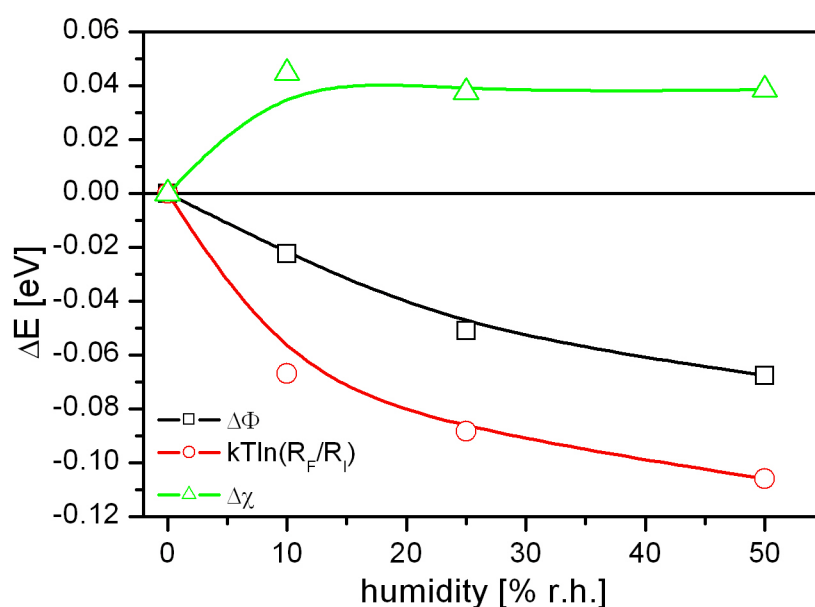
Figure 41:   Changes in work function ($\Delta\Phi$), band bending ($kT \ln(R_f/R_i)$) and electron affinity ($\Delta\chi$) with increasing humidity.

Unfortunately, these measurements do not give direct information about what kind of species are present at the surface. Different models for the interaction of water and metal oxide surface have already been presented in Chapter 2.2.2. Briefly, the result of these models would be:

- homolytically dissociated water forms a rooted OH-group and a terminal OH-group – The rooted OH-group can act as a donor under release of an electron ($q\Delta V_S < 0$), whereas the terminal OH-group builds up a local dipole $Sn^{\delta+}-(OH)^{\delta-}$ ($\Delta\chi > 0$) (see Equation 2 and Figure 42 A) [69].

- homolytically dissociated water forms two terminal OH-groups via an ionosorbed oxygen – With respect to work function change measurements, these OH-groups represent local dipoles and thus are expected to increase the electron affinity ($\Delta\chi > 0$). During the reaction, O^- releases its electron to the conduction band of the semiconductor ($q\Delta V_S < 0$) (see Equation 3 and Figure 42 B) [71, 72].
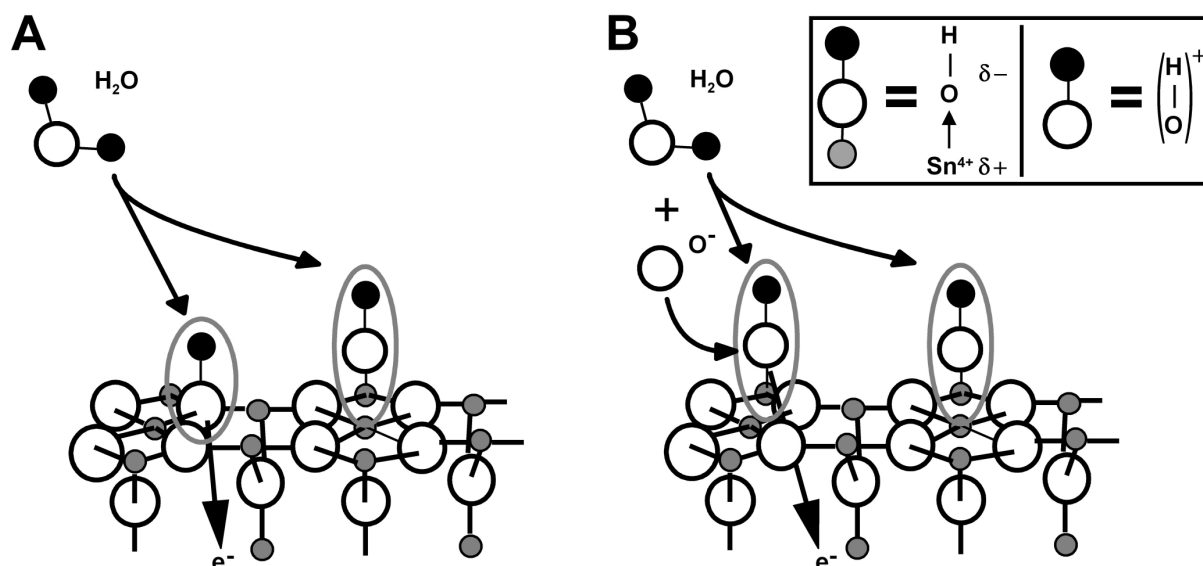
Figure 42:   Two models for the interaction of water with a reduced SnO_2 (110) surface. Homolytically dissociated water builds an OH-group bonded to a Sn-atom of the lattice and an OH-group with an oxygen from the lattice. The latter acts as a donor under release of an electron (A). Homolytically dissociated water reacts with a pre-adsorbed oxygen ion to form two OH-groups on Sn-atoms of the lattice. The electron of the oxygen ion is released to the conduction band (B).

One cannot distinguish between these two mechanisms just on the basis of the work function change and resistance measurements in the case of increasing humidity. However, taking into account the results of CO measurements in the presence of humidity, i.e. the smaller effect of CO on band bending in the humid case, only the second mechanism for the interaction of water with the tin dioxide surface is supported. As this reaction path for water consumes O^-, it is obvious that the effect of CO which also reacts via O^- is smaller than in the absence of water. This competition between water and CO for pre-adsorbed oxygen species leads to a less decreasing band bending in humid air than in dry air as the number of oxygen species is limited (Figure 39). In this model, the origin of the changes in band bending is the same for both, the interaction of

water and of CO with SnO_2. In both cases, the consumption of ionised oxygen species leads to a release of electrons. Therefore, the effects are additive and the change in band bending due to humidity plus the change in band bending due to CO in humidity is almost equal to the change in band bending due to CO in dry conditions (compare Figure 39 and Figure 41).

On the other hand, such a competitive reaction would lead, with increasing CO concentration, to a decrease of the terminal OH-groups due to a decrease of O^- (Equation 3). Thus, the electron affinity is expected to decrease. Figure 39 clearly shows an overall increase in the electron affinity. These measured changes of electron affinity display the overall change which might be a sum of different kinds of dipoles on the surface. A total increase in electron affinity therefore means that the dominating effect is the one leading to a positive change in electron affinity but could also contain species leading to a negative change. Figure 43 shows the development of work function, band bending and electron affinity with time for two given CO concentrations in the background of humidity. By increasing the CO concentration from 10 ppm to 240 ppm, one observes a very fast and strong decrease in electron affinity in region A. This decrease supports the above mentioned mechanism where the reaction of CO with O^- leads to a decrease in terminal OH-groups. But in the course of time, another dipole species appears, leading to an increase in electron affinity. As can be seen in region B of Figure 43, this species finally dominates the total effect. At the same time, this appearance of dipoles is totally unaffected by those reactions which change the band bending. Talking about humid conditions, one always has to bear in mind the possibility of molecular bonded water. Thiel and Madey [67] report that the interaction of molecular water and oxide surfaces can be described in terms of Lewis acid-base behaviour. In this picture, one expects water to bind either via the oxygen atom to the cationic sites or to bind via the hydrogen atom to the anionic sites. The first case would result in a decrease in electron affinity ($\Delta\chi < 0$) due to a charge donation from the adsorbed water to the surface. The second case would therefore lead to an increase in electron affinity ($\Delta\chi > 0$). Unfortunately, no experimental evidence could be gained yet that these molecular water species are involved in the interaction of CO with SnO_2 in humid conditions, but they should be taken into account for further modelling.
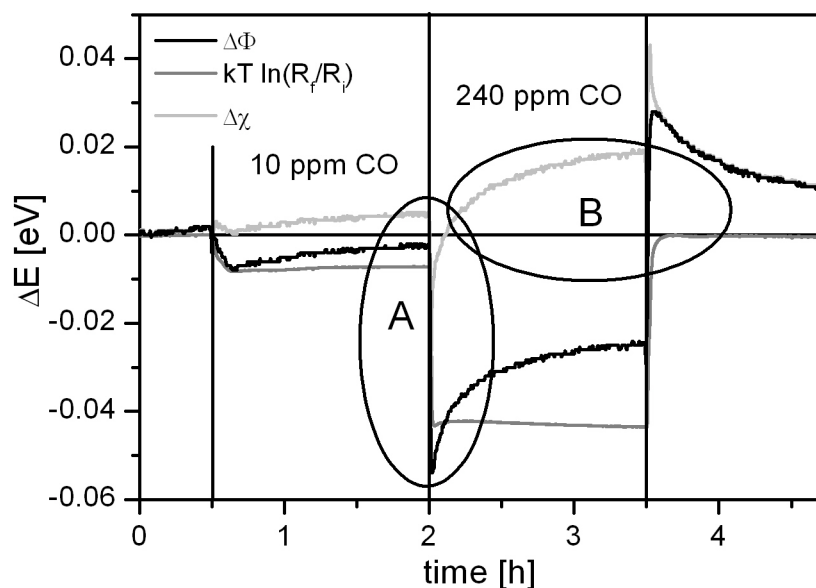
Figure 43: Development of work function ($\Delta\Phi$), band bending ($kT \ln(R_f/R_i)$) and electron affinity ($\Delta\chi$) over the time for two different CO concentrations (10 ppm and 240 ppm) in the background of synthetic air with 50% r.h. Region A shows the development of $\Delta\chi$ shortly after increasing the CO concentration, whereas region B displays the situation after a longer period of time.

5.2.2 Oxygen

As shown in the previous section, pre-adsorbed oxygen species are often involved in the adsorption processes of analytes on the metal oxide surface. Therefore, it is desired to know which kinds of oxygen species are present under which conditions. However, despite many studies the mechanism by which the interplay between O_2 and the SnO_2 surface occurs is still very poorly understood. The two main species are molecular ($O_{2(ads)}$ or $O_{2(ads)}^-$) and atomic ($O_{(ads)}$ or $O_{(ads)}^-$) oxygen. Their appearance depends mainly on the temperature, i.e. molecular forms at lower temperatures and atomic forms at higher temperatures. For this reason, measurements with different O_2 concentrations between 300 ppm and 6,000 ppm have been performed at two temperatures (200°C and 400°C). A constant background of 50 ppm O_2 and less than 10 ppm H_2O could be maintained. The main observations of the oxygen investigation are the following:

- at high temperatures (400°C), increasing oxygen concentration leads to an increase in band bending ($q\Delta V_S > 0$) and to a comparable increase of the work function ($\Delta\Phi > 0$, see Figure 44 B);

- at low temperatures (200°C), increasing oxygen concentration leads to an increase in band bending ($q\Delta V_S > 0$) and to a strong decrease of the work function ($\Delta\Phi < 0$, see Figure 45);

- all effects are reversible ($q\Delta V_S = 0$, $\Delta\chi = 0$, $\Delta\Phi = 0$ after 50 hours);

Generally, the processes described by Equation 21 – 24 are taken into consideration when analyzing the adsorption of oxygen.

$$O_{2(gas)} \leftrightarrows O_{2(ads)} \tag{21}$$

$$O_{2(ads)} + e^- \leftrightarrows O_{2(ads)}^- \tag{22}$$

$$O_{2(ads)} \leftrightarrows 2\,O_{(ads)} \tag{23}$$

$$O_{(ads)} + e^- \leftrightarrows O_{(ads)}^- \tag{24}$$

All these processes are equilibrium reactions, and the extent to which they occur depends very much on the temperature, the partial pressure of oxygen, and on the characteristics of the adsorbent. If one assumes that at high temperatures the processes described above end up with ionosorbed species (i.e. without any localized bond to the surface), one would expect a change in band bending which is of the same value as the change of the work function, and therefore no change of the electron affinity (as described in Chapter 2.2). This behavior has been found for all delivered oxygen concentrations at 400°C (Figure 44 B).

The results shown in Figure 44 strongly suggest that at 400°C all other species, beside ionic ones, can be regarded as being of secondary importance. However, at 200°C a completely different behavior of the changes of the work function appeared. This is illustrated by Figure 45, where changes in work function, band bending and electron affinity due to a pulse of 300 ppm oxygen are displayed for 200°C and 400°C, respectively.
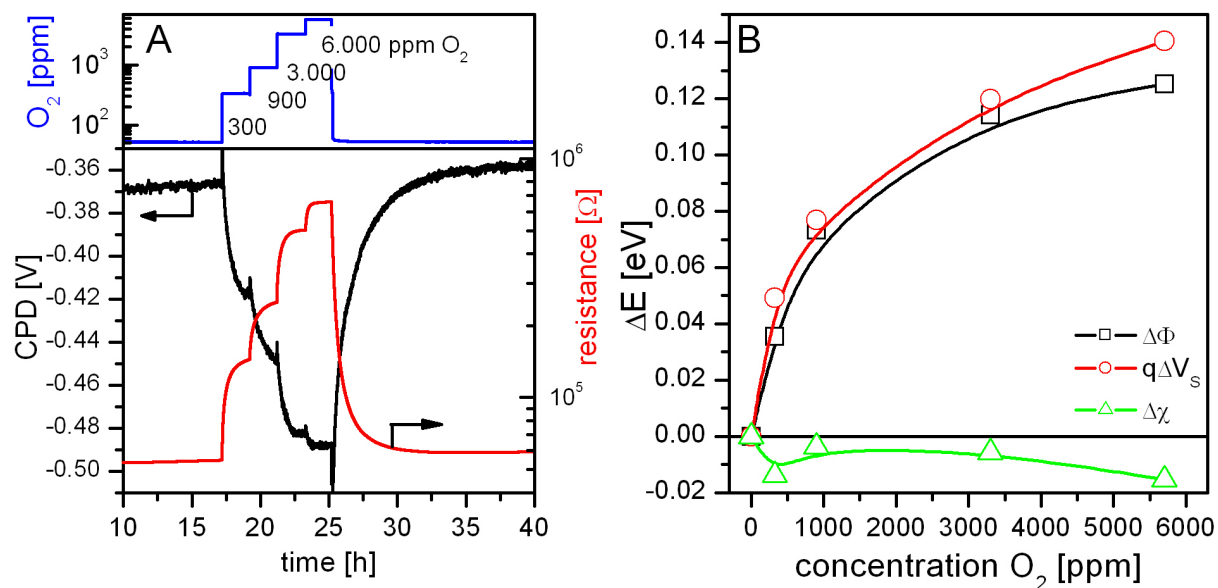
Figure 44: Measurement run at 400°C in dry synthetic air. The contact potential difference (CPD, black) and the resistance (grey) are recorded while different O_2 concentrations (grey line at top) are dosed to the sensor (A). Changes in work function (□), band bending (○) and electron affinity (△) are shown with increasing O_2 concentration (B).
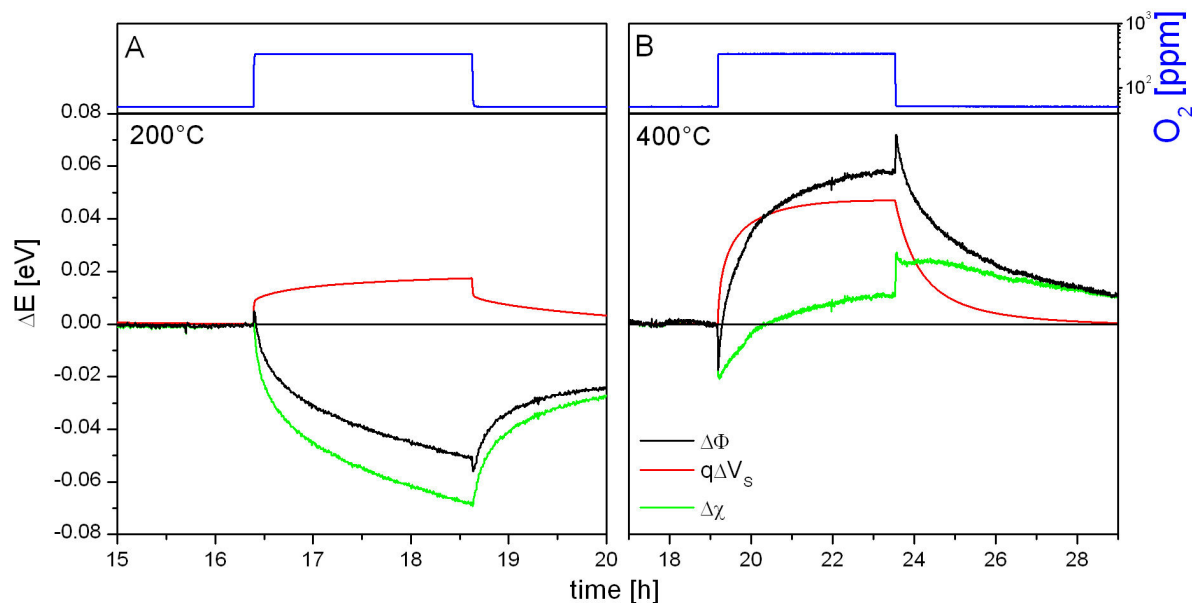
Figure 45: Changes in work function (black), band bending (dark grey) and electron affinity (light grey) due to 300 ppm O_2 (grey line at top) at 200°C (A) and at 400°C (B).

The most important difference is the strong decrease in electron affinity at 200°C. Such effects did not appear at 400°C. Changes in electron affinity are connected with the formation or loss of dipolar species between adsorbate and adsorbent accompanied by a

localized bonding. Therefore, the experimental results can only be explained by allowing for the possibility of dipoles carrying neutral molecular oxygen species.

It is challenging to get experimental results about the nature of neutral oxygen surface species as shown in Chapter 2.2.1. Therefore, theoretical studies of the stability of oxygen molecules on SnO_2 surfaces can provide some guidance. First-principle calculations have shown that molecular oxygen is not adsorbed on a perfect stoichiometric surface of SnO_2 [63]. However, in the presence of vacancies different conformations of adsorbed oxygen molecules are energetically favored. There is a twisted geometry, where the oxygen molecule is planar to the SnO_2 (110) surface and bonded to two fourfold Sn_{4f}^{2+} (Figure 46 a). This adsorbed species has a binding energy ($E_{binding}$) of 0.92 eV and is expected to pick up electronic charge due to a reduced Sn^{2+} and thus become a peroxide ion (Figure 46 b). Besides, a stable state on a fivefold Sn_{5f}^{4+} site ($E_{binding}$ = 0.11 eV) with the molecule axis tilted at ~70° from the normal was found (Figure 46 c).
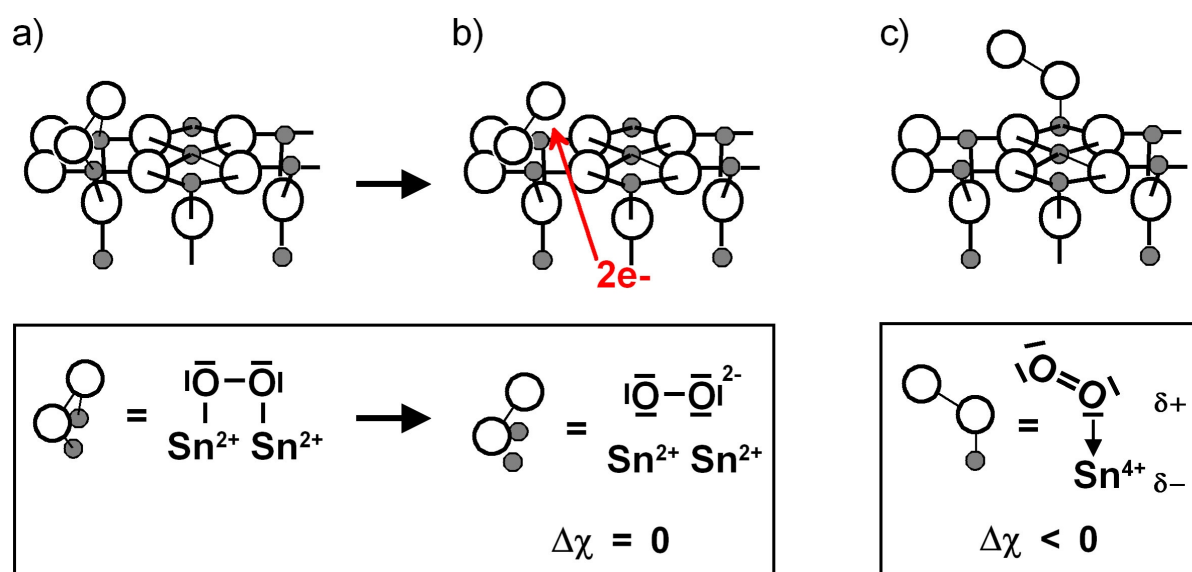
Figure 46: Adsorption of O_2 on a reduced SnO_2 (110) surface. There is a stable state for a twisted conformation on a fourfold Sn^{2+} site according to [63] (a). It is expected to accept negative charge under building of ionosorbed species and thus without influence on electron affinity (b). A stable conformation tilted from the normal, where a Lewis acid/base interaction leads to a local dipole with a negative partial charge on the tin and thus to a decrease in χ, is also reported (c).

For the latter conformation, the driving force of the bonding is a Lewis acid/base interaction between the Sn^{4+} and an unbounded electron pair of the oxygen and leads to a partial negative charge of the Sn site (Lewis acid), whereas the oxygen molecule will acquire a partial positive charge (Lewis base). This localized dipolar interaction leads to a decrease in electron affinity. Therefore, these theoretical calculations are in accordance with the observed experimental results assuming that these neutral oxygen species will not be stable at the higher temperature (400°C).

5.2.3 Summary

The combination of simultaneous work function change and resistance measurements allowed for an investigation of surface species – both ionised and dipolar – on the surface of FSP generated SnO_2 nanoparticles. Special emphasis was put on those surface species that are related with three of the main gaseous compounds present in many applications, i.e. CO, humidity and oxygen.

The results obtained for CO in dry air, for humidity and for oxygen at high temperature (400°C) were in line with the models described in literature: (i) CO reacts with pre-adsorbed oxygen ions, (ii) water dissociates homolytically and forms terminal hydroxyl groups with a pre-adsorbed oxygen ion, and (iii) oxygen adsorption ends up with ionosorbed species.

Additionally, under certain conditions hints for some surface species could be gathered that are invisible for standard resistance measurements and that influence the electron affinity of the SnO_2: (i) molecular water that is bond via Lewis acid/base interaction to the surface and (ii) molecular oxygen in a tilted configuration at low temperatures (200°C) with one oxygen atom donating partial negative charge towards a Sn site of the solid.

As mentioned before, one has to be careful when generalising these findings. The results were specifically obtained on undoped SnO_2 powder that was synthesised by FSP. In the case of SnO_2 with another fabrication history the situation might be different. Therefore, the gained information about adsorption and desorption processes on a molecular level

are of capital importance specially for improving the use of FSP for gas sensor fabrication.

5.3 Influence of deposition method

Besides using FSP generated nanoparticles for gas sensing the full integration of this method into a single-step sensor fabrication is the main topic of the present work. In a first benchmarking experiment, the properties of directly deposited sensors were compared with standard deposition techniques in research and industry, i.e. screen printing and spin coating. Undoped SnO_2 with a grain size of 10 nm was synthesised in the FSP reactor using a 5/5 flame. The thus fabricated nanoparticles were directly deposited on alumina substrates with a deposition time of 180 s. This results in a layer thickness of 30 μm. Simultaneously to the direct deposition, SnO_2 powder was collected from the filter and used for screen printing and spin coating on the same alumina substrates.

5.3.1 Temperature dependency

The sensor signal for the three sensors deposited by different techniques was recorded for 50 ppm CO and 25 ppm ethanol at various operating temperatures. Figure 47 shows the sensor signals for CO in dry synthetic air (Figure 47 A) and in synthetic air with 50% r.h. (Figure 47 B). In general, the sensing behaviour of the directly deposited sensor is comparable to the other deposition methods. In dry air, the temperature tendency is more like the screen printed sensor than the spin coated one, i.e. the sensor signal decreases with increasing temperature from 300°C to 450°C by a factor of about three while the sensor signal for the spin coated sensor is almost independent of the operating temperature. The presence of humidity decreases the signal of the sensors compared to the dry case which is known for undoped SnO_2 [81]. However, at higher temperature the directly deposited sensor shows higher sensor signals than in the absence of humidity. The temperature dependency for the directly deposited sensor in the presence of humidity is also different, i.e. the sensor signal of the latter increases with increasing

temperature. These two findings indicate that the SnO_2 surface is differently hydroxylated in the case of the directly deposited layer compared to screen printed and spin coated layers.
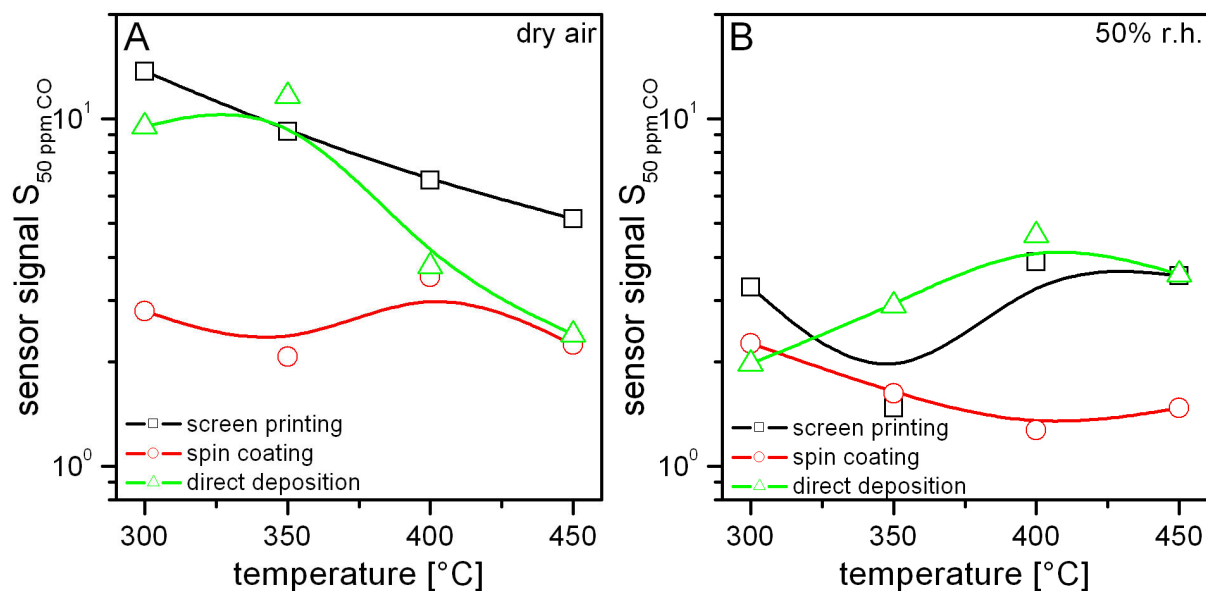
Figure 47:   Sensor signal S to 50 ppm CO at various temperatures. The screen printed (black squares), spin coated (dark grey circles) and directly deposited (light grey triangles) SnO_2 sensors are measured in dry synthetic air (A) and in 50% r.h. (B).

The sensing behaviour towards ethanol as another important probe molecule in gas sensing is shown in Figure 48. In dry conditions (Figure 48 A) the signals of the directly deposited sensor are lower than of the others and show a stronger decrease with increasing temperature. The presence of humidity (Figure 48 B) leads to higher signals for ethanol for the directly deposited sensor. The ethanol sensing of the other sensors is rather unaffected by humidity, especially for the spin coated one.
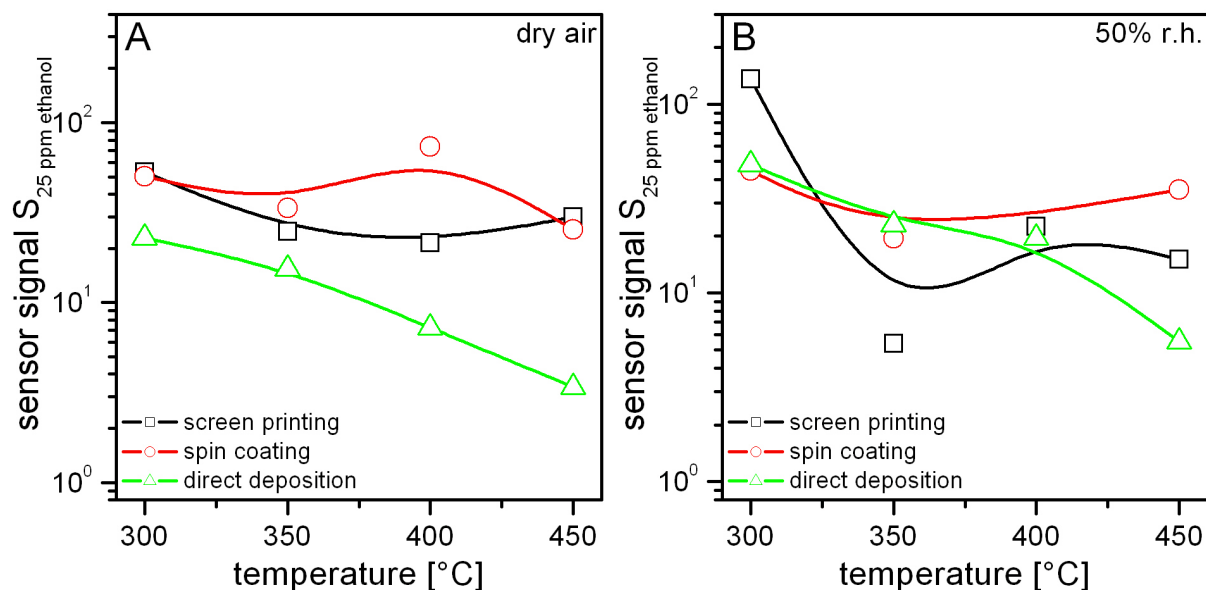
Figure 48: Sensor signal S to 25 ppm ethanol at various temperatures. The screen printed (black squares), spin coated (dark grey circles) and directly deposited (light grey triangles) SnO_2 sensors are measured in dry synthetic air (A) and in 50% r.h. (B).

5.3.2 Concentration dependency

For gas sensors not only the sensor signal at one certain gas concentration is of interest, but also how the signal of the sensor and the concentration of the analyte are correlated. Therefore, the three sensors were exposed to various CO and ethanol concentrations in dry synthetic air and in synthetic air with 50% r.h. at a constant operating temperature of 350°C.

For CO, the directly deposited sensor shows the highest signals for both dry air and humid air (Figure 49). In dry air direct deposition and screen printing lead to a similar sensor performance while spin coating shows only little signals. With humidity in the background all sensor signals for CO decrease. However, the directly deposited decreases least.
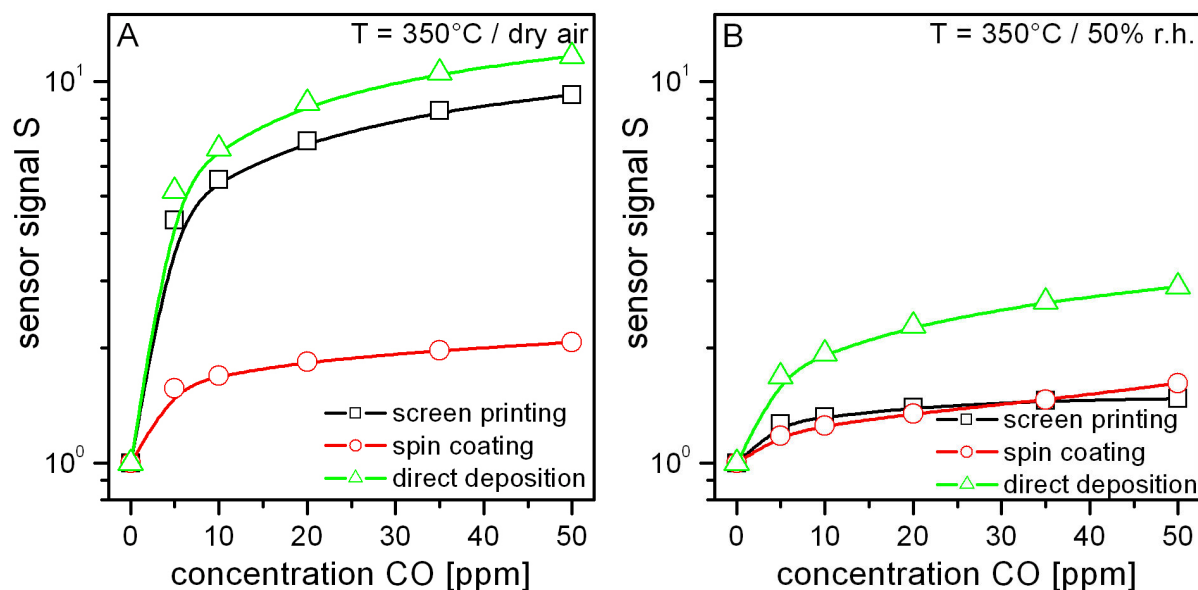
Figure 49: Sensor signal S dependence on CO concentration for screen printed (black squares), spin coated (dark grey circles) and directly deposited (light grey triangles) SnO_2 sensors. The measurements are performed at 350°C in dry synthetic air (A) and in synthetic air with 50% r.h. (B).

Table 8 lists the fitted calibration functions for the different sensors under the corresponding measurement conditions. To put it simple, the exponent gives a measure of the shape of the curve, i.e. how steep the slope is. For example, the screen printed and the directly deposited sensor show a similar shape of the sensor signal, displayed by similar exponents (x = 0.410 and 0.359) whereas the value for the spin coated sensor is much smaller (x = 0.121). The pre-exponential factor gives a hint for the height of the sensor signal curve, i.e. the initial increase at low concentrations.

Table 8: Calibration function $S = 1 + a \times c^x$ of the sensors deposited by different techniques for CO (5 – 50 ppm) and ethanol (2 – 25 ppm) in dry synthetic air and in synthetic air with 50% r.h.

conditions	Calibration function for SnO_2 sensors fabricated by		
	screen printing	spin coating	direct deposition
CO (dry air)	$S = 1 + 2.571 \times c^{0.410}$	$S = 1 + 1.284 \times c^{0.121}$	$S = 1 + 2.925 \times c^{0.359}$
CO (50% r.h.)	$S = 1 + 1.133 \times c^{0.069}$	$S = 1 + 0.936 \times c^{0.131}$	$S = 1 + 1.137 \times c^{0.237}$
ethanol (dry air)	$S = 1 + 3.772 \times c^{0.589}$	$S = 1 + 5.942 \times c^{0.548}$	$S = 1 + 2.213 \times c^{0.610}$
ethanol (50% r.h.)	$S = 1 + 1.420 \times c^{0.410}$	$S = 1 + 2.714 \times c^{0.619}$	$S = 1 + 3.675 \times c^{0.566}$

The sensor signals of the different sensors for ethanol at 350°C are shown in Figure 50. Ethanol sensing of the directly deposited sensor is relatively unaffected by humidity, whereas the signals for the screen printed and the spin coated sensors decrease (see also fitted values in Table 8). The screen printed sensor shows only low signals for ethanol in humid air.
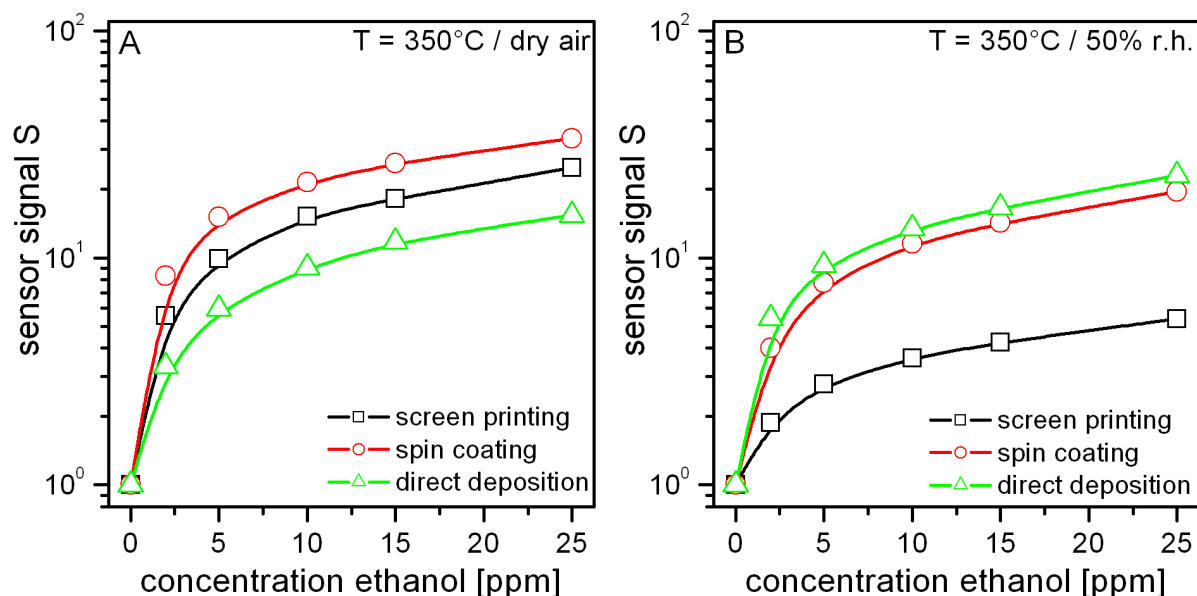
Figure 50:   Sensor signal S dependence on ethanol concentration for screen printed (black squares), spin coated (dark grey circles) and directly deposited (light grey triangles) SnO_2 sensors. The measurements are performed at 350°C in dry synthetic air (A) and in synthetic air with 50% r.h. (B).

5.3.3 Summary

The direct deposition of SnO_2 nanoparticles directly from the flame of a FSP reactor on standard sensor substrates could be established successfully with regard to gas sensing performance. When compared to standard deposition methods like screen printing and spin coating the directly deposited sensor showed good gas sensing behaviour.

In the case of CO, the directly deposited sensor was even superior as it revealed the highest signals in dry as well as in humid air. Sensing of ethanol could be achieved almost independently of the background humidity for the directly deposited sensor while the others showed a strong decrease under the same conditions.

5.4 Effect of platinum doping

As already seen in the previous chapters the sensing behaviour of the undoped SnO_2 for CO is relatively poor. However, a reliable and secure monitoring of CO is of great interest – especially in the low concentration range, i.e. below 50 ppm. This is because CO is a toxic gas that accompanies almost all combustion processes but is not detectable by the human nose. There are several guidelines for maximum CO exposure upon humans, e.g. in Germany the Maximale Arbeitsplatz Konzentration (MAK) gives a maximum concentration of a chemical substance in the work-place (eight-hour time weight average value) which is set for CO at 30 ppm. Even more striking, the limit value of CO (here maximum daily eight hour mean) for the protection of human health to be met in 2005 was set at 10 mg/m^3 (8.75 ppm) by the European Commission [158].

One approach to improve the sensing performance of SnO_2 is the use of noble metals, so called dopants (e.g. Pt or Pd). The aim is to decrease the response and recovery times, and increase the sensitivity, selectivity, reproducibility and stability of the sensors [86, 159]. Unfortunately, no generalisation for the interaction mechanism of the dopants can be made (see also Chapter 2.3). Parameters like the amount, chemical state, aggregation and localisation of the noble metal atoms can influence the sensing properties in completely different ways – even if the same base material (i.e. SnO_2) is used [85, 89, 160, 161, 162]. Moreover, the situation will be different if the noble metal forms isolated metallic nanoparticles of a few nanometers ("metallic clusters") or is getting oxidised and diffusing into the lattice of base material (SnO_2) forming solid-solutions (this is especially favourable for platinum because PtO_2 has the crystalline structure of rutile – the same as SnO_2, i.e. cassiterite).

Therefore, *in situ* functionalised (with platinum) SnO_2 nanoparticles were synthesised with a FSP reactor. Three different powders were realised using always a 5/5 flame, i.e. undoped SnO_2 (0.0 wt% Pt/SnO_2), 0.2 wt% Pt/SnO_2 and 2.0 wt% Pt/SnO_2. In all cases SnO_2 had a primary particle size of 10 nm. The powders were deposited via screen printing on standard substrates.

5.4.1 Low CO concentration range

Figure 51 shows the effect of the platinum functionalisation on the sensor signal for small concentrations of CO (5 – 50 ppm) at various temperatures in dry synthetic air. For all three sensors the highest signals are achieved at 300°C and are decreasing continuously with increasing temperature. Doping the SnO_2 with 0.2 wt% platinum results in a much steeper calibration curve and the highest sensor signals compared to pure SnO_2 (compare Figure 51 A and B). The higher sensor signal and especially the higher sensitivity (i.e. the steeper response curve) increase sensor performance. However, the situation is completely different when adding more platinum. Here, 2.0 wt% reduces the performance drastically and only at the highest concentration of 50 ppm and at the lowest temperature of 300°C does the sensor start to respond to CO. These tests were performed with a set of four sensors placed in a teflon-made chamber so that possible gas consumption effects have to be taken into consideration (see Chapter 5.4.3).
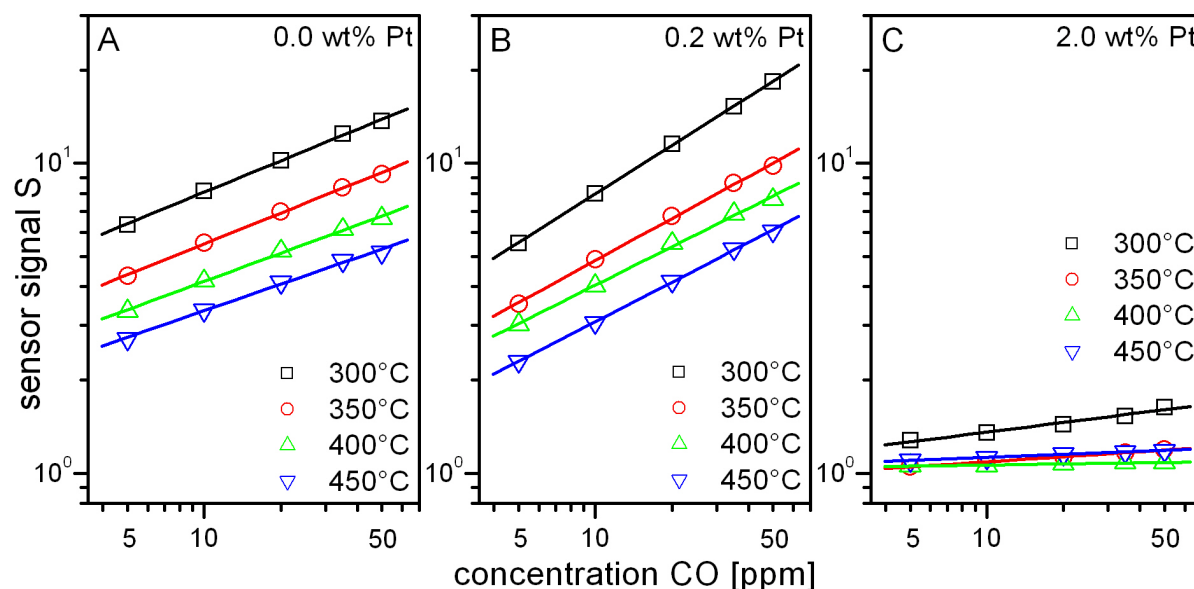
Figure 51:   Sensor signal S dependence on low CO concentration for undoped SnO_2 (A), 0.2 wt% Pt-doped SnO_2 (B) and 2.0 wt% Pt doped SnO_2 (C). The measurements are performed at various temperatures in dry synthetic air.

This is in agreement with the general findings on the influence of Pt doping on the CO sensing properties of SnO_2. Low concentrations of platinum increase the signals to CO whereas an increase in platinum concentration leads to a decrease in sensing properties. This was reported also for the sol-gel SnO_2 with 0.2 wt% and 2.0 wt% Pt [161, 163].

Similar findings were reported for pyrosol co-deposited Pt/SnO_2 (2.4 wt% Pt) [164]. In the wet phase method the 0.2 wt% Pt doping significantly increases the sensor signal to CO both in dry and especially in humid air, in contrast to 2.0 wt% Pt which decreases this property [78]. In both cases (for 0.2 wt% and 2.0 wt%) of the wet phase method Pt was found to be present in oxidised form (as Pt^{2+} or Pt^{4+}) and the formation of clusters or isolated metallic nanoparticles was not observed [84, 161]. In the aerosol pyrolysis method Pt is found to be present as Pt clusters either in a metallic or in an oxidised state on the surface of SnO_2 particles [162].

5.4.2 High CO concentration range

In order to investigate the strong effect that high platinum loading has on the sensing properties of the FSP generated SnO_2 materials, CO concentrations up to 1,000 ppm were delivered to the sensors. In order to eliminate consumption effects, each sensor was tested individually in a test chamber. Figure 52 shows the signals of the sensors for different CO concentrations in dry synthetic air and in synthetic air with 50% r.h. at an operating temperature of 400°C.
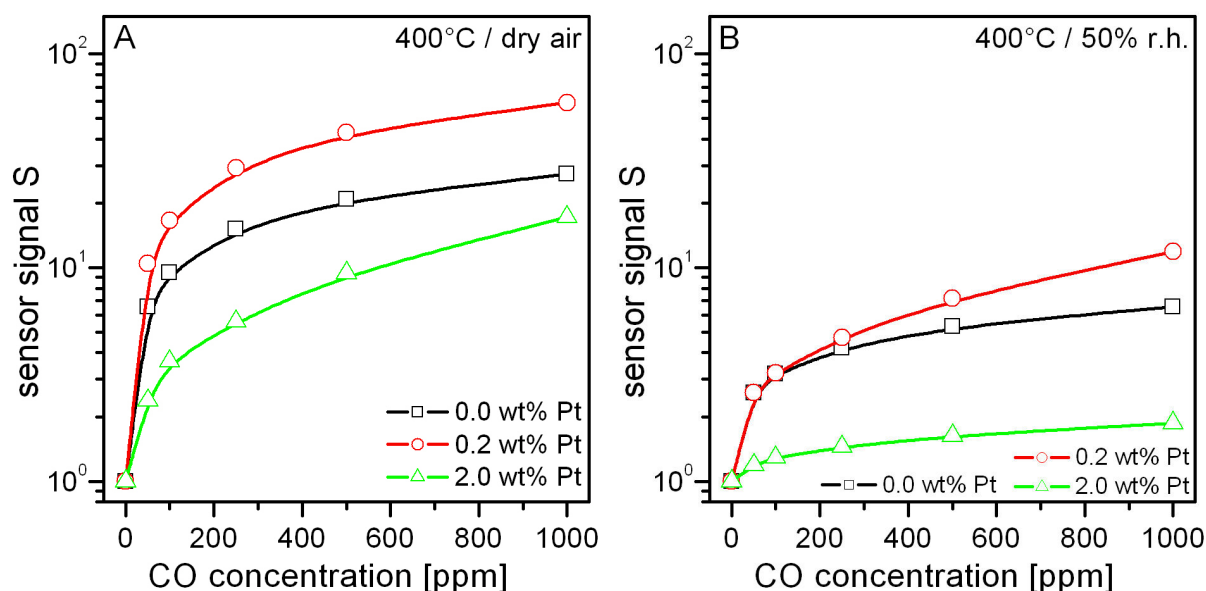
Figure 52: Sensor signal S dependence on high CO concentration for undoped SnO_2 (black squares), 0.2 wt% Pt-doped SnO_2 (dark grey circles) and 2.0 wt% Pt-doped SnO_2 (light grey triangles). The measurements are performed at 400°C in dry synthetic air (A) and in synthetic air with 50% r.h. (B).

In dry air the same tendency as for low CO concentrations was found, i.e. the 0.2 wt% Pt/SnO$_2$ sensor shows higher sensor signals than the undoped SnO$_2$ sensor and the 2.0 wt% Pt/SnO$_2$ sensor shows the lowest sensor signals. However, the sensor with 2.0 wt% platinum becomes more and more sensitive and the large difference in sensor signal is reduced at higher concentrations (Figure 52 A). In the presence of humidity the signals of all sensors are decreased with the 0.2 wt% Pt/SnO$_2$ sensor having still the best sensing performance (Figure 52 B). The dependence of the sensor signals on the CO concentration can be approximated by a power law dependency in all cases (Table 9).

Table 9: Calibration function $S = 1 + a \times c^x$ of the platinum functionalised sensors for CO (50 – 1,000 ppm) in dry synthetic air and in synthetic air with 50% r.h.

conditions	Calibration function for SnO$_2$ sensors functionalised with		
	0.0 wt% Pt	0.2 wt% Pt	2.0 wt% Pt
CO (dry air)	$S = 1 + 1.027 \times c^{0.480}$	$S = 1 + 1.118 \times c^{0.582}$	$S = 1 + 0.138 \times c^{0.642}$
CO (50% r.h.)	$S = 1 + 0.760 \times c^{0.311}$	$S = 1 + 0.331 \times c^{0.502}$	$S = 1 + 0.652 \times c^{0.149}$

As shown in Chapter 5.2.1 the reaction of CO with SnO$_2$ takes place via interaction with pre-adsorbed oxygen species. Bârsan et al showed that the type of reactive oxygen species that is involved in the reaction with CO determines the exponent of the calibration function [19]. Comparing the shape of the curves in Figure 52 and the values for the exponents in Table 9 indicates that the type of participating oxygen species changes with the doping content. Thus, the relative concentration of the different oxygen species on the surface depends on the presence and the amount of platinum.

5.4.3 Catalytic conversion measurements

The low signals of the sensors with high platinum loading (2.0 wt%) for CO may result from "localized" CO consumption at the platinum without electron transfer to the conduction band of SnO$_2$. In this case Pt acts as a "good catalyst" and catalytic oxidation of carbon monoxide takes place locally on platinum. In this case the charge transfer takes place only in a localized manner and has no direct impact on the electrical conduction of SnO$_2$.

Catalytic conversion measurements of the analyte gas are a good tool to investigate such questions. This is the case because each sensing process on its own – i.e. reaction of an analyte molecule at the surface of the sensor into one or more products – reduces the number of analyte molecules in the outgoing gas stream compared to the ingoing one. By measuring the composition of the outgoing gas stream and comparing it with the sensor signal one gets information about gas combustion at the different parts of the sensor. In the present case, the analyte gas containing a certain CO concentration was delivered first through a chamber with a single sensor (position #1) and afterwards through a chamber with seven sensors (sensors #2 to #5) in a row of always two sensors opposing each other (position #a and #b). The setup was chosen in this way because (i) a total number of eight sensors guarantees a measurable consumption of CO and formation of CO_2 and (ii) separating the first sensor from the others enables to obtain a sensor signal which is really due to the sensor response and not influenced by consumption effects.
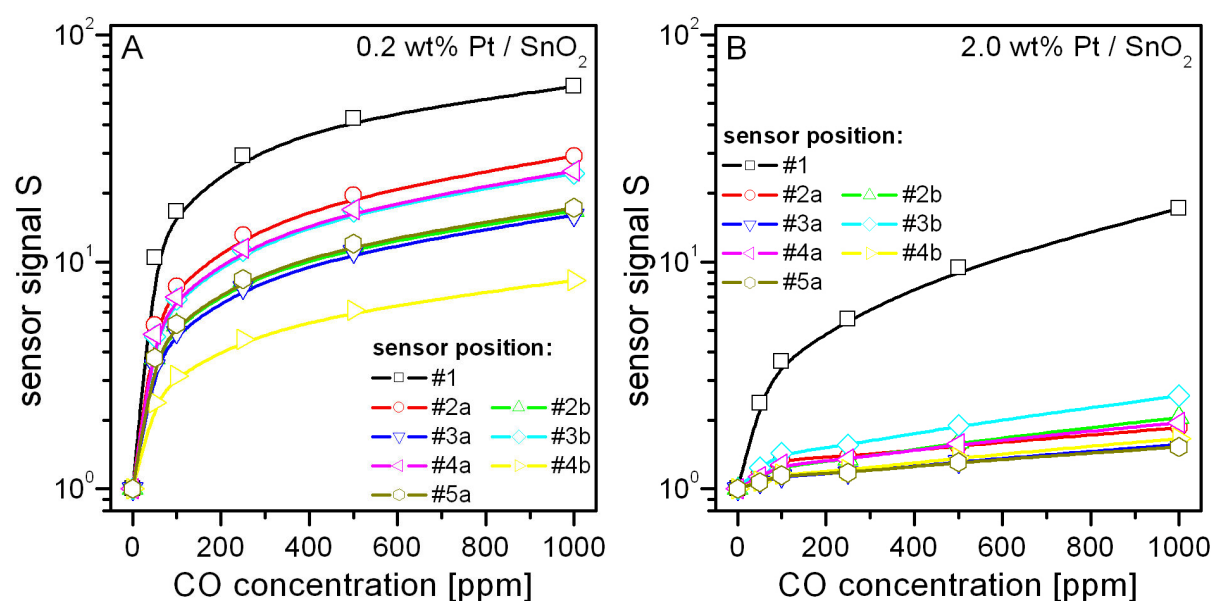
Figure 53: Sensor signal S of 0.2 wt% Pt/SnO_2 (A) and 2.0 wt% Pt/SnO_2 (B) sensors for different CO concentrations. In both cases two chambers are connected in series, the first one containing a single sensor (#1) and the second one containing seven sensors (#2a to #5a). The measurements are performed at 400°C in dry synthetic air.

Figure 53 shows the sensor signals of eight 0.2 wt% Pt-doped and eight 2.0 wt% Pt-doped SnO_2 sensors for various CO concentrations at 400°C in dry synthetic air. As already seen in previous experiments, the sensor with low platinum doping shows higher

signals than the sensor with high platinum doping (compare sensor #1 in Figure 53 A and B). For the 0.2 wt% Pt/SnO_2 sensors the sensor signal decreases subsequently in the direction of the gas flow. For the 2.0 wt% Pt/SnO_2 sensors only the first sensor in the single chamber (position #1) shows a significant sensor signal, whereas all seven sensors in the second chamber show almost no signal.

The decrease of the sensor signal in the second chamber is due to a consumption of CO by the sensors themselves and thus leading to a decrease in the effective CO concentration that is seen by the sensors along the flow direction. The drastic reduction of the sensor signal in the case of the 2.0 wt% Pt-doped sensors indicates a higher CO consumption on those sensors (compared to the 0.2 wt% Pt/SnO_2 ones). However, the fact that at the same time the sensor signal of the heavily doped sensor in position #1 is lower than the one of the less doped sensor indicates that the observed high conversion of CO does not take place at the surface of the SnO_2 (neither directly nor indirectly via the Pt dopant). To confirm the assumption of higher CO conversion, the outgoing gas composition was analysed with an IR gas analyser. Figure 54 shows the measured CO (educt of conversion) and CO_2 (product of conversion) concentrations in the final gas stream for several injected CO concentrations. One can clearly see that indeed the 2.0 wt% Pt-doped sensor converts more CO into CO_2 than the 0.2 wt% Pt-doped sensor, i.e. the CO concentration is lower whereas the CO_2 concentration is higher. The relative conversion of the 2.0 wt% Pt/SnO_2 sensor is 72.0%, whereas it is only 61.6% in the case of the 0.2 wt% Pt/SnO_2. Due to the non-linear behaviour of the sensors (a power law dependence on the CO concentration), the effect of this decrease in the actual CO concentration is a massive decrease in the sensor signal (as seen in Figure 53).
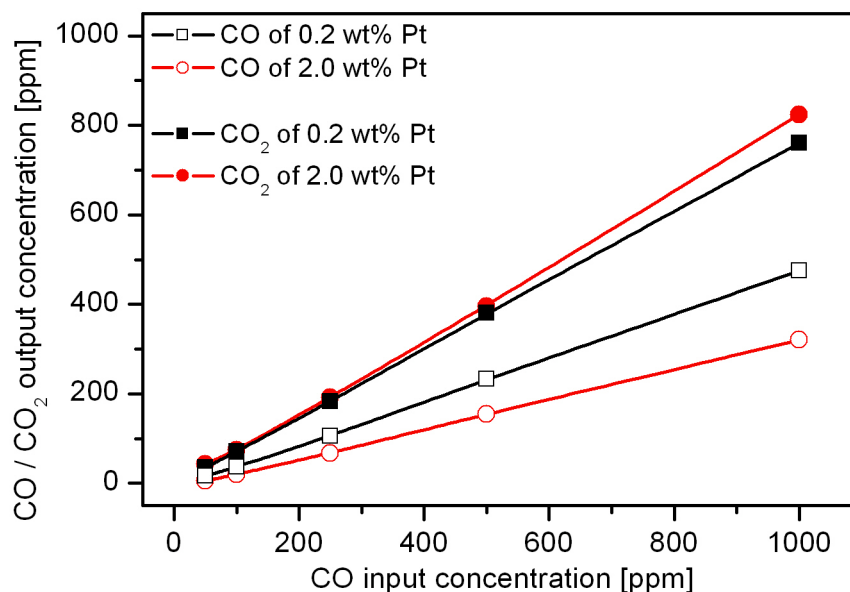
Figure 54: Catalytic conversion of CO by the 0.2 wt% Pt/SnO₂ sensor (black squares) and the 2.0 wt% Pt/SnO₂ sensor (grey circles). The outgoing CO concentration (open symbols) and CO₂ concentration (filled symbols) are measured for various CO concentrations at 400°C in dry synthetic air. The analyte gas is delivered through two chambers with altogether eight sensors.

As already mentioned in Chapter 4.1.2 higher platinum loading resulted in a lower dispersion of the platinum. Additionally, it has been shown for flame made metal oxides that a higher Pt content favours the reduction of the platinum leading to a larger amount of Pt^0 than materials with low platinum content [165]. Combining both findings makes a local conversion of CO at the platinum particles without charge transfer to or from the conduction band of the SnO_2 grains very much probable for the 2.0 wt% Pt-doped SnO_2.

5.4.4 Stability tests

The previous chapter demonstrated that the appropriate doping of SnO_2 with the FSP approach can help to optimise the performance of the fabricated sensors. In this context, "performance" was related to the sensor signal. Another very important feature of a metal oxide gas sensor is the long term stability. Actually, the drift of the sensors is one of the main difficulties for the application of MOX based sensors. Therefore, it was studied how sensors fabricated with FSP generated nanoparticles behave over a longer period of time and if the stability of the latter is influenced by *in situ* functionalisation with platinum.

The sensors were tested for 20 days with exposure to three different CO concentrations (10 ppm, 240 ppm and 50 ppm) every second day (see Figure 55). For these measurements one undoped SnO_2 and one 0.2 wt% Pt-doped SnO_2 sensor were placed together in one chamber facing each other.
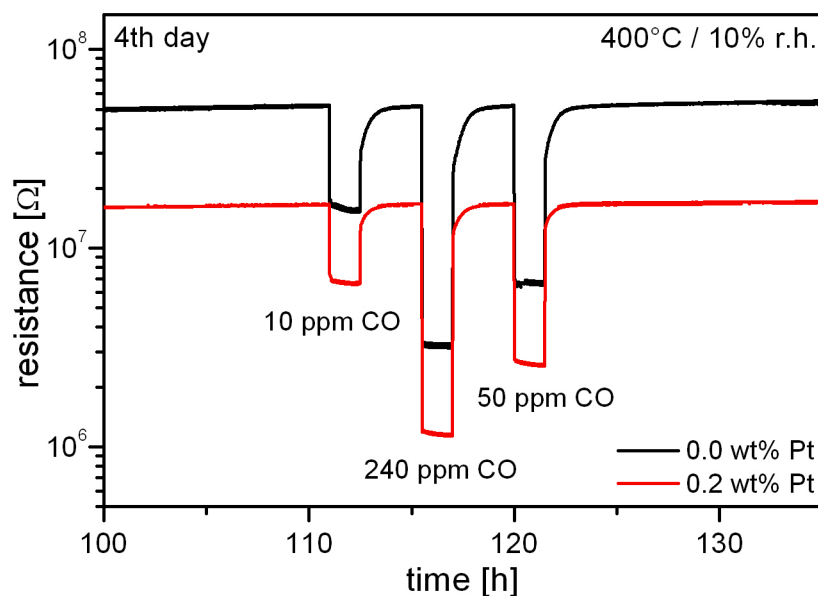
Figure 55: Measurement run for stability tests. The 0.0 wt% Pt/SnO_2 (black) and the 0.2 wt% Pt/SnO_2 (grey) sensor are exposed every second day to three different CO concentrations for a period of twenty days. The measurement is performed at 400°C and in synthetic air with 10% r.h. The figure shows one exposure cycle on the fourth day.

Figure 56 shows the calculated sensor signals for the three CO concentrations over 20 days for the undoped sensor (Figure 56 A) and the 0.2 wt% Pt-doped sensor (Figure 56 B). The signals for both sensors are quite stable over time and show only little drift, whereas the stability of the doped one seems to be a little bit better. The reason for the observed drift becomes more obvious when looking at the evolution of the resistance over the time for the sensors.
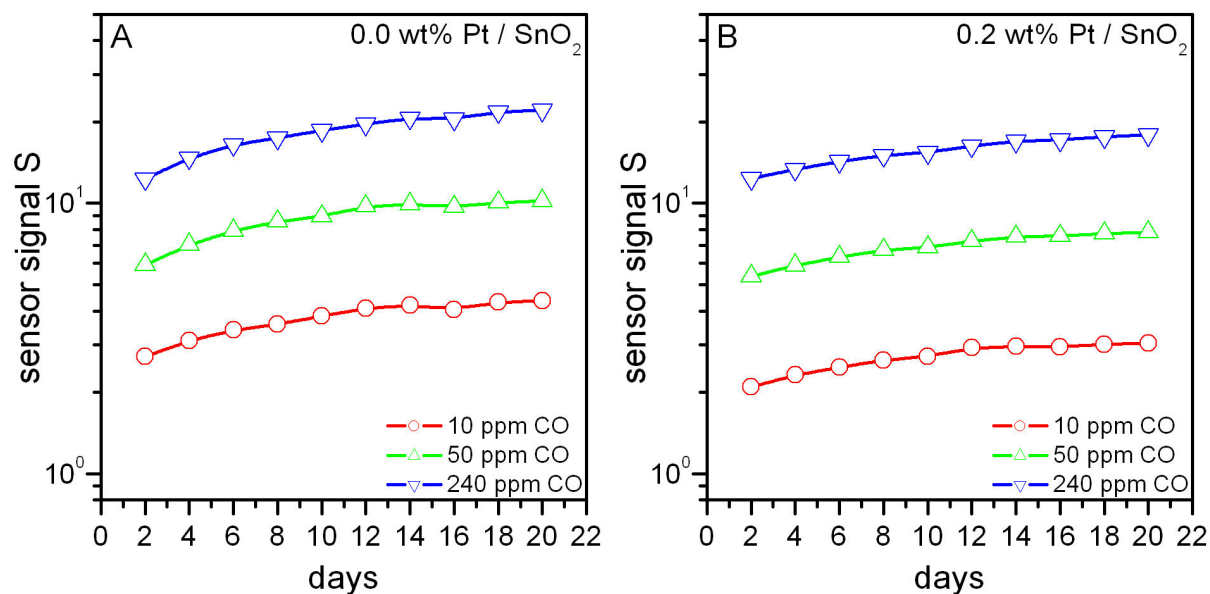
Figure 56: Sensor signal S of the 0.0 wt% Pt/SnO$_2$ (A) and the 0.2 wt% Pt/SnO$_2$ (B) sensor for three different CO concentrations over 20 days. The measurement is performed at 400°C in synthetic air with 10 % r.h.

Figure 57 reveals that most of the drift is due to a slight drift in the base resistance of the sensors in air, i.e. in the absence of CO. This effect is emphasised even more for the undoped material (compare black squares in Figure 57 A and B). Furthermore, in the presence of CO practically no drift could be observed for the Pt-doped material. This indicates that the presence of platinum stabilises the situation at the surface of the SnO$_2$ as the adsorption / desorption equilibrium of the analytes is reached faster due to the catalytic behaviour of the noble metal. Thus, the stability of the 0.2 wt% Pt-doped SnO$_2$ sensor is better than of the undoped SnO$_2$. However, the quality of both FSP fabricated sensors is quite high compared to others. For example, sensors from sol-gel prepared powders showed a steady drift of a factor of 1.6 over the same timescale (20 days) [78].
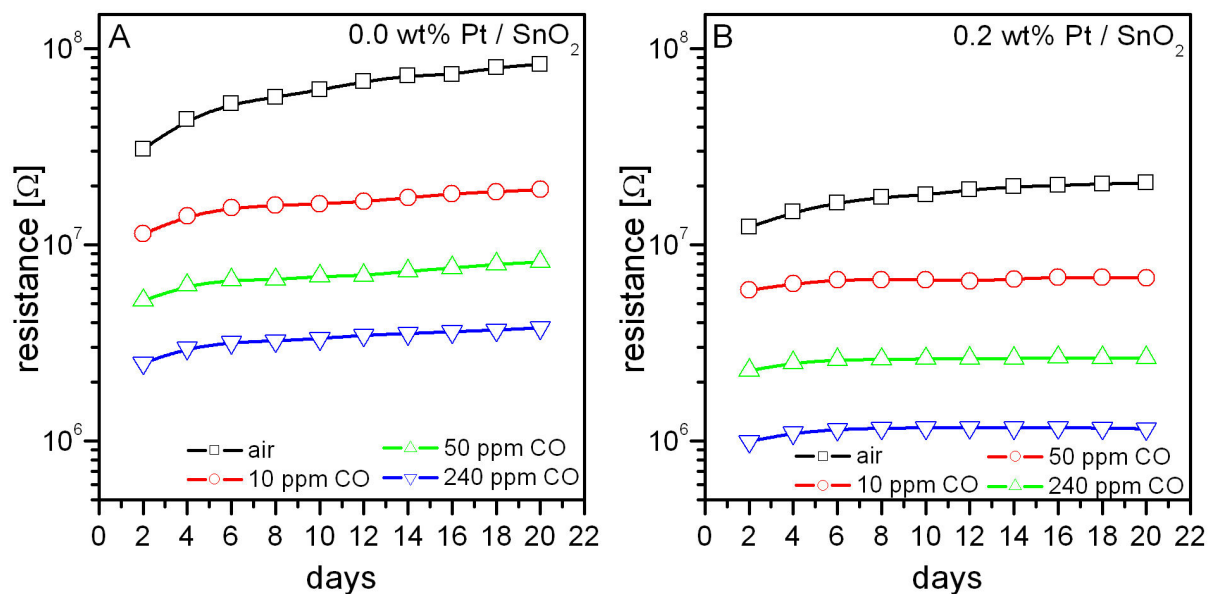
Figure 57: Resistance of the 0.0 wt% Pt/SnO₂ (A) and the 0.2 wt% Pt/SnO₂ (B) sensor in air and for three different CO concentrations over 20 days. The measurement is performed at 400°C in synthetic air with 10% r.h.

5.4.5 Summary

The *in situ* functionalisation of SnO₂ nanoparticles with platinum was realised successfully in a single-step process using the FSP method. Sensors with thus prepared powders were tested for their CO sensing behaviour.

Low platinum loadings (0.2 wt% Pt) led to sensors with higher sensor signals and steeper calibration curves in the low concentration range (5 – 50 ppm CO) as well as in the high concentration range (50 – 1,000 ppm CO) compared to undoped SnO₂. However, in the case of high platinum loadings (2.0 wt% Pt) the sensor signal decreased dramatically. Catalytic conversion measurements revealed that this effect is due to an increased reaction of CO at the platinum without direct or indirect interaction with the SnO₂: The CO conversion was found to be higher for the 2.0 wt% Pt/SnO₂ sensor than for the 0.2 wt% Pt/SnO₂ sensor. The stability of the prepared sensors (undoped SnO₂ and 0.2 wt% Pt/SnO₂) was very high over an examined period of 20 days, especially with regard to other sensors reported in literature.

In summary, using FSP to synthesize functionalised metal oxide nanoparticles for gas sensing applications allows for the fabrication of optimised and improved sensors.

5.5 Grain size effect

5.5.1 Influence on CO sensing

It has been shown in Chapter 4.1 that FSP is a very smart method to tune the grain size of the fabricated metal oxide. In this chapter the effect of varying the grain size on the gas sensing properties was examined. Therefore, undoped SnO_2 powder with three different grain sizes was prepared using different ratios of precursor feed rate and oxygen flow rate (Table 10). With these powders sensors were prepared by means of screen printing on alumina substrates.

Table 10:   Parameters of the FSP reactor for SnO_2 powder with different grain sizes.

sensor	feed rate of syringe pump	flow of oxygen	grain size
SnO_2 3/7	3 ml/min	7 l/min	5.5 nm
SnO_2 5/5	5 ml/min	5 l/min	10 nm
SnO_2 8/3	8 ml/min	3 l/min	17 nm
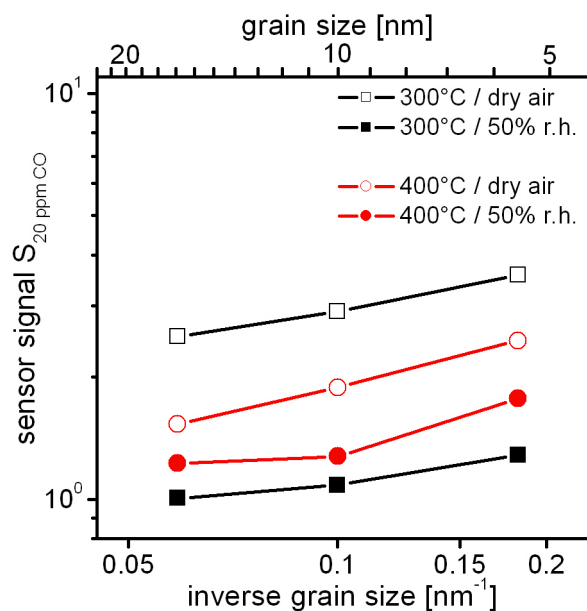
Figure 58:   Sensor signal S of the SnO_2 3/7, SnO_2 5/5 and SnO_2 8/3 sensors for 20 ppm CO. The sensor signal is plotted against the inverse grain size. The measurements are performed at 300°C (black squares) and 400°C (grey circles) in dry synthetic air (open symbols) and in synthetic air with 50% r.h. (filled symbols). For the sake of clarity, the grain size is given at the top scale bar.

The signals of the SnO_2 sensors with 5.5 nm, 10 nm and 17 nm grain size for 20 ppm CO were recorded at two different temperatures (300°C and 400°C) in dry synthetic air and in synthetic air with 50% r.h. Figure 58 plots the obtained signals versus the inverse grain size (additionally, the grain size itself can be seen at the top of the figure).

It can be seen that in all cases the sensor signal increases with decreasing grain size. This phenomenon has been reported many times in the past [166, 167, 168, 132]. However, the present results show only a slight increase with decreasing grains whereas for comparable grain sizes a steep increase is described [166, 167]. A model that is based on grain boundaries, necks between grains and totally depleted grains explains this strong increase of the sensor signal [166]. It is stated that the sensor signal depends strongly on the relation between the diameter of the grains (D) and the size of the depletion layer (L). As long as D is much larger than 2L, the transduction process is dominated by grain boundaries and results in a slight increase of the sensor signal with decreasing grain size. When the grain diameter gets close to 2L the sensor signal increases strongly because in this case all the electrons are captured at the surface and thus changes in the surface charge carrier concentration lead to strong changes in the overall resistance. Most papers report this strong increase in sensor signal for a grain size of 5 – 10 nm. As a consequence of the above described model, for the FSP generated powder the critical value of D = 2L is not reached yet even for the SnO_2 3/7 (5.5 nm). Rather, the transduction process is still dominated by grain boundaries. A similar correlation between sensor signal and grain size in the same grain size region has been reported for SnO_2 and ethanol [132].

5.5.2 Summary

It has been shown that FSP generated nanoparticles show different sensing properties depending on the grain size, i.e. the sensor signal increases with decreasing grain size. However, even in the case of the smallest particles (5.5 nm) the grains were not fully depleted and thus the charge carrier transport is still dominated by the grain boundaries.

5.6 Layer thickness dependency

The flexibility of the FSP process using the direct deposition of nanoparticles on sensor substrates offers a straightforward possibility of tuning and adjusting the thickness of the deposited layers by varying the deposition time (see Chapter 2.7 and 4.2.1). The deposition time had no influence on the porosity of the layers, the grain size and the chemical state of additional dopants. For the present investigation, the fabrication of four sensors at once has been tested using (i) 0.0 wt% Pt/SnO_2 and (ii) 0.2 wt% Pt/SnO_2. Therefore, these sensors give additional information about the reproducibility of the FSP direct deposition method. Both materials undoped and Pt-doped SnO_2 were deposited using three different deposition times, respectively (i.e. 30 s, 180 s and 360 s). Table 6 in Chapter 4.2.1 reveals that the resulting layers had a layer thickness of 9 µm, 30 µm and 40 µm.

5.6.1 Reproducibility

The reproducibility of the sensors was calculated according to Equation 11 for the four 0.0 wt% Pt/SnO_2 sensors and the four 0.2 wt% Pt/SnO_2 sensors with 180 s deposition time. Table 11 lists the reproducibility for dry air and 50 ppm CO in dry air at 400°C. Both types of sensors show a good reproducibility, whereas it is improved by platinum functionalisation.

Table 11: Reproducibility (%) of four sensors simultaneously deposited (deposition time: 180 s). The calculations are performed for 0.0 wt% Pt and 0.2 wt% Pt-doped SnO_2 sensors in dry synthetic air and in 50 ppm CO in dry synthetic air.

sensor	reproducibility in	
	dry air	50 ppm CO
0.0 wt% Pt/SnO_2	77.3%	85.2%
0.2 wt% Pt/SnO_2	83.4%	87.9%

The similarity of sensors simultaneously deposited within one production batch can also be seen from Figure 59 A where the mean sensor signal and its standard deviation is given

for the undoped and the 0.2 wt% Pt-doped sensors. The different materials also show a similar sensing behaviour represented by similar calibration curves: $S = 1 + 1.488 \times c^{0.378}$ for 0.0 wt% Pt/SnO$_2$ and $S = 1 + 1.472 \times c^{0.413}$ for 0.2 wt% Pt/SnO$_2$.
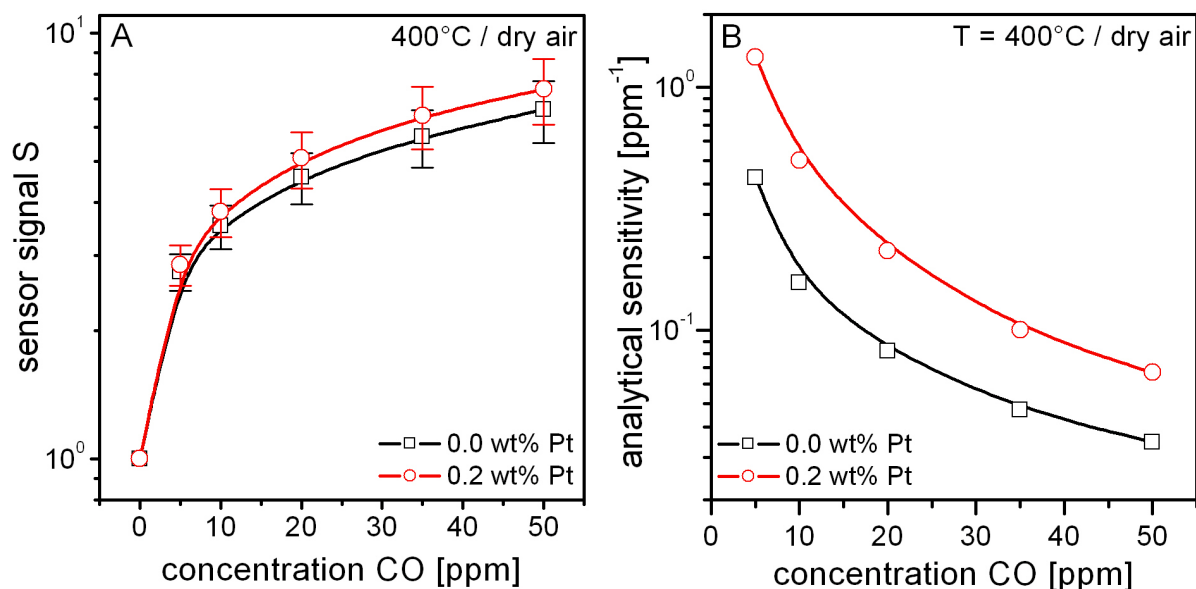
Figure 59: Sensor signal S dependency of the 0.0 wt% Pt/SnO$_2$ (black squares) and the 0.2 wt% Pt/SnO$_2$ (grey circles) for various CO concentrations given as the mean value of the sensor signal and its standard deviation (A). Analytical sensitivity of the 0.0 wt% Pt/SnO$_2$ (black squares) and the 0.2 wt% Pt/SnO$_2$ (grey circles) (B). The measurements are performed at 400°C in dry synthetic air.

Figure 59 B shows the analytical sensitivity for the undoped and the Pt-doped sensors which were calculated from the standard deviation (Equation 13). For example, the analytical sensitivity to 50 ppm CO is 0.034 ppm^{-1} for the 0.0 wt% Pt/SnO$_2$ sensors and 0.067 ppm^{-1} for the 0.2 wt% Pt/SnO$_2$ sensors. Therefore, the two different kind of sensors allow the detection of 50 ppm CO with a precision of 29 ppm and 15 ppm, respectively.

5.6.2 Undoped SnO$_2$

The resistance of the 0.0 wt% Pt/SnO$_2$ sensors with three different layer thicknesses was measured at 400°C in dry air, in dry air with 50 ppm CO and in dry air with 10 ppm ethanol. Figure 60 shows the resistance values (left axis) and the sensor signals calculated on the basis of these values.
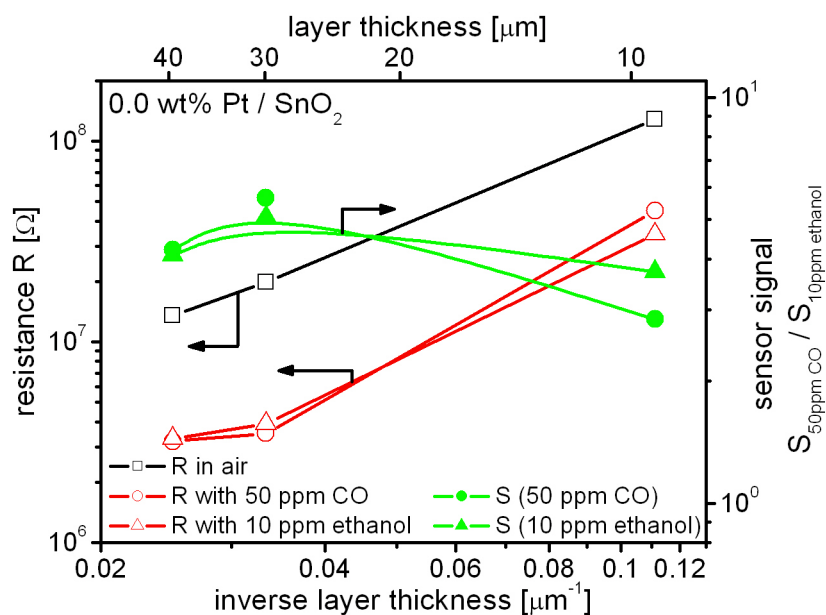
Figure 60: Influence of layer thickness for the 0.0 wt% Pt/SnO₂ sensor. The resistance (open symbols) is recorded in dry synthetic air (black squares), in dry synthetic air with 50 ppm CO (dark grey circles) and in dry synthetic air with 10 ppm ethanol (dark grey triangles) at 400°C. The sensor signal is calculated for 50 ppm CO (light grey circles) and for 10 ppm ethanol (light grey triangles). Resistance values and sensor signals are plotted versus the inverse layer thickness. For the sake of clarity, the layer thickness is given at the top scale bar.

It can be clearly seen that the overall resistance decreases with longer deposition times and therefore with thicker layers. Especially in air, the resistance has an inverse dependence on the layer thickness. The influence of the layer thickness on the characteristics of a MOX based sensor is described by different models in literature. To summarise, the main models to explain the layer thickness effects are (i) a simple geometric theory [169], (ii) a diffusion theory of the analyte into the pores of the metal oxide [170, 171, 172] and (iii) a theory of space charge effects at the three boundary point gas/metal oxide/metal electrodes [19, 173].

In the geometric model the resistance R of the sensing layer depends on the resistivity of the sensing material ρ_{SC}, and the geometric parameters of the layer, i.e. the length L, the thickness s_{sl} and the width w (Equation 25):

$$R = \rho_{SC} \cdot \frac{L}{s_{sl} \cdot w} \qquad (25)$$

This relation displays very well the observed inverse layer thickness dependence of the resistance in dry air. However, the simple geometric model does not predict the sensor signal correctly. The sensor signal is defined as the ratio of resistance without and with analyte ($S = R_{air}/R_{gas}$). As the geometric parameters in Equation 25 do not change with gas adsorption, they are cancelled if calculating the ratio and the sensor signal would be independent of the layer thickness. This contradicts the observed results.

Therefore, the diffusion theory takes into account that the analyte molecules have to diffuse into the pores of the sensing layer. The consequence will be a concentration gradient along the penetration depth inside the layer. The relative penetration depth will be larger for smaller layer thicknesses. As the resistance is a measure over the whole layer, one can expect an increase in the sensor signal ($S = R_{air}/R_{gas}$) with decreasing layer thickness. However, the present study showed a maximum for the sensor signal for CO and for ethanol (Figure 60). This "anomalous" dependence that the sensor signal goes through a maximum with increasing layer thickness was found for CO also by others [173, 174].

This effect is explained by the electrode theory [173]. It has been shown that the sensing reaction depends on many factors, one of them being the material and the geometry of the electrodes [19]. In the case of CO detection with SnO_2 the sensing activity is not equal through the whole layer; it rather takes place at the bottom of the SnO_2 layer [169]. This can be attributed to the effect of the metal electrodes. The electrode theory suggests that at the three boundary point gas/metal oxide/metal electrode adsorbed oxygen species are accumulated and thus depleted regions in the metal oxide in the vicinity of the electrodes are created. These depleted regions have their 3-dimensional continuation also into the layer of the metal oxide for a certain effective reach. Simulations of the overall resistance for different layer thicknesses showed that the assumption of the electrode theory lead to a maximum in the sensor signal for a certain layer thickness. The actual dependency relies on various factors, amongst them temperature and the nature and concentration of the analyte. Thus, the observed results for the sensor signal of 50 ppm CO and 10 ppm ethanol for the undoped SnO_2 sensor are in agreement with the described model.

5.6.3 Pt-doped SnO$_2$

In the case of the 0.2 wt% Pt-doped SnO$_2$ sensor a similar behaviour for the sensor signal is obtained for CO sensing, i.e. a maximum for 30 µm layer thickness appears (see Figure 61). However, for ethanol the situation is completely different. Here, the sensor signal increases continuously with decreasing layer thickness.
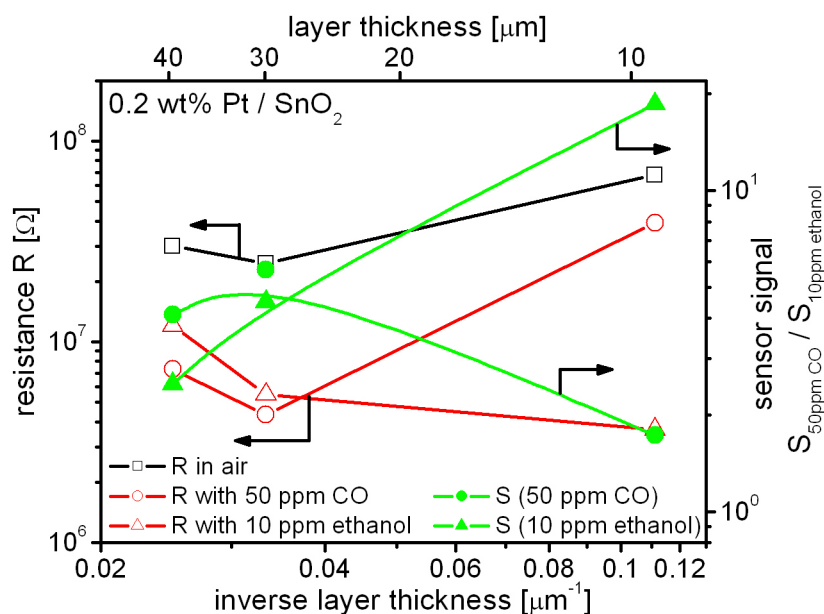
Figure 61: Influence of layer thickness for the 0.2 wt% Pt/SnO$_2$ sensor. The resistance (open symbols) is recorded in dry synthetic air (black squares), in dry synthetic air with 50 ppm CO (dark grey circles) and in dry synthetic air with 10 ppm ethanol (dark grey triangles) at 400°C. The sensor signal is calculated for 50 ppm CO (light grey circles) and for 10 ppm ethanol (light grey triangles). Resistance values and sensor signals are plotted versus the inverse layer thickness. For the sake of clarity, the layer thickness is given at the top scale bar.

Bearing in mind that the results for the undoped SnO$_2$ were explained by the effects of the three boundary point gas/metal oxide/metal electrode, platinum loading in the case of 0.2 wt% Pt/SnO$_2$ sensors introduces an additional three boundary point gas/metal oxide/noble metal. The latter are not limited to the bottom of the layer but are present throughout the whole sensing layer. Thus, the thickness dependent effects of the electrodes are superposed by the catalytic effects of the dopant which are assumed to be less position dependent. As a result, diffusion controlled effects become more important, leading to a decreased sensor signal with increasing layer thickness.

5.6.4 Summary

Simultaneously fabricated sensors by FSP direct deposition (undoped as well as *in situ* platinum functionalised SnO_2) showed high reproducibility for CO detection. This is a very important feature for commercial sensor production and practical applications. These sensors were realised with different layer thicknesses between 9 μm and 40 μm.

The performance of the gas sensors was found to depend on the layer thickness. Different models were applied to explain the observed behaviour. In this context, the important role of the electrodes at the bottom of the sensing layer as well as of noble metal dopants dispersed throughout the layer was pointed out. Thus, thickness effects on the gas sensing can be explained taking into account gas diffusion and chemical contribution of electrodes and dopants. Generally, variation of the layer thickness allows tuning the sensor performance. Hence the FSP technique allows for an easy layer thickness control, it is highly recommended for gas sensor fabrication.

5.7 Multilayer sensors

The FSP setup was used to synthesise and directly deposit multilayers of metal oxides on sensor substrates. The advantage of this approach is to use different materials with different properties towards the gases to be detected. In the present study, multilayer sensors were fabricated consisting of a sensing layer (undoped or Pd-doped SnO_2) and a catalytic filter layer (Pd-doped Al_2O_3) on top of it. The potential of multilayer sensors with a sensing layer and a filter layer on top has been reported in the past [113, 114, 119]. However, the integration of the latter into a single-step fabrication process is a unique and new achievement. The sensing behaviour of thus fabricated sensors was investigated by means of dc electrical measurements and catalytic conversion measurements. The alumina filter layer always contained 1.4 wt% palladium, the SnO_2 was undoped or with 1.4 wt% palladium. To investigate the effect of the filter, the corresponding single layer (undoped or Pd-doped SnO_2) counterparts were fabricated as well. Additionally, a single layer SnO_2 sensor with 0.07 wt% Pd was used to study the effect of Pd loading.

5.7.1 Dc electrical characterisation

All sensors were tested for methane (CH₄), CO and ethanol. The measurements were carried out at temperatures between 200°C and 400°C. Figure 62 shows the sensor signals of all sensors for 230 ppm CH₄, 240 ppm CO and 50 ppm ethanol at various temperatures in dry synthetic air.
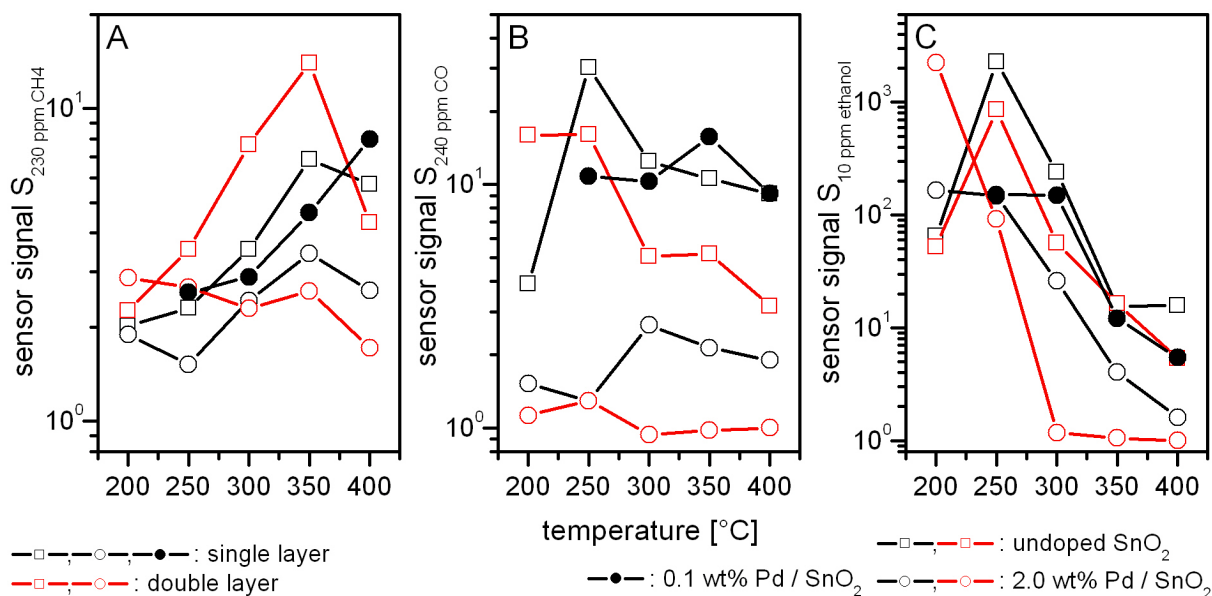
Figure 62: Temperature dependence of the sensor signal for different undoped SnO₂ (open squares), 1.4 wt% Pd-doped SnO₂ (open circles) and 0.07 wt% Pd-doped SnO₂ (filled circles) sensors. Single layer sensors (black) and double layer sensors (grey) are tested for 230 ppm CH₄ (A), 240 ppm CO (B) and 50 ppm ethanol (C) in dry synthetic air.

Effect of doping SnO₂

The surface functionalisation of the SnO₂ with 1.4 wt% Pd leads to a decrease in sensor signal for all three investigated gases (compare black open squares and black open circles in Figure 62). This might be due to the relatively high loading with Pd, as a similar behaviour was found in Chapter 5.4 for platinum doping. In the previous case, this effect was explained by a direct catalysis on the noble metal clusters at higher Pt loadings. Accordingly, in the case of Pt-doping the 0.2 wt% Pt increased the sensor signal for CO, whereas 2.0 wt% led to a strong decrease. By contrast, low Pd-doping only increases the sensor signal in very few cases (for CH₄ at 400°C and for CO at 350°C, see Figure 62 A

and B) but mostly leads to a decrease compared to the undoped sensor. Therefore, one can assume that for Pd even low dopant loadings cause a direct reaction of the analytes at the palladium clusters without interaction with the SnO_2 surface.

Effect of Pd/Al$_2$O$_3$ filter on undoped SnO$_2$

The presence of a Pd-doped Al_2O_3 filter on top of the undoped SnO_2 layer increases the sensor signal for CH_4 (Figure 62 A). This sensitisation effect cannot be explained by the performance of a "classical" filter, i.e. the number of active molecules in the sensing layer is reduced by the presence of a filter layer either physically or chemically. Rather, the methane reaction at the SnO_2 grains is activated by the filter layer (see also Chapter 2.6). The initial step in the oxidation of CH_4 is the abstraction of an H radical [75, 76, 175]. The energy needed for this reaction might be lowered by the interaction with the Pd/Al_2O_3 layer. Pd based catalysts are known to be the most effective for the complete conversion of methane [176]. This would increase the sensing reaction in the vicinity of the Pd/Al_2O_3-SnO_2 interface.

However, for CO and for ethanol the sensor signal decreases in the presence of the Pd/Al_2O_3 filter (Figure 62 B and C). Two possible explanations are the following. Either both CO and ethanol are partially converted into CO_2 already within the Pd/Al_2O_3 layer so that less CO and ethanol molecules reach the sensing layer and thus smaller sensor signals are achieved. Or the concentration of pre-adsorbed oxygen species in the SnO_2 layer is decreased by the filter layer. Catalytic conversion measurements might deliver insight into the detailed mechanisms (see Chapter 5.7.3).

Effect of Pd/Al$_2$O$_3$ filter on Pd-doped SnO$_2$

The influence of the Pd/Al_2O_3 filter on the sensing properties of Pd/SnO_2 depends on the temperature. For CH_4, the filter increases the sensor signal at temperatures below 300°C, whereas it decreases the latter at temperatures above 300°C (Figure 62 A). Two competing effects might occur at the same time, i.e. the activation of the initial reaction step by the Pd/Al_2O_3 layer (as described above) and the total conversion to CO_2

throughout the Pd/Al_2O_3 layer. The activation process should be most effective at the interface between filter layer and sensing layer and the conversion of CH_4 by the filter should take place mostly within the filter layer. As the filter layer on top of the Pd-doped SnO_2 is much thicker than on top of the undoped SnO_2, these conversion effects are more visible for the Pd-doped SnO_2 sensor.

For CO and ethanol, at 300°C and above the presence of the Pd/Al_2O_3 layer inhibits the sensing reaction completely (Figure 62 B and C), i.e. no change in the resistance was observed. It is most likely that almost all analyte molecules already react within the filter layer at these temperatures and the analyte does not reach the sensing layer. However, at 200°C the sensor signal for ethanol is strongly increased by the filter. Again, the initial activation of the reaction might be strongly promoted in the filter layer at lower temperatures.

5.7.2 Catalytic conversion measurements

The reactions of the analyte within the different layers of the sensors were studied with catalytic conversion measurements. Downstream of the measurement chamber, an IR gas analyzer was employed to analyze the composition of the outgoing gas. Only CO_2 was found as reaction product for all analytes. On the basis of the measured CO_2 concentrations and the CH_4, CO and ethanol concentrations in the downstream gas, the percentage of the conversion was calculated. In order to get information about the influence of the entire setup (measurement chamber, blank substrates, gas connections etc.) measurements under identical conditions were performed using substrates without a sensing layer.
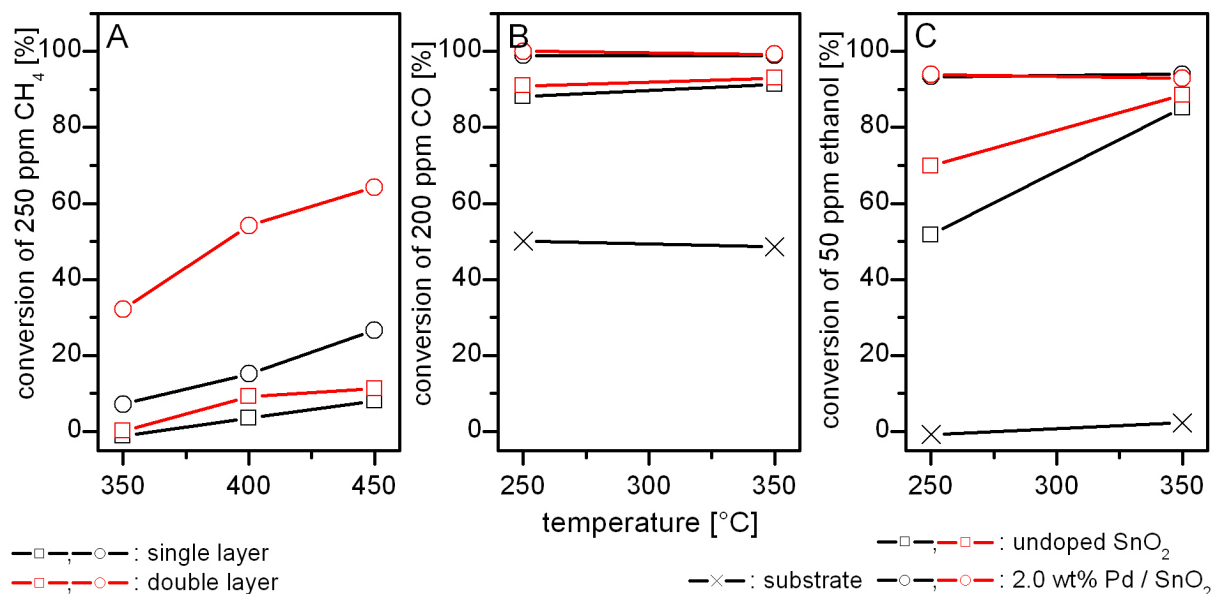
Figure 63: Catalytic conversion for different undoped SnO_2 (open squares) and 1.4 wt% Pd-doped SnO_2 (open circles). Single layer sensors (black) and double layer sensors (grey) are tested for 250 ppm CH_4 (A), 200 ppm CO (B) and 50 ppm ethanol (C) in dry synthetic air.

The results of these measurements are shown in Figure 63 and can be categorized as follows: (i) Doping the SnO_2 with palladium increases the conversion to CO_2 for all three gases. The associated decrease in sensor signal under these conditions indicates that the analyte molecules prefer to react directly at the Pd surface. This pathway inhibits reactions with the SnO_2 grains and therefore does not change the concentration of the free charge carriers resulting in an unaffected resistance of the sensing layer. (ii) The presence of the Pd/Al_2O_3 filter on undoped SnO_2 increases the conversion of CO and ethanol (Figure 63 B and C). This supports the assumption (see also Chapter 5.7.1) that lower sensor signals are due to a conversion of CO and ethanol within the filter layer. (iii) The addition of the Pd/Al_2O_3 filter layer on top of Pd-doped SnO_2 leads to a remarkable increase in conversion of CH_4 (Figure 63 A), which corresponds to lower sensor signals at these temperatures (see also Figure 62). However, the total conversion of methane is rather low compared to CO and ethanol which is in agreement with the higher sensor signals compared to CO and ethanol. (iv) The conversion of CO and ethanol is almost complete for both the Pd/SnO_2 and the Pd/SnO_2 + Pd/Al_2O_3 sensor (Figure 63 B and C). The conversion of CO to CO_2 takes place in either of these layers. Therefore, in the presence of the Pd/Al_2O_3 filter the sensor shows a sensor signal of 1 (i.e. no sensing reaction takes places).

5.7.3 Filter effect on selectivity

The influence of the operating temperature for different gases was investigated for each sensor in Chapter 5.7.1. Figure 64 shows a selection of these data for two different temperatures. At 250°C the Pd/SnO$_2$ sensor exhibits high sensor signals for ethanol and only small sensor signals for CO and CH$_4$. This results in a high selectivity for ethanol at this temperature. Increasing the temperature to 350°C improves the sensor signals for CH$_4$ for all sensors (see Figure 62). The multilayer sensor with a Pd/SnO$_2$ sensing layer and the Pd/Al$_2$O$_3$ filter shows a lower sensor signal compared to the undoped one (see Figure 62). However, this sensor shows a remarkable performance for methane sensing, because it does not respond to CO and ethanol at all and therefore has a formidable selectivity for CH$_4$ (Figure 64 B).
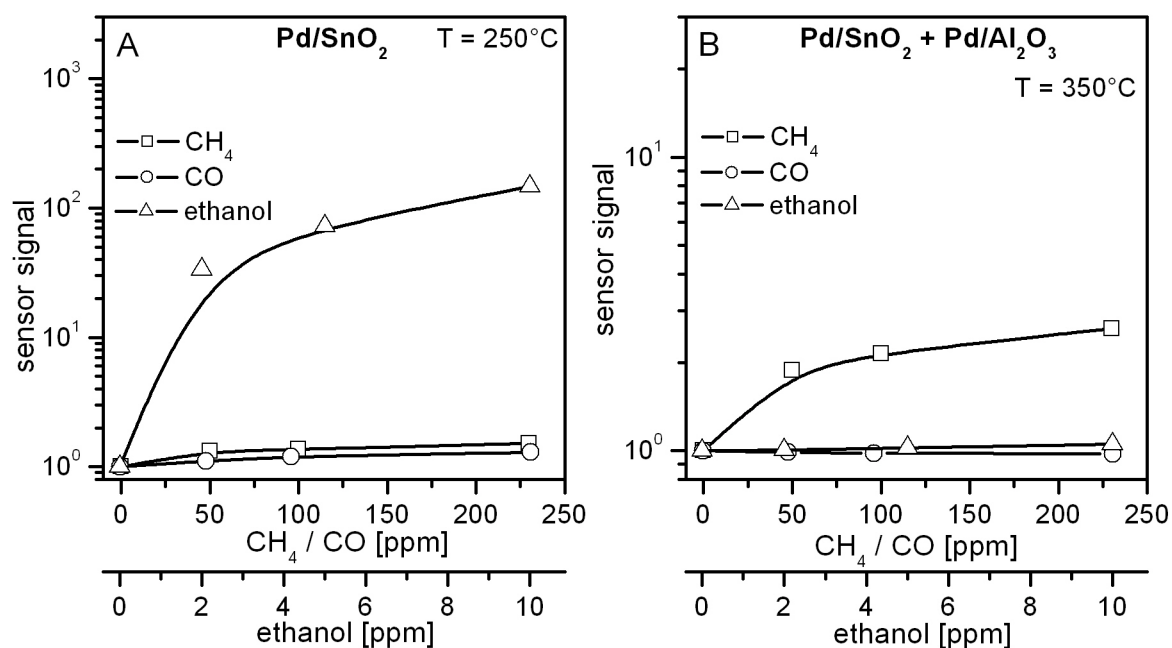
Figure 64: Sensor signal for methane (squares), CO (circles) and ethanol (triangles). The measurements with the Pd-doped SnO$_2$ single layer sensor are performed in dry synthetic air at 250°C (A). The measurements with the Pd-doped SnO$_2$ + Pd-doped Al$_2$O$_3$ double layer sensor are performed in dry synthetic air at 350°C (B).

5.7.4 Summary

The realised multilayer sensors with undoped and Pd-doped SnO_2 were characterised and compared with their single layer counterparts. It revealed that doping the SnO_2 with palladium decreases the sensor signals even for low Pd contents. This contradicts the findings of the Pt-doped sensors. Additionally, catalytic conversion measurements showed that Pd increases the formation of CO_2.

The presence of a Pd/Al_2O_3 filter on top of the sensing layer influenced the sensing behaviour for all three gases. Especially the combination of Pd-doped SnO_2 and Pd-doped Al_2O_3 allowed for achieving a very high selectivity for methane compared to CO and ethanol. Thus, by choosing appropriate filters and sensing conditions (e.g. temperature) the FSP method for multilayer sensor fabrication is a powerful tool and novel approach to specifically tune the performance of MOX based gas sensors.

6

Summary & outlook

6.1 Summary

The main achievements of this thesis are related to the development of a novel sensor fabrication technology and – with a strong focus put on – the implementation of its use for gas sensing applications. To achieve this, a strategy was followed that links the research activities with the strong restrictions of industrial implementation. The two main guidelines along this way were *investigation* and *benchmarking*. Thus, putting a lot of effort in research activity that is finally of no practical use can be avoided.

6.1.1 Investigation

A standard production technology for metal oxide nanoparticles mainly used in catalysis, the so called flame spray pyrolysis (FSP), was adopted stepwise for gas sensor fabrication. The final achievement is a fast and clean single-step process to fabricate fully functionalised multilayer sensors. This is a substantial progress as it merges the two fundamental processes of producing the sensing material and fabricating the sensing element into one step.

It was successfully demonstrated that different grain sizes between 5.5 nm and 19 nm with a narrow size distribution can be adjusted by the FSP reactor and that these grain sizes are not influenced by the deposition process, i.e. no agglomeration of particles occurs. As the sensors with different grain sizes show different sensing properties, FSP ensures the choice of optimum sensor performance. Furthermore, the functionalisation of the metal oxide with different noble metals in different amounts has crucial influence on the sensing behaviour. In the case of platinum, small amounts of dopant significantly increases the sensor signal for reducing gases like CO, whereas large amounts inhibit almost completely the sensing reaction. Catalytic conversion measurements revealed that in the latter case, most of the CO directly reacts at the Pt clusters. Pd doping of SnO_2 decreases the sensor signal for all amounts of palladium.

The direct deposition offers a straightforward method of tuning the thickness of the sensing layer by varying the deposition time. The layer growth can be predicted by a

simplified model of deposition by thermophoresis. For all realised layer thicknesses, other important parameters like grain size or porosity of the layers remain unaffected. The maximum sensor performance for CO of the thus fabricated sensors exhibit directly deposited sensors with a layer thickness of 30 μm. Selectivity enhancement can be gained by directly depositing a second layer on top of the sensing layer. Pd-doped Al_2O_3 was chosen as this second layer. Depositing a thin Pd/Al_2O_3 layer on undoped SnO_2 increases the sensor signal for methane compared to the single layer sensor. By contrast, a thicker Pd/Al_2O_3 layer on Pd-doped SnO_2 decreases the sensor signal for methane. However, as it completely suppresses a sensor signal for interfering gases like CO and ethanol, this combination remarkably increases the selectivity of the sensor for methane. Depending on the desired application, the combination of different materials for multilayer sensor fabrication offers the chance to specifically adjust the sensor performance.

Besides many other factors, the adsorption and desorption processes at the surface of MOX based sensors also depend on the very basic factors metal oxide synthesis route and deposition method. As the proposed method of direct deposition via FSP is a novel technology, also some more fundamental investigations were carried out to achieve insight into the sensing mechanism of those sensors. Simultaneous work function change and resistance measurements with special emphasis on three important gaseous species for many applications (CO, humidity and oxygen) delivered information about local dipolar species that are invisible for standard resistance measurements. At low temperature (200°C) the electron affinity of the SnO_2 is influenced by (i) molecular water that is bond via Lewis acid/base interaction to the surface and (ii) molecular oxygen in a tilted configuration. The measurements performed at high temperatures (400°C) support the existing models for the sensing mechanism of CO in dry air, for humidity and for oxygen: (i) CO reacts with pre-adsorbed oxygen ions, (ii) water dissociates homolytically and forms terminal hydroxyl groups with a pre-adsorbed oxygen ion, and (iii) oxygen adsorption ends up with ionosorbed species.

The accompanying investigation of the sensing performance throughout the successive implementation of FSP into a single-step sensor fabrication technology assures this method a high potential for commercial use.

6.1.2 Benchmarking

When discussing such applicability for commercial use, each new technology has to additionally withstand the thorough benchmarking with the existing and state-of-the-art technologies.

In a first attempt it was shown that FSP generated SnO_2 nanoparticles can fully compete with commercial SnO_2 powders for various gases. For CO and propanal sensing it shows even superior performance. The next consequent step was to compare the behaviour of the directly deposited sensors with sensors using classical deposition methods like screen printing and spin coating. In the case of CO, the directly deposited sensors show the highest sensor signals in dry as well as in humid air. For ethanol sensing the directly deposited sensors bear the advantage of unaffected sensor signal due to humidity, whereas the signals for screen printed and spin coated sensors decrease remarkably in the presence of humidity.

Finally, the technological benchmarking with screen printing fully demonstrates the potential of FSP direct deposition. It was demonstrated that the direct deposition of SnO_2 nanoparticles leads to highly porous layers with a very large accessible surface. At the same time the layers are smooth and homogeneous without any larger agglomerates or any cracks within the layer. Furthermore, the synthesis and deposition of the sensing material on the sensor substrates is finished for the FSP direct deposition within minutes whereas synthesis of metal oxides via sol-gel processes and the following screen printing takes several days. On top of this, screen printing needs additional organic additives that one has to get rid of at the end of the process.

6.2 Outlook

According to the two guiding principles of the present thesis, the future research on FSP direct deposition for gas sensor fabrication should focus on both the investigation of the gas sensing properties and the related gas sensing mechanisms on the one hand and at the

same time on the benchmarking of the achieved results with the state-of-the-art technology for gas sensor fabrication. This way, the presented technology has a high potential to sustainable determine the progress in this field of research.

Although the results of the simultaneous work function and resistance measurements clearly revealed the presence of different kinds of dipolar species under certain conditions (i.e. oxygen at low temperatures, CO in the background of humidity), the exact nature of these species is still unclear. Therefore, the potential of this measurement technique should be exploited by investigating the realised sensors under various conditions: (i) the measurements with oxygen, CO and humidity over the whole operating temperature range; (ii) measurements with methane and the single layer and double layer sensors to understand the mechanism of the methane sensing by the use of filters; (iii) identical measurements with undoped and differently doped SnO_2 sensors to complete the picture of the role of the dopants. Furthermore, applying Diffuse Reflectance Infrared Fourier Transformed Spectroscopy (DRIFT) to the sensors could allow for identifying the accompanying surface species that appear during the above mentioned measurements [177]. Another measurement technique of interest for future investigations is impedance spectroscopy on the fabricated sensors. This could clarify the contribution of the different parts of the sensor on the signal transduction, i.e. the grain boundaries, the contact between metal oxide and electrodes, the contact between metal oxide and substrate, etc [20].

Further development steps on the technological side could be the use of different filter materials as the top layer of the sensor. In the present study, Pd-doped alumina was chosen, because this is known as a very good catalyst in the oxidation of methane. However, different kinds of metal oxides with different functionalities could be synthesised and thus sensors with completely different selectivity could be achieved. Up to now, only standard ceramic substrates were used for direct deposition. In future research, new kinds of materials could be used for the substrates, e.g. silicon based substrates. Thus, much smaller sensors could be realised. It has to be pointed out that for all those considerations the achieved progress has to be carefully checked with regard to

its manufacturing and gas sensing properties. Otherwise, it will not be able to be implemented into commercial use.

Summarising, one can state that there is a lot of promising future research that can be performed on the basis of the knowledge that was gained within this thesis.

7

Bibliography

Bibliography

1. Müller-Baden, E. *Bibliothek des allgemeinen und praktischen Wissens für Militäranwärter* (Deutsches Verlaghaus Bong & Co, Berlin, 1905).

2. Heiland, G. Zum einfluss von wasserstoff auf die elektrische leitfahigkeit an der oberflache von zinkoxydkristallen. *Zeitschrift Fur Physik* **148**, 15-27 (1957).

3. Bielanski, A., Deren, J. & Haber, J. Electric conductivity and catalytic activity of semiconducting oxide catalysts. *Nature* **179**, 668-679 (1957).

4. Seiyama, T., Kato, A., Fujiishi, K. & Nagatani, M. A new detector for gaseous components using semiconductive thin films. *Analytical Chemistry* **34**, 1502-& (1962).

5. Taguchi, N. Gas detecting device. *U.S. Patent. 3,631,436* (1971).

6. http://www.figarosens.com.

7. http://www.fisinc.co.jp.

8. http://www.umweltsensortechnik.de.

9. http://www.appliedsensors.com.

10. http://www.microchemical.com.

11. http://www.citytech.com/.

12. Wang, Z. L. *Nanowires and Nanobelts: Materials, Properties and Devices, Volume 1: Metal and Semiconductor Nanowires* (Kluwer, Boston, 2003).

13. Sawicka, K. M., Prasad, A. K. & Gouma, P. I. Metal oxide nanowires for use in chemical sensing applications. *Sensor Letters* **3**, 31-35 (2005).

14. Kolmakov, A., Klenov, D. O., Lilach, Y., Stemmer, S. & Moskovits, M. Enhanced gas sensing by individual SnO2 nanowires and nanobelts functionalized with Pd catalyst particles. *Nano Letters* **5**, 667-673 (2005).

15. Moskovits, M., Kolmakov, A. & Zhang, Y. X. Smart sensors: Semiconductor nanowire-based FETS and nanowire arrays. *Abstracts of Papers of the American Chemical Society* **227**, U115-U115 (2004).

16. Kolmakov, A., Zhang, Y. X., Cheng, G. S. & Moskovits, M. Detection of CO and O-2 using tin oxide nanowire sensors. *Advanced Materials* **15**, 997-+ (2003).

17. Barsan, N., Schweizer-Berberich, M. & Gopel, W. Fundamental and practical aspects in the design of nanoscaled SnO2 gas sensors: a status report. *Fresenius Journal of Analytical Chemistry* **365**, 287-304 (1999).

18. Simon, T., Barsan, N., Bauer, M. & Weimar, U. Micromachined metal oxide gas sensors: opportunities to improve sensor performance. *Sensors and Actuators B-Chemical* **73**, 1-26 (2001).

19. Barsan, N. & Weimar, U. Conduction model of metal oxide gas sensors. *Journal of Electroceramics* **7**, 143-167 (2001).

20. Barsan, N. & Weimar, U. Understanding the fundamental principles of metal oxide based gas sensors; the example of CO sensing with SnO2 sensors in the presence of humidity. *Journal of Physics-Condensed Matter* **15**, R813-R839 (2003).

21. Mädler, L. & Pratsinis, S. E. Bismuth oxide nanoparticles by flame spray pyrolysis. *Journal of the American Ceramic Society* **85**, 1713-1718 (2002).

22. Stark, W. J. & Pratsinis, S. E. Aerosol flame reactors for manufacture of nanoparticles. *Powder Technology* **126**, 103-108 (2002).

23. Strobel, R., Stark, W. J., Mädler, L., Pratsinis, S. E. & Baiker, A. Flame-made platinum/alumina: structural properties and catalytic behaviour in enantioselective hydrogenation. *Journal of Catalysis* **213**, 296-304 (2003).

24. Koziej, D. *Phenomenological and Spectroscopic Studies on Gas Detection Mechanism of Selected Gases with Tin Dioxide Based Sensors* (Shaker Verlag, Aachen, 2006).

25. Morrison, S. R. *The Chemical Physics of Surfaces* (1977).

26. Willett, M. J. Spectroscopy of surface reactions. *Tech. Mech. Gas Sens.*, 61-107 (1991).

27. Henrich, V. E. & Cox, P. A. *The Surface Science of Metal Oxides* (1994).

28. Hahn, S. H., Barsan, N. & Weimar, U. Investigation of CO/CH4 mixture measured with differently doped SnO2 sensors. *Sensors and Actuators, B: Chemical* **B78**, 64-68 (2001).

29. Hahn, S. H. et al. CO sensing with SnO2 thick film sensors: role of oxygen and water vapour. *Thin Solid Films* **436**, 17-24 (2003).

30. Barsan, N., Stetter, J. R., Findlay, M. & Gopel, W. High performance gas sensing of CO: Comparative tests for semiconducting (SnO2-based) and for amperometric gas sensors. *Analytical Chemistry* **71**, 2512-2517 (1999).

31. Hyodo, T. et al. NOx sensing properties of WO3-based semiconductor gas sensors fabricated by slide-off transfer printing. *Electrochemistry* **71**, 481-484 (2003).

Bibliography

32. Cantalini, C., Lozzi, L., Passacantando, A. & Santucci, S. The comparative effect of two different annealing temperatures and times on the sensitivity and long-term stability of WO3 thin films for detecting NO2. *Ieee Sensors Journal* **3**, 171-179 (2003).

33. Gillet, M., Aguir, K., Bendahan, M. & Mennini, P. Grain size effect in sputtered tungsten trioxide thin films on the sensitivity to ozone. *Thin Solid Films* **484**, 358-363 (2005).

34. Wager, J. F. Applied physics: Transparent electronics. *Science (Washington, DC, United States)* **300**, 1245-1246 (2003).

35. Presley, R. E. et al. Tin oxide transparent thin-film transistors. *Journal of Physics D: Applied Physics* **37**, 2810-2813 (2004).

36. Masuda, S. et al. Transparent thin-film transistors using ZnO as an active channel layer and their electrical properties. *Journal of Applied Physics* **93**, 1624-1630 (2003).

37. Fuller, M. J. & Warwick, M. E. Catalytic oxidation of carbon monoxide on tin(IV) oxide. *Journal of Catalysis* **29**, 441-50 (1973).

38. Park, P. W., Kung, H. H., Kim, D. W. & Kung, M. C. Characterization of SnO2/Al2O3 lean NOx catalysts. *Journal of Catalysis* **184**, 440-454 (1999).

39. Jarzebski, Z. M. & Marton, J. P. Physical properties of stannic oxide materials. III. Optical properties. *Journal of the Electrochemical Society* **123**, 333C-346C (1976).

40. Batzill, M. & Diebold, U. The surface and materials science of tin oxide. *Progress in Surface Science* **79**, 47-154 (2005).

41. Klementova, M., Rieder, M. & Weiss, Z. Rietveld refinement of cassiterite: a caveat for meticulous sample preparation. *Journal of the Czech Geological Society* **45**, 155-157 (2000).

42. Kilic, C. & Zunger, A. Origins of coexistence of conductivity and transparency in SnO2. *Physical Review Letters* **88**, - (2002).

43. Landolt, B. *Semiconductors Subvolume f Physics of Nontetrahedrally Bonded Binary Compounds II* (ed. Madelung, O.) (Springer Verlag, Berlin New York, 1982).

44. Cox, P. A., Dean, F. W. H. & Williams, A. A. Electrostatic models for surfaces of ionic crystals. *Vacuum* **33**, 839-41 (1983).

45. Munnix, S. & Schmeits, M. Electronic structure of tin dioxide surfaces. *Physical Review B: Condensed Matter and Materials Physics* **27**, 7624-35 (1983).

46. Gopel, W. Chemisorption and charge transfer at ionic semiconductor surfaces: implications in designing gas sensors. *Progress in Surface Science* **20**, 9-103 (1985).

47. Madou, M. J. & Morrison, S. R. *Chemical Sensing with Solid State Devices* (1989).

48. Volkenstein, F. F. *Electronic Processes on the Surface of Semiconductors During Chemisorption* (1987).

49. Geistlinger, H. Electron theory of thin-film gas sensors. *Sensors and Actuators, B: Chemical* **17**, 47-60 (1993).

50. Rothschild, A. & Komem, Y. Numerical computation of chemisorption isotherms for device modeling of semiconductor gas sensors. *Sensors and Actuators B-Chemical* **93**, 362-369 (2003).

51. Weisz, P. B. Effects of Electronic Charge between Adsorbate und Solid on Chemisorption and Catalysis. *Journal of Chemical Physics* **21**, 1531-8 (1952).

52. Yamazoe, N., Fuchigami, J., Kishikawa, M. & Seiyama, T. Interactions of tin oxide surface with oxygen, water, and hydrogen. *Surface Science* **86**, 335-44 (1979).

53. Joly, J. P., Gonzalez-Cruz, L. & Arnaud, Y. Temperature programmed desorption of labile oxygen from stannic oxide. *Bulletin de la Societe Chimique de France*, 11-17 (1986).

54. Che, M. & Tench, A. J. Characterization and reactivity of mononuclear oxygen species on oxide surfaces. *Advances in Catalysis* **31**, 77-133 (1982).

55. Morazzoni, F. et al. Nanostructured Pt-doped tin oxide films: sol-gel preparation, spectroscopic and electrical characterization. *Chemistry of Materials* **13**, 4355-4361 (2001).

56. Armelao, L. et al. Can electron paramagnetic resonance measurements predict the electrical sensitivity of SnO2-based film? *Applied Magnetic Resonance* **22**, 89-100 (2002).

57. Chang, S.-C. Oxygen chemisorption on tin oxide: correlation between electrical conductivity and EPR measurements. *Journal of Vacuum Science and Technology* **17**, 366-9 (1980).

58. Davydov, A. A. IR spectroscopic investigation of oxygen states and of their reactivities on the tin dioxide surface. *Zhurnal Prikladnoi Spektroskopii* **56**, 597-605 (1992).

59. Davydov, A. A. *Molecular spectroscopy of oxide catalyst surfaces* (John Wiley&Sons, Chichester, 2003).

60. Lenaerts, S., Roggen, J. & Maes, G. FT-IR characterization of tin dioxide gas sensor materials under working conditions. *Spectrochimica Acta, Part A: Molecular and Biomolecular Spectroscopy* **51A**, 883-94 (1995).

61. Slater, B., Catlow, C. R. A., Williams, D. E. & Stoneham, A. M. Dissociation of O-2 on the reduced SnO2 (110) surface. *Chemical Communications*, 1235-1236 (2000).

62. Yamaguchi, Y., Tabata, K. & Suzuki, E. Density functional theory calculations for the interaction of oxygen with reduced M/SnO2(1 1 0) (M=Pd, Pt) surfaces. *Surface Science* **526**, 149-158 (2003).

63. Oviedo, J. & Gillan, M. J. First-principles study of the interaction of oxygen with the SnO2(110) surface. *Surface Science* **490**, 221-236 (2001).

64. Sensato, F. R. et al. Periodic study on the structural and electronic properties of bulk, oxidized and reduced SnO2(110) surfaces and the interaction with O-2. *Surface Science* **511**, 408-420 (2002).

65. Tabata, K., Kawabe, T., Yamaguchi, Y. & Nagasawa, Y. Chemisorbed oxygen species over the (110) face of SnO2. *Catalysis Surveys from Asia* **7**, 251-259 (2003).

66. Maki-Jaskari, M. A., Rantala, T. T. & Golovanov, V. V. Computational study of charge accumulation at SnO2(110) surface. *Surface Science* **577**, 127-138 (2005).

67. Thiel, P. A. & Madey, T. F. The interaction of water with solid surfaces: fundamental aspects. *Surface Science Reports* **7**, 211-385 (1987).

68. Henderson, M. A. The interaction of water with solid surfaces: fundamental aspects revisited. *Surface Science Reports* **46**, 1-308 (2002).

69. Heiland, G. & Kohl, D. Physical and chemical aspects of oxidic semiconductor gas sensors. *Chemical Sensor Technology* **1**, 15-38 (1988).

70. Matsuura, Y., Takahata, K. & Ihokura, K. Mechanism of gas sensitivity change with time of tin dioxide gas sensors. *Sensors and Actuators* **14**, 223-32 (1988).

71. Schierbaum, K. D., Weimar, U., Goepel, W. & Kowalkowski, R. Conductance, work function and catalytic activity of tin dioxide-based gas sensors. *Sensors and Actuators, B: Chemical* **B3**, 205-14 (1991).

72. Koziej, D. et al. Water-oxygen interplay on tin dioxide surface: Implication on gas sensing. *Chemical Physics Letters* **410**, 321-323 (2005).

73. Ionescu, R., Vancu, A., Moise, C. & Tomescu, A. Role of water vapour in the interaction of SnO2 gas sensors with CO and CH4. *Sensors and Actuators, B: Chemical* **B61**, 39-42 (1999).

74. Williams, D. E. & Pratt, K. F. E. Classification of reactive sites on the surface of polycrystalline tin dioxide. *Journal of the Chemical Society, Faraday Transactions* **94**, 3493-3500 (1998).

75. Kohl, D. Surface processes in the detection of reducing gases with tin dioxide-based devices. *Sensors and Actuators* **18**, 71-113 (1989).

76. Yamaguchi, Y., Nagasawa, Y., Shimomura, S. & Tabata, K. Reaction model for methane oxidation on reduced SnO2 (110) surface. *International Journal of Quantum Chemistry* **74**, 423-433 (1999).

77. Kohl, D. Oxidic semiconductor gas sensors. *Gas Sens.*, 43-88 (1992).

78. Kappler, J. *Characterization of high-performance SnO2 gas sensors for CO detection by in-situ techniques* (ed. Ph.D. Thesis, U. o. T.) (Shaker Verlag, Aachen, 2001).

79. Baraton, M. I., Merhari, L., Ferkel, H. & Castagnet, J. F. Comparison of the gas sensing properties of tin, indium and tungsten oxides nanopowders: carbon monoxide and oxygen detection. *Materials Science & Engineering C-Biomimetic and Supramolecular Systems* **19**, 315-321 (2002).

80. Koziej, D. et al. Spectroscopic insights into CO sensing of undoped and palladium doped tin dioxide sensors derived from hydrothermally treated tin oxide sol. *Sensors and Actuators, B: Chemical* **B118**, 98-104 (2006).

81. Sahm, T., Gurlo, A., Barsan, N., Weimar, U. & Madler, L. Fundamental studies on SnO2 by means of simultaneous work function change and conduction measurements. *Thin Solid Films* **490**, 43-47 (2005).

82. Egashira, M., Nakashima, M. & Kawasumi, S. Influence of coadsorbed water on the reactivity of oxygen adsorbates on noble metal-doped tin(IV) oxides. *Analytical Chemistry Symposia Series* **17**, 41-6 (1983).

83. Jacobs, H., Mokwa, W., Kohl, D. & Heiland, G. Characterization of structure and reactivity of ZnO and SnO2 supported Pd catalysts. *Vacuum* **33**, 869-870 (1983).

84. Cabot, A. et al. Analysis of the noble metal catalytic additives introduced by impregnation of as obtained SnO2 sol-gel nanocrystals for gas sensors. *Sensors and Actuators B-Chemical* **70**, 87-100 (2000).

85. Cabot, A., Dieguez, A., Romano-Rodriguez, A., Morante, J. R. & Barsan, N. Influence of the catalytic introduction procedure on the nano-SnO2 gas sensor performances - Where and how stay the catalytic atoms? *Sensors and Actuators B-Chemical* **79**, 98-106 (2001).

86. Yamazoe, N. New approaches for improving semiconductor gas sensors. *Sensors and Actuators, B: Chemical* **B5**, 7-19 (1991).

87. Morrison, S. R. Selectivity in semiconductor gas sensors. *Sensors and Actuators* **12**, 425-40 (1987).

88. Matsushima, S., Maekawa, T., Tamaki, J., Miura, N. & Yamazoe, N. New methods for supporting palladium on a tin oxide gas sensor. *Sensors and Actuators, B: Chemical* **B9**, 71-8 (1992).

89. Matsushima, S., Teraoka, Y., Miura, N. & Yamazoe, N. Electronic interaction between metal additives and tin dioxide in tin dioxide-based gas sensors. *Japanese Journal of Applied Physics, Part 1: Regular Papers, Short Notes & Review Papers* **27**, 1798-802 (1988).

90. Harrison, P. G. & Editor. *Chemistry of Tin* (1989).

91. Lantto, V., Rantala, T. T. & Rantala, T. S. Atomistic understanding of semiconductor gas sensors. *Journal of the European Ceramic Society* **21**, 1961-1965 (2001).

92. Tsang, S. C., Bulpitt, C. D. A., Mitchell, P. C. H. & Ramirez-Cuesta, A. J. Some New Insights into the Sensing Mechanism of Palladium Promoted Tin (IV) Oxide Sensor. *Journal of Physical Chemistry B* **105**, 5737-5742 (2001).

93. Pfaff, G. Effect of powder preparation and sintering on the electrical properties of tin dioxide-based ceramic gas sensors. *Sensors and Actuators, B: Chemical* **20**, 43-8 (1994).

94. Fliegel, W., Behr, G., Werner, J. & Krabbes, G. Preparation, development of microstructure, electrical and gas-sensitive properties of pure and doped SnO2 powders. *Sensors and Actuators, B: Chemical* **19**, 474-7 (1994).

95. Orlik, D. R., Ivanovskaya, M. I. & Kol, K. D. Characterization of semiconductor tin dioxide film sensors prepared by the sol-gel method. *Journal of Analytical Chemistry (Translation of Zhurnal Analiticheskoi Khimii)* **50**, 1073-7 (1995).

96.   Daza, L., Dassy, S. & Delmon, B. Chemical sensors based on tin dioxide and tungsten trioxide for the detection of formaldehyde: cooperative effects. *Sensors and Actuators, B: Chemical* **B10**, 99-105 (1993).

97.   Comini, E., Faglia, G., Sberveglieri, G., Pan, Z. & Wang, Z. L. Stable and highly sensitive gas sensors based on semiconducting oxide nanobelts. *Applied Physics Letters* **81**, 1869-1871 (2002).

98.   Faglia, G., Baratto, C., Sberveglieri, G., Zha, M. & Zappettini, A. Adsorption effects of NO2 at ppm level on visible photoluminescence response of SnO2 nanobelts. *Applied Physics Letters* **86**, 011923/1-011923/3 (2005).

99.   Cheng, G. S. et al. Current rectification in a single GaN nanowire with a well-defined p-n junction. *Applied Physics Letters* **83**, 1578-1580 (2003).

100.   Law, M., Kind, H., Messer, B., Kim, F. & Yang, P. D. Photochemical sensing of NO2 with SnO2 nanoribbon nanosensors at room temperature. *Angewandte Chemie-International Edition* **41**, 2405-2408 (2002).

101.   Shimizu, Y., Hyodo, T. & Egashira, M. Mesoporous semiconducting oxides for gas sensor application. *Journal of the European Ceramic Society* **24**, 1389-1398 (2004).

102.   Hyodo, T., Shimizu, Y. & Egashira, M. Design of mesoporous oxides as semiconductor gas sensor materials. *Electrochemistry (Tokyo, Japan)* **71**, 387-393 (2003).

103.   Scott, R. W. J. et al. Tin dioxide opals and inverted opals. Near-ideal microstructures for gas sensors. *Advanced Materials (Weinheim, Germany)* **13**, 1468-1472 (2001).

104.   Scott, R. W. J., Yang, S. M., Coombs, N., Ozin, G. A. & Williams, D. E. Engineered sensitivity of structured tin dioxide chemical sensors: Opaline architectures with controlled necking. *Advanced Functional Materials* **13**, 225-231 (2003).

105.   King, A. G. & Editor. *Ceramic Technology and Processing* (2000).

106.   Kodas, T. T. & Hampden-Smith, M. J. *Aerosol Processing of Materials* (1999).

107.   Taylor, C. J. & Semancik, S. Use of microhotplate arrays as microdeposition substrates for materials exploration. *Chemistry of Materials* **14**, 1671-1677 (2002).

108.   Heule, M. & Gauckler, L. J. Gas sensors fabricated from ceramic suspensions by micromolding in capillaries. *Advanced Materials* **13**, 1790-1793 (2001).

109. Su, M., Li, S. Y. & Dravid, V. P. Miniaturized chemical multiplexed sensor array. *Journal of the American Chemical Society* **125**, 9930-9931 (2003).

110. Sahm, T., Gurlo, A., Barsan, N. & Weimar, U. Properties of indium oxide semiconducting sensors deposited by different techniques. *Particulate Science and Technology* **24**, 441-452 (2006).

111. Vincenzi, D. et al. Low-power thick-film gas sensor obtained by a combination of screen printing and micromachining techniques. *Thin Solid Films* **391**, 288-292 (2001).

112. Riviere, B., Viricelle, J. P. & Pijolat, C. Development of tin oxide material by screen-printing technology for micro-machined gas sensors. *Sensors and Actuators B-Chemical* **93**, 531-537 (2003).

113. Pijolat, C., Viricelle, J. P., Tournier, G. & Montmeat, P. Application of membranes and filtering films for gas sensors improvements. *Thin Solid Films* **490**, 7-16 (2005).

114. Kwon, C. H. et al. Multi-layered thick-film gas sensor array for selective sensing by catalytic filtering technology. *Sensors and Actuators, B: Chemical* **B65**, 327-330 (2000).

115. Tournier, G. & Pijolat, C. Selective filter for SnO2-based gas sensor: application to hydrogen trace detection. *Sensors and Actuators, B: Chemical* **B106**, 553-562 (2005).

116. Cabot, A. et al. Mesoporous catalytic filters for semiconductor gas sensors. *Thin Solid Films* **436**, 64-69 (2003).

117. Hugon, O., Sauvan, M., Benech, P., Pijolat, C. & Lefebvre, F. Gas separation with a zeolite filter, application to the selectivity enhancement of chemical sensors. *Sensors and Actuators, B: Chemical* **B67**, 235-243 (2000).

118. Schweizer-Berberich, M., Strathmann, S., Gopel, W., Sharma, R. & Peyre-Lavigne, A. Filters for tin dioxide CO gas sensors to pass the UL2034 standard. *Sensors and Actuators, B: Chemical* **B66**, 34-36 (2000).

119. Fleischer, M., Kornely, S., Weh, T., Frank, J. & Meixner, H. Selective gas detection with high-temperature operated metal oxides using catalytic filters. *Sensors and Actuators, B: Chemical* **B69**, 205-210 (2000).

120. Hubalek, J. et al. Pt-loaded Al2O3 catalytic filters for screen-printed WO3 sensors highly selective to benzene. *Sensors and Actuators, B: Chemical* **B101**, 277-283 (2004).

121.   Papadopoulos, C. A., Vlachos, D. S. & Avaritsiotis, J. N. Comparative study of various metal-oxide-based gas-sensor architectures. *Sensors and Actuators, B: Chemical* **B32**, 61-69 (1996).

122.   Tabata, S. et al. A micromachined gas sensor based on a catalytic thick film/SnO2 thin film bilayer and a thin film heater. Part 2: CO sensing. *Sensors and Actuators, B: Chemical* **B109**, 190-193 (2005).

123.   Menil, F., Lucat, C. & Debeda, H. The thick-film route to selective gas sensors. *Sensors and Actuators, B: Chemical* **B25**, 415-20 (1995).

124.   Mandayo, G. G. et al. Built-in active filter for an improved response to carbon monoxide combining thin- and thick-film technologies. *Sensors and Actuators, B: Chemical* **B87**, 88-94 (2002).

125.   Sberveglieri, G. Classical and novel techniques for the preparation of tin dioxide thin-film gas sensors. *Sensors and Actuators, B: Chemical* **B6**, 239-47 (1992).

126.   Wollenstein, J., Bottner, H., Jaegle, M., Becker, W. J. & Wagner, E. Material properties and the influence of metallic catalysts at the surface of highly dense SnO2 films. *Sensors and Actuators, B: Chemical* **B70**, 196-202 (2000).

127.   Zhu, W. & Pratsinis, S. E. Synthesis of SiO2 and SnO2 particles in diffusion flame reactors. *AIChE Journal* **43**, 2657-2664 (1997).

128.   Vemury, S., Pratsinis, S. E. & Kibbey, L. Electrically controlled flame synthesis of nanophase TiO2, SiO2, and SnO2 powders. *Journal of Materials Research* **12**, 1031-1042 (1997).

129.   Lindackers, D., Janzen, C., Rellinghaus, B., Wassermann, E. F. & Roth, P. Synthesis of Al2O3 and SnO2 particles by oxidation of metal-organic precursors in premixed H2/O2/Ar low-pressure flames. *Nanostructured Materials* **10**, 1247-1270 (1999).

130.   Pratsinis, S. E. Flame aerosol synthesis of ceramic powders. *Progress in Energy and Combustion Science* **24**, 197-219 (1998).

131.   Mädler, L., Stark, W. J. & Pratsinis, S. E. Flame-made ceria nanoparticles. *Journal of Materials Research* **17**, 1356-1362 (2002).

132.   Kennedy, M. K. et al. Tailored nanoparticle films from monosized tin oxide nanocrystals: particle synthesis, film formation, and size-dependent gas-sensing properties. *Journal of Applied Physics* **93**, 551-560 (2003).

133. Madler, L., Stark, W. J. & Pratsinis, S. E. Simultaneous deposition of Au nanoparticles during flame synthesis of TiO2 and SiO2. *Journal of Materials Research* **18**, 115-120 (2003).

134. Cabanas, M. V., Delabouglise, G., Labeau, M. & Vallet-Regi, M. Application of a modified ultrasonic aerosol device to the synthesis of SnO2 and Pt/SnO2 for gas sensors. *Journal of Solid State Chemistry* **144**, 86-90 (1999).

135. Strobel, R., Krumeich, F., Stark, W. J., Pratsinis, S. E. & Baiker, A. Flame spray synthesis of Pd/Al2O3 catalysts and their behavior in enantioselective hydrogenation. *Journal of Catalysis* **222**, 307-314 (2004).

136. Suda, H., Sudo, S. & Nakahara, M. Fine Glass Particle-Deposition Mechanism in the Vad Process. *Fiber and Integrated Optics* **4**, 427-437 (1983).

137. Rowell, J. M. Photonic Materials. *Scientific American* **255**, 146-& (1986).

138. Thybo, S. et al. Flame spray deposition of porous catalysts on surfaces and in microsystems. *Journal of Catalysis* **223**, 271-277 (2004).

139. Skandan, G. et al. Low-pressure flame deposition of nanostructured oxide films. *Journal of the American Ceramic Society* **81**, 2753-2756 (1998).

140. Vukasinovic, B., Sundell, S. & Oljaca, M. Closed loop controlled deposition of BaxSr1-xTiO3 thin films in spray flames. *Surface Engineering* **19**, 179-184 (2003).

141. Oljaca, M., Luten, H. A., Tomov, T., Sundell, S. & Hunt, A. Deposition of BaxSr1-xTiO3 in atmospheric pressure flame: Combustion monitoring and optimisation of thin film properties. *Surface Engineering* **19**, 51-57 (2003).

142. Kennedy, M. K., Kruis, F. E. & Fissan, H. Gas phase synthesis of size selected SnO2 nanoparticles for gas sensor applications. *Metastable, Mechanically Alloyed and Nanocrystalline Materials, Pts 1 and 2* **343-3**, 949-954 (2000).

143. Krinke, T. J., Fissan, H. & Deppert, K. Deposition of aerosol nanoparticles on flat substrate surfaces. *Phase Transitions* **76**, 333-345 (2003).

144. Sahm, T. et al. Formation of highly porous gas-sensing films by in-situ thermophoretic deposition of nanoparticles from aerosol phase. *Materials Research Society Symposium Proceedings* **915**, 163-174 (2006).

145. Madler, L., Kammler, H. K., Mueller, R. & Pratsinis, S. E. Controlled synthesis of nanostructured particles by flame spray pyrolysis. *Journal of Aerosol Science* **33**, 369-389 (2001).

146. Sahm, T. et al. Flame spray synthesis of tin dioxide nanoparticles for gas sensing. *Sensors and Actuators B-Chemical* **98**, 148-153 (2004).

147. Maedler, L. et al. Direct formation of highly porous gas-sensing films by in situ thermophoretic deposition of flame-made Pt/SnO2 nanoparticles. *Sensors and Actuators, B: Chemical* **B114**, 283-295 (2006).

148. Maedler, L. et al. Sensing low concentrations of CO using flame-spray-made Pt/SnO2 nanoparticles. *Journal of Nanoparticle Research* **8**, 783-796 (2006).

149. Nowotny, J., Dufour, L. C. & Editors. *Materials Science Monographs, 47: Surface and Near-Surface Chemistry of Oxide Materials* (1988).

150. Riviere, J. C. Work function: measurements and results. *Solid State Surface Science* **1**, 179-289 (1969).

151. Thomson, J. J. Contact-Electricity of Metals. *The London, Edinburgh, and Dublin philosophical magazine and journal of science* **46**, 82-119 (1898).

152. Cheary, R. W. & Coelho, A. A. Axial divergence in a conventional X-ray powder diffractometer. I. Theoretical foundations. *Journal of Applied Crystallography* **31**, 851-861 (1998).

153. Bolzan, A. A., Fong, C., Kennedy, B. J. & Howard, C. J. Structural studies of rutile-type metal dioxides. *Acta Crystallographica Section B-Structural Science* **53**, 373-380 (1997).

154. Johannessen, T. & Koutsopoulos, S. One-step flame synthesis of an active Pt/TiO₂ catalyst for SO₂ oxidation - A possible alternative to traditional methods for parallel screening. *Journal of Catalysis* **205**, 404-408 (2002).

155. Dieguez, A. et al. Influence on the gas sensor performances of the metal chemical states introduced by impregnation of calcinated SnO2 sol-gel nanocrystals. *Sensors and Actuators B-Chemical* **68**, 94-99 (2000).

156. Kulkarni, P. & Biswas, P. A Brownian dynamics simulation to predict morphology of nanoparticle deposits in the presence of interparticle interactions. *Aerosol Science and Technology* **38**, 541-554 (2004).

157. Watson, J. The stannic oxide semiconductor gas sensor. *Sensors, Nanoscience, Biomedical Engineering, and Instruments*, 1/18-1/24 (2006).

158. Directive 2000/69/EC of the European parliement and of the council. *Official Journal of the Europena Commision* **L313/12** (November 16, 2000).

159. Schweizer-Berberich, M. et al. The effect of Pt and Pd surface doping on the response of nanocrystalline tin dioxide gas sensors to CO. *Sensors and Actuators, B: Chemical* **B31**, 71-5 (1996).

160. Gaidi, M., Labeau, M., Chenevier, B. & Hazemann, J. L. In-situ EXAFS analysis of the local environment of Pt particles incorporated in thin films of SnO2 semi-conductor oxide used as gas-sensors. *Sensors and Actuators B-Chemical* **48**, 277-284 (1998).

161. Kappler, J. et al. Correlation between XPS, Raman and TEM measurements and the gas sensitivity of Pt and Pd doped SnO2 based gas sensors. *Fresenius Journal of Analytical Chemistry* **361**, 110-114 (1998).

162. Matko, I., Gaidi, M., Hazemann, J. L., Chenevier, B. & Labeau, M. Electrical properties under polluting gas (CO) of Pt- and Pd-doped polycrystalline SnO2 thin films: analysis of the metal aggregate size effect. *Sensors and Actuators B-Chemical* **59**, 210-215 (1999).

163. Cabot, A. in *Facultat de Fisica* 480 (Universitat de Barcelona, Barcelona, 2004).

164. Matko, I. et al. Pt doping of SnO2 thin films - A transmission electron microscopy analysis of the porosity evolution. *Journal of the Electrochemical Society* **149**, H153-H158 (2002).

165. Stark, W. J., Grunwaldt, J.-D., Maciejewski, M., Pratsinis, S. E. & Baiker, A. Flame-Made Pt/Ceria/Zirconia for Low-Temperature Oxygen Exchange. *Chemistry of Materials* **17**, 3352-3358 (2005).

166. Xu, C., Tamaki, J., Miura, N. & Yamazoe, N. Grain-Size Effects on Gas Sensitivity of Porous SnO_2-Based Elements. *Sensors and Actuators B-Chemical* **3**, 147-155 (1991).

167. Korotcenkov, G. Gas response control through structural and chemical modification of metal oxide films: state of the art and approaches. *Sensors and Actuators, B: Chemical* **B107**, 209-232 (2005).

168. Rothschild, A. & Komem, Y. The effect of grain size on the sensitivity of nanocrystalline metal-oxide gas sensors. *Journal of Applied Physics* **95**, 6374-6380 (2004).

169. Bauer, M. et al. in *11th European Microelectronics Conference* 37-44 (Venice, 1997).

170. Sakai, G., Matsunaga, N., Shimanoe, K. & Yamazoe, N. Theory of gas-diffusion controlled sensitivity for thin film semiconductor gas sensor. *Sensors and Actuators B-Chemical* **80**, 125-131 (2001).

171. Gardner, J. W. A Diffusion-Reaction Model of Electrical-Conduction in Tin Oxide Gas Sensors. *Semiconductor Science and Technology* **4**, 345-350 (1989).

172. Williams, D. E. in *Solid State Gas Sensors* (eds. Moseley, P. T., Totfield, B. C. & Hilger, A.) 71-123 (Bristol & Philadelphia, Philadelphia, 1987).

173. Montmeat, P., Lalauze, R., Viricelle, J. P., Tournier, G. & Pijolat, C. Model of the thickness effect of SnO2 thick film on the detection properties. *Sensors and Actuators, B: Chemical* **B103**, 84-90 (2004).

174. Hossein-Babaei, F. & Orvatinia, M. Ananlysis of thickness dependence of the sensitivity in thin film resitive gas sensors. *Sensors and Actuators B-Chemical* **89**, 256-261 (2004).

175. Capone, S. (University of Lecce, Lecce, 2000).

176. Demoulin, O., Navez, M. & Ruiz, P. Investigation of the behaviour of a Pd/g-Al2O3 catalyst during methane combustion reaction using in situ DRIFT spectroscopy. *Applied Catalysis, A: General* **295**, 59-70 (2005).

177. Harbeck, S., Szatvanyi, A., Barsan, N., Weimar, U. & Hoffmann, V. DRIFT studies of thick film un-doped and Pd-doped SnO2 sensors: temperature changes effect and CO detection mechanism in the presence of water vapour. *Thin Solid Films* **436**, 76-83 (2003).

List of abbreviations

symbol	description
A	surface area
ac	air conditioning
AFM	atomic force microscope
BET	Brunauer, Emmett and Teller
C	capacity
CCVD	combustion chemical vapor deposition
CMOS	Complementary Metal Oxide Semiconductors
CVD	chemical vapour deposition
cwa	chemical warfare agents
d	distance
d_p	particle diameter
DPN	dip-pen nanolithography
DRIFT	Diffuse Reflectance Infrared Fourier Transformed Spectroscopy
$E_{binding}$	binding energy
Ec	energy of concuction band edge
E_D	Energy of donor level
EDX	energy dispersive X-ray
E_f	Fermi energy
E_g	band gap energy
EPR	Electron Paramagnetic Resonance Spectroscopy
ETH	Swiss Federal Institute of Technology
Ev	energy of valence band edge
EXAFS	extended X-ray absorption fine structure
FSD	flame spray deposition
FSP	flame spray pyrolysis
G	conductance
HRTEM	high resolution transmission electron microscopy
I	current
IMCS	International Meeting on Chemical Sensors
IR	infra red
ITO	indium-tin oxide
J	total particle number flux
K	Boltzman constant
L	lenghth of sensing layer
ℓ	stagnation gas layer thickness

symbol	description
LDL	lower detection limit
m	sensitivity
MAK	Maximale Arbeitsplatz Konzentration
MEMS	Micro-Electro-Mechanical Systems
MOX	metal oxides
OVD	outside vapor deposition
PEG	polyethyleneglycol
ppb	parts per billion
ppm	parts per million
PVD	physical vapour deposition
q	heat flux
Q	reproducability
qV_S	surcafe band bending
R	resistance
r.h.	relative humidity
rf	radio frequency
S	sensor signal
SEM	scanning electron microscopy
s_s	solid layer thickness
SSA	specific surface area
s_{sl}	porous layer thickness
STEM	scanning transition electron microscopy
T	absolute temperature
TCO	transparent conducting oxide
TDS	thermal desorption spectroscopy
TEM	transmission electron microscopy
TPD	temperature programmed desorption
T_{res}	response time
UCLA	University of California, Los Angelos
UHV	ultra high vacuum
V	voltage
VAD	vapor axial deposition
VCPD	contact potential difference
w	width of sensing layer
wt%	weight percent

symbol	description
XANES	X-ray absorption near edge structure
XPS	x-ray photoelectron spectroscopy
XRD	X-ray diffraction pattern
α	analytical sensitivity
ε	dielectric constant
λ	thermal conductivity
Φ	work function
ϕ	porosity
ρ	density
ρ_{SC}	resistivity of the semiconductor
φ	porosity
σ	standard deveation
χ	electron affinity
ξ_{dep}	layer growth rate
ω	frequency

Acknowledgements

Herrn PD Dr. Udo Weimar danke ich für die Bereitstellung des interessanten Themas meiner Dissertation. Darüber hinaus sind die hervorragenden Arbeitsbedingungen und die Atmosphäre in seinem Arbeitskreis im besten Sinne des Wortes herausragend, sodass man sich dort nur Wohlfühlen kann.

Herrn Prof. Dr. Günther Gauglitz danke ich für die Bereitschaft, das Co-Referat zu übernehmen.

A special *Thanks!* goes to Dr. Nicolae Bârsan for his great support. It was a tough job to introduce a simple-minded chemist like me to the mysterious world of solid state physics. His profound knowledge about every little aspect in MOX based gas sensors is still amazing to me. And besides science, I learnt a lot from him about the real world out there. I'm sure that I will benefit a lot from this many times.

I would like to thank Dr. Lutz Mädler and his team at ETH Zürich and ULCA California for our fruitful collaboration and his engagement in preparing the sensors for this thesis by using his FSP setup.

Einen großen Anteil am äußerst angenehmen Arbeitsklima hatten meine zeitweiligen Zimmerkollegen Dr. Jan Claussen, Dr. Patrick Reichel, Dr. Ourania Sachlara, Johan Bertrand und Dr. Dorota Koziej. Ich danke ihnen für das lockere Miteinander und dafür, dass sie immer bereit waren mir zu helfen.

Ein besonderer Dank gilt hierbei Dr. Dorota Koziej. Das manchmal frustrierende Forscherleben war dank ihres Humors und ihrer Unterstützung oft wesentlich leichter durchzustehen. Außerdem habe ich den monatlichen Wettstreit um die Krone in der Kaffee-Liste sehr genossen – obwohl ich immer noch davon überzeugt bin, dass mein Beitrag in der Kaffee-Kasse ihr eines Tages doch noch den Porsche finanzieren wird. Das geht doch nicht mit rechten Dingen zu!

Ebenfalls ganz besonders danke ich Melanie Sahm, die durch das gesamte Studium und die Promotion hindurch gemeinsam mit mir die Präsenz unseres Nachnamens nachhaltig verdoppelt hat und damit für einige Verwirrung unter der Professorenschaft gesorgt hat. Diese Verwirrung wird uns beide noch lange in Tübingen überleben.

Ich danke außerdem Dr. Alexandru Oprea für seine geduldige Hilfe und Unterstützung, besonders für die vielen kleineren und größeren Arbeitseinsätze im Elektroniklabor und die tatkräftige Einarbeitung in das komplizierte Feld der Kelvin-Probe.

Außerdem danke ich einem ehemaligen Kollegen, Dr. Alexander Gurlo, der mir in meiner Anfangszeit sehr hilfsbereit viele Geräte und zahlreiche Tipps und Tricks gezeigt hat.

Ein herzlicher Dank geht an alle übrigen Kollegen der AG Weimar und auch vor allem an das Team der *permanent staffs*, also Ute Harbusch, Egon Merz, Dr. Michael Wandel und Dr. Nikos Papamichail. Das Arbeiten mit ihnen hat sehr viel Spaß gemacht, und ihre Hilfe im täglichen Kleinkrieg mit den bürokratischen Wirrungen war unentbehrlich für mich.

Die Betreuung von „meinen" Studenten im Mitarbeiterpraktikum war für mich immer eine willkommene Abwechslung. In diesem Zusammenhang danke ich besonders Karsten Holtin für sein Engagement und sein ausgeprägtes Interesse. Er hat mir etliche Stunden vor der Gasmischanlage und bei der Datenauswertung abgenommen.

Ich danke Elke Nadler für die gemeinsamen SEM Aufnahmen und die fruchtbaren Diskussionen dabei. Auch allen anderen Kollegen vom ipc, mit denen ich zusammengearbeitet habe, danke ich für die Unterstützung.

Vielen Dank allen *proof-readern* – ganz besonders meinem Bruder Tobias, dessen Englischkenntnisse mir sehr geholfen haben, zahlreiche Fehler auszumerzen (ja, ich weiß, es heißt *independent of…*).

An dieser Stelle möchte ich die Gelegenheit nutzen, meiner Familie, allen voran meinen Eltern, ganz besonders zu danken. Sie haben mich stets in jeglicher Hinsicht unterstützt und mich vor allem immer meinen Weg gehen lassen. Danke, dass Ihr immer zur richtigen Zeit da seid. Ihr seid klasse!

Zum Schluss gilt mein größtes Dankeschön meiner Frau Dorothea! In den Zeitraum meiner Promotion sind so einige spannende Ereignisse gefallen, die wir gemeinsam zum Teil genossen, zum Teil durchgehalten haben. Gerade im Endspurt meiner Dissertation, als ich ihre Hilfe mehr denn je brauchte, konnte ich mir ihrer Unterstützung sicher sein, was mir sehr geholfen hat. Promotion abschließen, Umzug, Berufseinstieg – das ging nur, weil Du da warst… Tausend Dank!

Meine akademischen Lehrer waren:

K. Albert, D. Christen, H.-J. Egelhaaf, H. Eckstein, G. Gauglitz, F. Gönnenwein,
G. Häfelinger, M. Hanack, D. Hoffmann, V. Hoffman, W. Jäger, W. Koch, D. Krug,
N. Kuhn, M.E. Maier, H.A. Mayer, H.-J. Meyer, E. Lindner, U. Nagel, H. Oberhammer,
D. Oelkrug, H. Pauschmann, H. Pommer, G. Reinhardt, V. Schurig, M. Schwarz,
E. Schweda, F.F. Seelig, J. Strähle, U. Weimar, K.-P. Zeller.

Curriculum Vitae

Name	Thorsten Sahm
Geburtstag	29.07.1977
Geburtsort	Dillenburg
Familienstand	verheiratet
Staatsangehörigkeit	deutsch

Ausbildung

09/1984 – 07/1988	**Grundschule** in Breitscheid (Hessen) und Griesingen (Baden-Württemberg)
09/1988 – 07/1997	**Carl-Laemmle-Gymnasium** in Laupheim mit dem Abschluss der Allgemeinen Hochschulreife
10/1997 – 09/2003	**Studium der Chemie** (Abschlussziel Diplom) an der Eberhard-Karls-Universität Tübingen
09/1999	**Vordiplomprüfungen**
09/2003	**Diplomprüfungen**
	Diplomarbeit bei PD Dr. Udo Weimar am Institut für Physikalische und Theoretische Chemie der Eberhard-Karls-Universität Tübingen
seit 10/2003	Anfertigung einer **Dissertation** bei PD Dr. Udo Weimar am Institut für Physikalische und Theoretische Chemie der Eberhard-Kalrs-Universität Tübingen mit dem Titel "Development of a new single-step process for the production of SnO_2 based gas sensors"